Department of physics, Graduate school of science,
Osaka University.

Doctoral Dissertation

Search for Neutrinoless Double Beta Decay in ^{48}Ca with the CANDLES III experiment

by Takaki Ohata

2018

Abstract

This dissertation reports a search for a neutrinoless double-beta decay ($0\nu\beta\beta$) of ^{48}Ca with the CANDLES Ⅲ experiment.

An observation of the decay demonstrates the Majorana nature of neutrinos, the decay is a lepton number violating process, which is beyond the Standard Model. The nature is vital for understanding of the baryon asymmetry in our universe. Furthermore, the rate of the decay derives the effective neutrino mass.

An experiment for the observation requires large target nuclear mass, low background techniques and high energy resolution, since the decay is very rare process. Reduction of backgrounds for given target mass is the most challenging part of an experiment. The Q value of ^{48}Ca, 4.3 MeV is the highest among all $0\nu\beta\beta$ candidate nuclei, which is a potential advantage to give least backgrounds. We aim to achieve background-free measurement by taking advantage of ^{48}Ca.

The CANDLES Ⅲ experiment started operation in June 2016 at the Kamioka observatory after the construction of a passive shield. The events of gamma ray from (n, γ) reactions, which were dominant backgrounds at the Q value region are reduced drastically. Currently, gamma ray events from the outside of the detector are negligible. Radioactive contamination contained in CaF_2 crystals is reduced by an analysis described in this thesis. Among radioactive isotopes the ^{232}Th series decay chain gives the most serious backgrounds which are ^{212}Bi-Po sequential decay and ^{208}Tl beta decay. The half-life of ^{212}Bi-Po, 0.3 μsec is shorter than the decay time constant of CaF_2 waveform, 1 μsec. Therefore, beta and alpha waveforms pile up and the total energy reaches to Q value region. ^{212}Bi-Po is removed by double pulse shape discrimination using the characteristic of a waveform. The Q value of ^{208}Tl 5.0 MeV is and its sum energy of beta and gamma rays also reaches to the Q value region. ^{208}Tl is removed by delayed coincidence analysis. The alpha ray from ^{212}Bi is selected by pulse shape discrimination. Then, all events in the same crystal within 18 min since the prompt ^{212}Bi alpha ray are vetoed. The time is enough long since the half-life of ^{208}Tl is 3 min. which is enough longer than the half-life of ^{208}Tl, 3 min are vetoed.

The detection efficiency of $0\nu\beta\beta$ and the number of expected backgrounds are evaluated by Monte Carlo simulation. A new limit on the half-life of $0\nu\beta\beta$ decay of $T^{0\nu}_{1/2} > 0.33 \times 10^{23}$ yr at 90% C.L. is obtained using 93 crystals. By using 26 crystals which have lower radioactivity, we achieve background free

measurement and a lower limit on the half-life of $0\nu\beta\beta$ decay of $T^{0\nu}_{1/2} > 1.08 \times 10^{23}$ yr at 90% C.L. is obtained.

In near future, enrichment techniques of ^{48}Ca for larger target mass will be developed. Therefore, we will be able to pursue the neutrino mass down to a few hundred meV.

Contents

List of Figures

List of Tables

Chapter 1

Neutrino Physics

Early in the 20th century, β decay was thought to two-body-decay. At that time this decay was assumed that a neutron is converted to a proton under emanation of an electron as Eq. (1.1).

$$n \rightarrow p + e^{-} \tag{1.1}$$

This dose not satisfy the conservation lows of energy, angular momentum, and spin. Hence, there was a discrepancy between theory and experiment. Neutrinos that are neutral leptons were proposed by W. Pauli in 1930 and were explained by E. Fermi with the following equation:

$$n \rightarrow p + e^{-} + \overline{\nu_e} \tag{1.2}$$

In 1956, antielectron neutrinos were detected by F. Reines and C. Cowan [1]. Antineutrinos created beta decay in a nuclear reactor were observed during inverse beta decay in water in which cadmium chloride was dissolved. After that, in 1962 muon neutrinos were detected by L. Lederman, M. Schwartz, J. Steimberger [2] and in 2001 tau neutrinos were detected by the DONUT experiment at Fermilab [3]. We understand that there are three generation of neutrinos as in the quarks. Elemental particles are summarized in Table1.1.

1.1 Neutrino Mass

For a long time, the absolute mass of neutrino was known to be zero. In the late 1960s, solar neutrinos were observed by R. Davis Homestake experiment utilizing chlorine. [4]. The number of expected solar neutrinos using the standard solar model was not consistent with that of observed and this was

Table 1.1: Fundamental particle of the Standard Model

Particle	charge	I	II	III	spin
quarks	+2/3	u (up)	c (charm)	t (top)	1/2
	-1/3	d (down)	s (strange)	b (bottom)	
leptons	-1	e (electron)	μ (muon)	τ (tau)	1/2
	0	ν_e	ν_μ	ν_τ	

called the solar neutrino problem. It was a big problem until the discovery of neutrino oscillation, with which it was found that the a neutrino mass is not zero but finite.

1.1.1 Neutrino Oscillation

Neutrino oscillation is a phenomenon that a neutrino created with a certain lepton flavor as electron, muon or tau is observed to have a different flavor. It can be described by quantum mechanics. This phenomenon occurs when a neutrino has a finite mass.

An α flavour eigenstates ($|\nu_\alpha\rangle$) and an eigenstates of neutrino mass ($|\nu_i\rangle$) are described by:

$$|\nu_\alpha\rangle = \sum_i U_{\alpha i} |\nu_i\rangle \tag{1.3}$$

,where the matrix U is the MNS matrix (Maki-Nakagawa-Sakata matrix). This unitary mixing matrix is described by mixing angle as θ and CP phase angle as δ as the following equation:

$$U_{\alpha i} = \begin{pmatrix} c_{12}c_{13} & s_{12}c_{13} & s_{13}e^{-i\delta} \\ -s_{12}c_{23} - c_{12}s_{23}s_{13}e^{-i\delta} & c_{12}c_{23} - s_{12}s_{23}s_{13}e^{-i\delta} & s_{23}c_{13} \\ s_{12}s_{23} - c_{12}c_{23}s_{13}e^{-i\delta} & -c_{12}s_{23} - s_{12}c_{23}s_{13}e^{-i\delta} & c_{23}c_{13} \end{pmatrix} \tag{1.4}$$

where $s_{ij} = \sin\theta_{ij}$, $c_{ij} = \cos\theta_{ij}$ $(i, j = 1, 2, 3)$.

The unitary mixing matrix ($U_{2\times2}$) is described for neutrino oscillation with two neutrino flavors as follows:

$$U_{2\times2} = \begin{pmatrix} \cos\theta & \sin\theta \\ -\sin\theta & \cos\theta \end{pmatrix} \tag{1.5}$$

The corresponding transition probability is described

$$\begin{aligned} P(\nu_\alpha \to \nu_\beta) &= \sin^2 2\theta \sin^2 \left(\frac{\Delta {m_{12}}^2 L}{4E} \right) \\ &= \sin^2 2\theta \sin^2 \left(\frac{1.27 \Delta {m_{12}}^2 [\mathrm{eV}^2] L[\mathrm{km}]}{E[\mathrm{MeV}]} \right) \end{aligned} \tag{1.6}$$

, where

$$\Delta {m_{12}}^2 = m_1^2 - m_2^2 \tag{1.7}$$

Neutrino oscillation depends on energy (E), distance between a source and a detector (L), Δm^2 and mixing angle θ.

In 1998, oscillation of atmospheric neutrinos was detected by the Super-Kamiokande experiment [5] and it was confirmed that neutrinos have mass . In 2001, oscillation of solar neutrinos was detected by the SNO experiment at Sudbury Neutrino Observatory in Canada [6]. After that, oscillation of reactor neutrinos was detected by the KamLAND experiment [7]. The neutrino oscillation is confirmed by these experiments.

Three mass eigenstates have mass deference, which have been measured by neutrino oscillation experiment. However, absolute values of mass have not been observed. Hierarchy of three neutrino mass eigenstates from three kinds: normal hierarchy, inverted hierarchy and degenerate in Fig. 1.1.

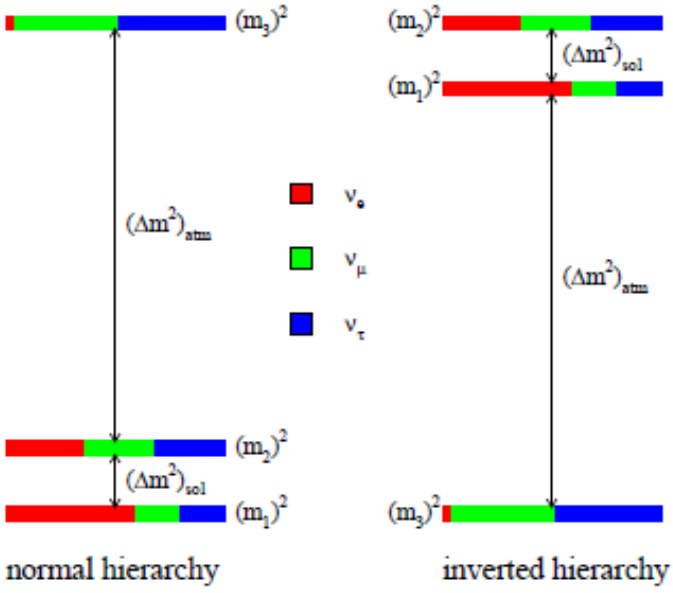

Figure 1.1: Normal and inverted hierarchy of the neutrino mass.

1.2 Double Beta Decay

Double beta decay, which translates two neutrons in a nucleus to two protons, is described by the following equation:

$$ {}^{A}_{Z}X \rightarrow {}^{A}_{Z+2}Y + 2e^{-} + 2\overline{\nu_e} \tag{1.8} $$

Energy spectrum of electrons from a double beta decay is continuous since neutrinos carry certain energy from a nucleus. This decay conserves lepton number and is in the Standard Model.

1.2.1 $0\nu\beta\beta$ Mode

If a neutrino is a Majorana particle, neutrinoless double beta decay ($0\nu\beta\beta$) occurs where neutrinos disappear (Eq. 1.9). Fig. 1.2 shows Feynman diagram of $0\nu\beta\beta$ decay.

$$ {}^{A}_{Z}X \rightarrow {}^{A}_{Z+2}Y + 2e^{-} \tag{1.9} $$

Since only two electrons appear in the final state, sum energy of the two electrons is expected to peak at Q value.

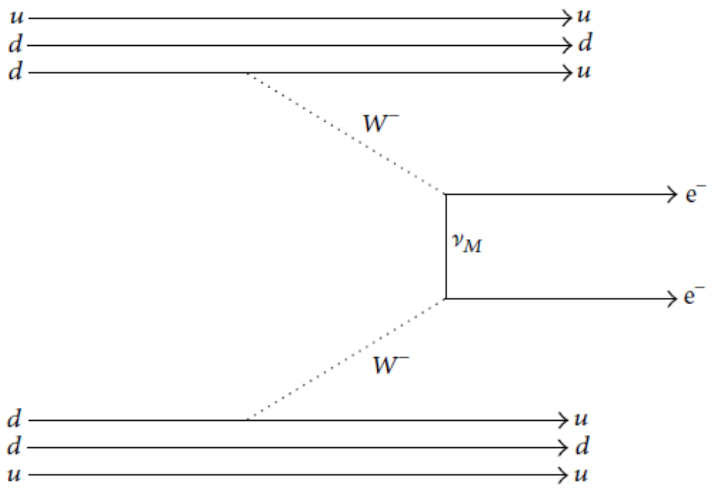

Figure 1.2: Feynman diagram of $0\nu\beta\beta$ decay

Half-life of $0\nu\beta\beta$ decay is described by the following equation:

$$ \left(T^{0\nu}_{1/2}\right)^{-1} = G_{0\nu}|M^{0\nu}|^2 \langle m_{\beta\beta}\rangle^2 \tag{1.10} $$

, where $\langle m_{\beta\beta} \rangle$ is Majorana effective mass, $G_{0\nu}$ is Phase Space Factor (PSF) and $M^{0\nu}$ is Nuclear Matrix Element (NME). The uncertainty of NME is large since there are many models for the calculation. NME is summarized in the next section.

If $0\nu\beta\beta$ decay is observed, the decay demonstrates lepton number violation which is vital for understanding of the baryon asymmetry in our universe. From Eq. 1.10, the Majorana effective neutrino mass is calculated by the half-life of $0\nu\beta\beta$. Fig. 1.3 shows prediction for the effective Majorana effective neutrino mass based on neutrino oscillation observations. Neutrino mass hierarchy will be solved by $0\nu\beta\beta$.

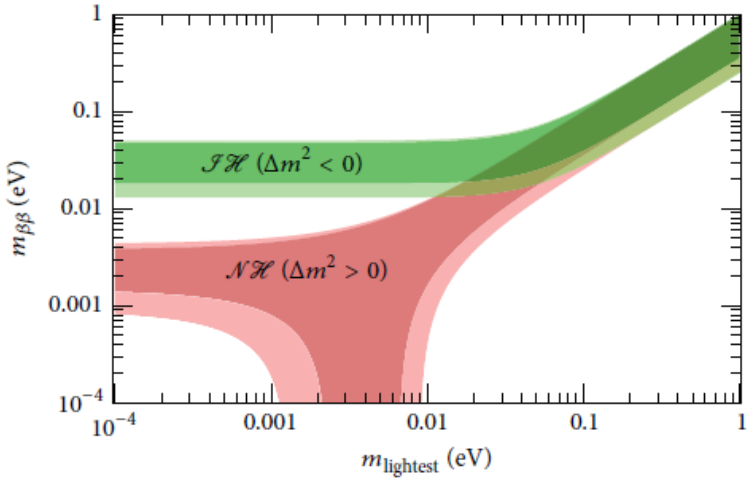

Figure 1.3: Prediction for the effective Majorana mass based on neutrino oscillation observations. The allowing region for the inverted hierarchy are shown in green and for the normal hierarchy are shown in red . The horizontal axis corresponds to the lightest neutrino mass in three neutrino scenario. The vertical axis corresponds to the effective Majorana mass.

1.2.2 Nuclear Matrix Element

The lightest nuclei of the candidates undergoing $0\nu\beta\beta$ decay is ^{48}Ca. A nuclear matrix element of ^{48}Ca can be handled by the shell model with reasonable effort without heavy truncations of model space. For heavier nuclei such as ^{76}Ge and ^{82}Se, a heavy truncation of model space is usually needed. The apporoximation with Ref.[8] is to decouple proton and neutron shells.

The main uncertainty in the estimation of effective Majorana mass by

experimental half-life limits is the nuclear matrix element. Calculations are quite complex and models for them are as follows.

- Interacting shell model (ISM)
- Microscopic interacting boson model (IBM-2)
- Quasiparticle random phase approximation (QRPA)
- Energy density functional methods (EDF)

Fig. 1.4 shows comparisons of NMEs obtained with various nuclear structure and the NMEs of ^{48}Ca are summarized in Tab. 1.2. The NME values have approximately triple times difference between the minimum and the maximum.

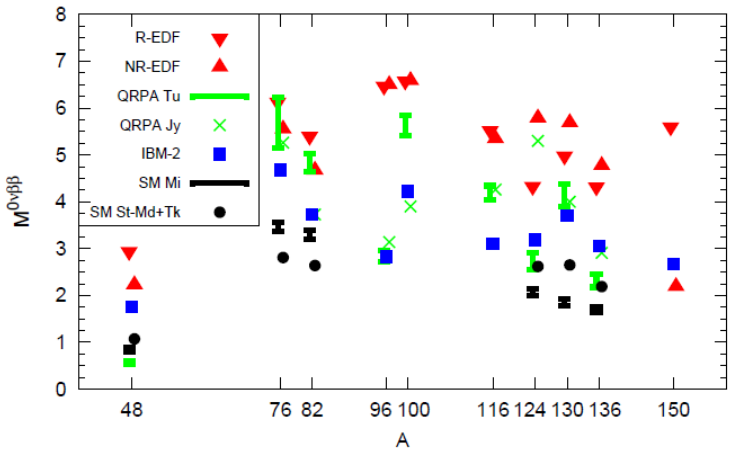

Figure 1.4: The values of nuclear matrix elements. "A" coresponds to mass number [9].

1.3 Experimental Searches for Double Beta Decay

An experiments for $0\nu\beta\beta$ decay observation requires large target nuclear mass, low background techniques and high energy resolution. A lot of experiments are located at underground laboratory in order to reduce of background from cosmic muon.

Table 1.2: The comparison of nuclear matrix elements for ^{48}Ca

NME model	NME value	Reference
SM St-Md + Tk	0.80 $\sim$ 1.18	[10], [11]
SM Mi	0.80 $\sim$ 0.88	[12]
IBM-2	1.75	[13]
QRPA Tu	0.54 $\sim$ 0.59	[14]
NR-EDF	2.37	[15]
R-EDF	2.94	[16]

1.3.1 Target Isotopes

Double beta decay isotopes are summarized in Tab. 1.3. There are several important keys for determining a double decay isotope for an experiment; ease of enrichment, long half-life of $2\nu\beta\beta$ decay and high Q value of the decay. If enrichment of nuclei is easy, a lot of target mass can be prepared for a detector. ^{136}Xe, ^{76}Ge, ^{130}Te, ^{82}Se, ^{100}Mo and ^{116}Cd can be enriched since their gas compounds are stable. $2\nu\beta\beta$ is an event which can not be reduced by analysis. If half-life of $2\nu\beta\beta$ is longer than other nuclei, background rate of $2\nu\beta\beta$ is reduced.

Table 1.3: Double beta decay nuclei

Isotope	$Q_{\beta\beta}$[keV]	Natural abundance [%]	${T_{1/2}}^{2\nu}$ [year]
^{48}Ca	4271	0.19	4.4×10^{19}
^{76}Ge	2039	7.8	1.55×10^{21}
^{82}Se	2995	9.2	1.33×10^{20}
^{96}Zr	3351	2.8	2.35×10^{19}
^{100}Mo	3034	9.6	7.11×10^{18}
^{116}Cd	2805	7.5	2.8×10^{19}
^{130}Te	2529	34.5	7.0×10^{20}
^{136}Xe	2476	8.9	2.30×10^{21}
^{150}Nd	3367	5.6	9.11×10^{18}

^{48}Ca has highest Q value in double beta decay isotopes. The background in detector is reduced using ^{48}Ca since Q value of ^{48}Ca is higher than almost all natural radiation.

1.3.2 Current Status and Future Prospects

The Heidelberg-Moscow experiment [17]

The Heidelberg-Moscow experiment studied $0\nu\beta\beta$ with 11 kg of enriched ^{76}Ge decay at the underground Laboratori Nazionali del Gran Sasso. The full running period is August 1990 - May 2003 and the collected statistic is 71.7 kg·yr. The detector of semiconducting Ge has high energy resolution and low background. The background in Q value region of ^{76}Ge achieved 0.11 events/(kg·y·keV). The observation of $0\nu\beta\beta$ was reported by a few members of the collaboration and the result of half-life and neutrino mass are

$$T^{0\nu}_{1/2} = (0.69 - 4.18) \times 10^{25} \quad (1.11)$$

$$\langle m_\nu \rangle = (0.24 - 0.58)\,[eV] \quad (1.12)$$

Almost the finite lifetime is reported, there are criticisms and it is almost excluded by the GERDA experiment as described later. Fig. 1.5 shows the energy spectrum around Q value region. The analysis method and estimation of background have questions.

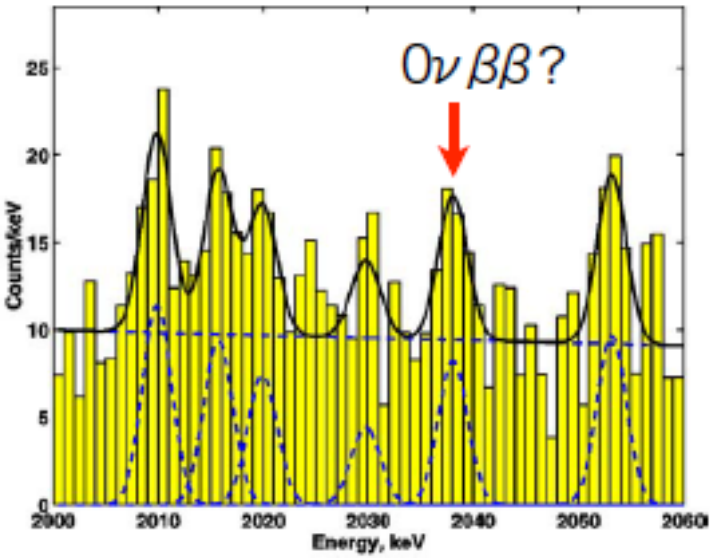

Figure 1.5: $0\nu\beta\beta$ energy spectrum of ^{76}Ge

The KamLAND-Zen experiment [18]

The KamLAND-Zen experiment studied $0\nu\beta\beta$ decay of ^{136}Xe with 13 tons of Xe-loaded liquid scintillator contained in the spherical inner balloon located at the center of KamLAND detector, which is located at the Kamioka observatory. After background reduction of ^{110m}Ag contamination, a lower limit for the $0\nu\beta\beta$ decay half-life is

$$T_{1/2}^{0\nu}\left(^{136}\mathrm{Xe}\right) > 1.07 \times 10^{26}\mathrm{yr}\,(90\%\ \mathrm{C.L.}) \tag{1.13}$$

and the effective Majorana neutrino mass is

$$\langle m_{\beta\beta}\rangle < (61 - 165)\,\mathrm{meV}\,(90\%\ \mathrm{C.L.}) \tag{1.14}$$

This result is the first constraint below 100 meV of all double beta decay isotopes.

The GERDA experiment [19]

The GERDA experiment studied $0\nu\beta\beta$ decay of ^{76}Ge with germanium detector enriched from 7.8% to 87% inside liquid argon. The GERDA experiment is located at the underground Laboratori Nazionali del Gran Sasso. Currently, the background level is achieved approximately 10^{-3} count keV^{-1} kg^{-1} yr^{-1}. A lower limit for the $0\nu\beta\beta$ decay half-life is

$$T_{1/2}^{0\nu}\left(^{76}\mathrm{Ge}\right) > 5.3 \times 10^{25}\mathrm{yr}\,(90\%\ \mathrm{C.L.}) \tag{1.15}$$

and the effective Majorana neutrino mass is

$$\langle m_{\beta\beta}\rangle < (0.15 - 0.33)\,\mathrm{eV}\,(90\%\ \mathrm{C.L.}) \tag{1.16}$$

The result of the Heidelberg-Moscow experiment is rejected by the GERDA experiment.

1.3.3 The ELEGANT VI experiment

The ELEGANT VI experiment studied neutrinoless double beta decay of ^{48}Ca and WIMPs at the Oto Cosmo observatory. Fig. 1.6 shows decay scheme of ^{48}Ca. Single β decay of ^{48}Ca to ^{48}Sc is strongly suppressed. This is due to spin selection rule. This detector consists of europium doped 23 CaF_2 CaF_2 (Eu) scintillators with $4.5 \times 4.5 \times 4.5$ cm^3 in size and total mass of 6.7 kg. The schematic view is shown in Fig. 1.7. Undoped CaF_2 (CaF_2 (pure)) crystals with $4.5 \times 4.5 \times 20$ cm^3 works as guides of light emitted from

CaF_2 (Eu) crystals. 38 thallium doped CsI (CsI (Tl)) scintillators with 6.5 × 6.5 × 25 cm^3 surround CaF_2 modules. CsI(Tl) and CaF_2(pure) scintillators works also as 4π active shields.

The result of limit on $0\nu\beta\beta$ with exposures of 4947 kg·day and they achieved zero background measurementis as follows [20].

$$T^{0\nu}_{1/2}\left(^{48}\mathrm{Ca}\right) > 5.8 \times 10^{22}\mathrm{yr}\,(90\%\mathrm{C.L.}) \tag{1.17}$$

The result of $2\nu\beta\beta$ half-life is as follows.

$$T^{2\nu}_{1/2}\left(^{48}\mathrm{Ca}\right) = 1.4^{+0.3}_{-0.2}\,(\mathrm{stat.}) \pm 0.5\,(\mathrm{syst.}) \times 10^{19} \tag{1.18}$$

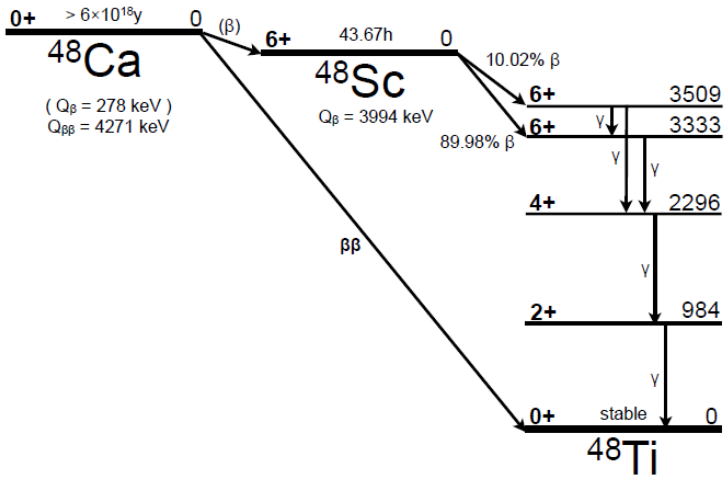

Figure 1.6: Decay scheme of ^{48}Ca. Single β decay of ^{48}Ca to ^{48}Sc is strongly suppressed. This is due to spin selection rule.

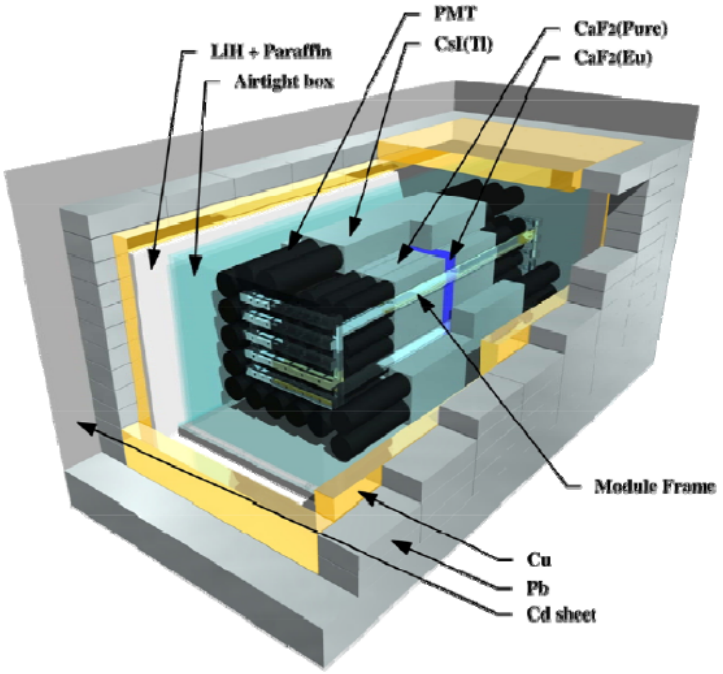

Figure 1.7: Schematic view of the ELEGANT VI detector

Chapter 2

The CANDLES Experiment

CANDLES stands for **CA**lcium fluoride for studies of **N**eutrino and **D**ark matters by **L**ow **E**nergy **S**pectrometer. We are studying $0\nu\beta\beta$ decay of ^{48}Ca in the CANDLES III detector. The Q value of ^{48}Ca is the highest among all $0\nu\beta\beta$ candidate nuclei. Taking of this advantage, we aim at achieving background free measurement. The CANDLES detector is located 1000 m underground (2700 m of water equivalent) at the Kamioka observatory. Surrounding rock reduces the intensity of cosmic muon by 10^{-5} over that of at surface laboratories. In this chapter, CANDLES III is introduced in detail.

2.1 The CANDLES III Detector

Fig. 2.1 shows a schematic view. The CANDLES III detector consists of a stainless steel tank of 3 m diameter $\times$ 4 m height in size, 96 CaF_2 modules and 2000 L liquid scintilator (LS) contained in. The CaF_2 module (Sec. 2.1.1) and LS (Sec. 2.1.2) are inside acrylic tank with a size of 1.4 m diameter $\times$ 1.4 m height. The scintillating light of CaF_2 crystals and LS is observed by three types of PMTs (Sec. 2.2.1). Lead and Boron shield (Sec. 2.1.3) are installed covering stainless steel tank to reduce external natural gamma rays and neutrons. Temperature of the CANDLES III detector is cooled down to about 4 °C to increase the light yield of CaF_2 crystal (Sec. 2.1.4).

2.1.1 CaF_2 Module

The CaF_2 module is composed of two materials that are CaF_2 crystal and Wave Length Shifter (WLS) in Fig. 2.1. A CaF_2 crystal emit ultraviolet light (Fig. 2.2). The WLS is used to convert the ultraviolet light to visible light which is sensitive to PMTs [21]. The number of CaF_2 modules is 96 and 365

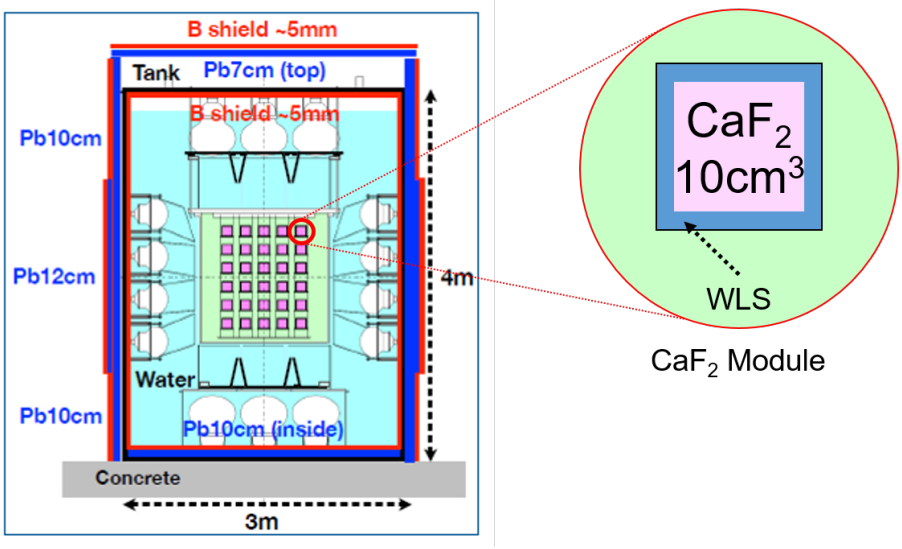

Figure 2.1: Schematic view of the CANDLES III detector and CaF_2 module.

g of ^{48}Ca are included in total. The size of CaF_2 crystals is 100 mm × 100 mm × 100 mm. Table 2.1 shows the composition of WLS. The thickness of WLS is 5 mm. The thickness was determined to minimize dead layer since WLS is not scintillator and to keep conversion effecting high enough. The ultraviolet light emitted from CaF_2 crystals is absorbed by LS. Therefore, WLS is set close to CaF_2 crystal in Fig. 2.1.

Table 2.1: The property of wavelength shifter

	Solvent	Solute
Material	Paraol250	Bis-MSB (0.1 g/l)

2.1.2 Liquid Scintillator (LS)

Liquid scintillator acts as an active shield. The decay time constant of the LS which is defferet from that of CaF_2 realizes the active shield quite effective. CaF_2 crystal has decay time constant about 1 μs. By contrast, LS has decay time constant about few tens ns. We use these characteristics to veto external background as called 4π active shield. Detail of 4π active shield will be explained later. Table 2.2 is component of LS.

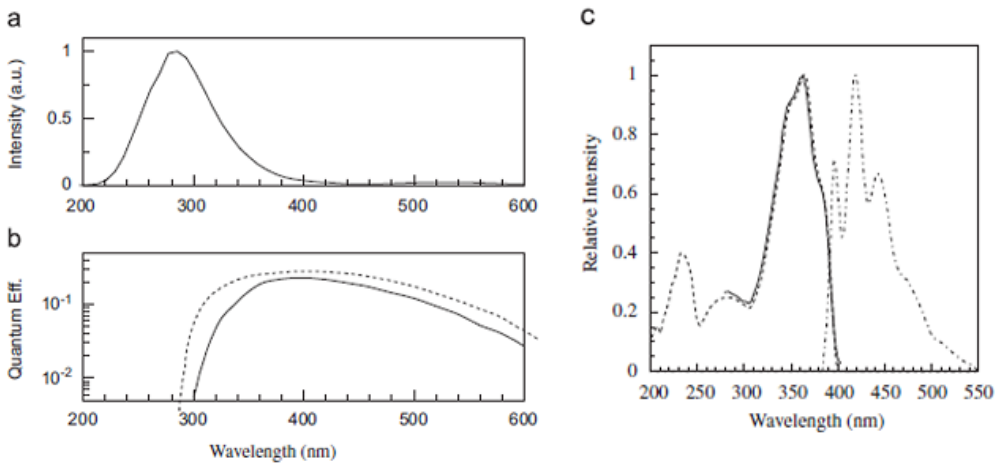

Figure 2.2: Property of wavelengh conversion system (a)Emission Wavelength spectrum of CaF_2 [21]. (b)Sensitivity of 13 inch and 2inch PMTs. The solid curve is 13 inch. The dashed curve is 2 inch. (c)The absorption and emission curve of bis-MSB.The absorption is solid curve and the emission curve is dashed.

Table 2.2: The property of Liquid scintillator

	Solvent		Solute	
Material	Paraol250	Pseudocumene	PPO	Bis-MSB
Component	80%	20%	1.0 g/l	0.1 g/l

2.1.3 Lead and Boron Shield

We know one of the main background is high energy gamma rays above Q value of ^{48}Ca. These gamma rays are emitted by neutron capture reactions ((n, γ) reactions) in surrounding rock and the CANDLES Ⅲ detector. The detail of (n, γ) background will be discussed later. In the CANDLES Ⅲ detector, there are two major origins of (n, γ) reactions. One is the rock surrounding the CANDLES Ⅲ detector, and other is the stainless steel tank that is contained in the CANDLES Ⅲ detector, reserver tank for LS and so on. We must shield the detector from entering neutrons and gamma rays. We designed the shield using Monte Carlo simulation (MC). Construction of the shield started in 2015 and finishd in 2016.

The shield consists of two materials as lead (Pb) block and silicon rubber sheet with 40 wt% of boron carbide (B_4C) that is called B rubber sheet. Pb shield reduces rock (n, γ) events and B rubber sheet captures neutron entering the CANDLES Ⅲ detector. In the case of Pb side shield, thickness of 10 cm is enough to reduced several MeV gamma rays and top shield is limited to 7 cm in thickness, because of maximum weight. Center of side tank is thickness of 12 cm to compensate PMT thickness which reduce shielding power of water. Boron rubber sheet is thickness of 5 mm. We installed inside of the CANDLES Ⅲ detector and outside of Pb shield in Fig. 2.1. Non-thermal neutrons enter the detector and are thermalized by water passive shield. Boron rubber sheet inside of stainless tank absorb these thermal neutron.

2.1.4 Cooling System

The light yield of CaF_2 crystal increases at low temperature [22]. The temperature dependence of scintillation light yield of pure CaF_2 crystal was measured 8 - 305 K using the multiphoton counting technique by other experimental group.

The light yield of temperature dependence was evaluated by CaF_2 module. The result studied in Osaka university is summarized in Tab. 2.3 [23]. The light yield is increased and the energy resolution at 0 °C is better than that at 20 °C same as previous experiment. Additionally, the ability of pulse shape discrimination at 0 °C is also better than that at 20 °C.

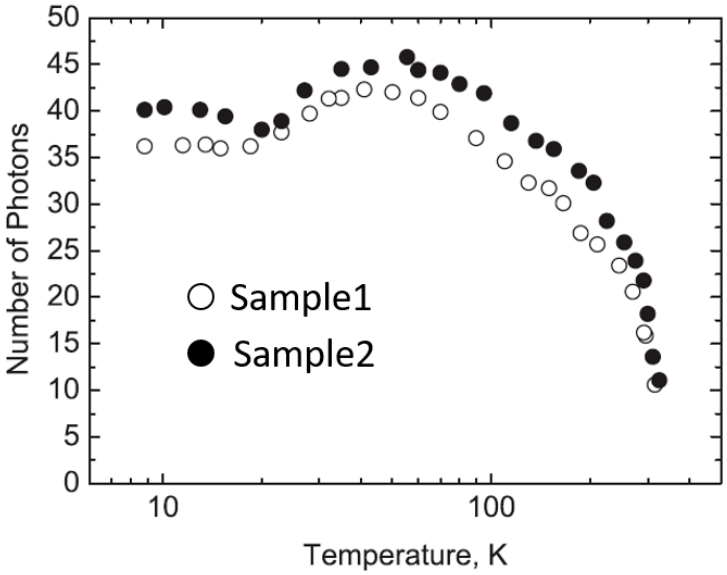

Figure 2.3: Light yield in CaF_2 as a function of temperature. Both sample1 and sample2 are pure CaF_2 crystal.

Table 2.3: The result of cooling experiment at Osaka university using gamma ray of 662 keV.

	20 °C	0 °C	Ratio
Light yield (ch)	1008 ± 1	1360 ± 1	× 1.35
σ (%)	7.07 ± 0.05	6.43 ± 0.03	

2.2 Data Acquisition

2.2.1 Photomultiplier Tube (PMTs)

The CANDLES Ⅲ detector has three types of PMTs. The first one is 20 inch PMTs. We set 20 inch PMTs on top and bottom of the CANDLES Ⅲ detectors. The second one is 13 inch PMTs, we set on side of the detectors. The last one is 10 inch PMTs. These PMTs have faster time response than 13 and 20 inch PMTs. We expect to improve rejection efficiency of LS events by Pulse Shape Discrimination (PSD). I summarized the characteristics of each PMT in Tab. 2.4. Fig. 2.4 shows schematic view of PMTs.

Table 2.4: The characteristics of three types of PMTs

Product Name	R7250	R8055	R7081
Diameter	508 mm (20 inch)	332 mm (13 inch)	253 mm (10 inch)
Photocathode material	Bialkali	Bialkali	Bialkali
Dynode	10 stage Box&Line	10 stage Box&Line	10 stage Box&Line
Spectral Response	300 to 650 nm	300 to 650 nm	300 to 650 nm
Peak Wavelength	420 nm	420 nm	420 nm
Gain	5.0×10^7 (at 2000 V)	1.0×10^7 (at 2000 V)	1.0×10^7 (at 1500 V)

2.2.2 Electronics and Trigger System

We designed the data acquisition system (DAQ) [24] in order to efficiently collect pulse shape data for each PMT. The scintillation lights of CaF_2 crystals and LS are simultaneously detected by 62 PMTs. Raw signals send to amplifier electronics modules through BNC cables of about 30 m. After amplified analog signals are converted to digital signals by Flash A/D Converter (FADC) and are recorded pulse shape of each PMT [25], [26]. This FADC digitizes the signal to an 8 bit value in every 2 ns.

Pulse shape of first 768 ns is recorded by 2 ns using 384 channels. Next 8.2 μs is recorded by 64 ns using 127 channels. Then total pulse shape information is 8.96 μs as (Eq. 2.1)

$$2\,\text{ns} \times 384 + 64\,\text{ns} \times 128 = 8.96\,\mu\text{s} \tag{2.1}$$

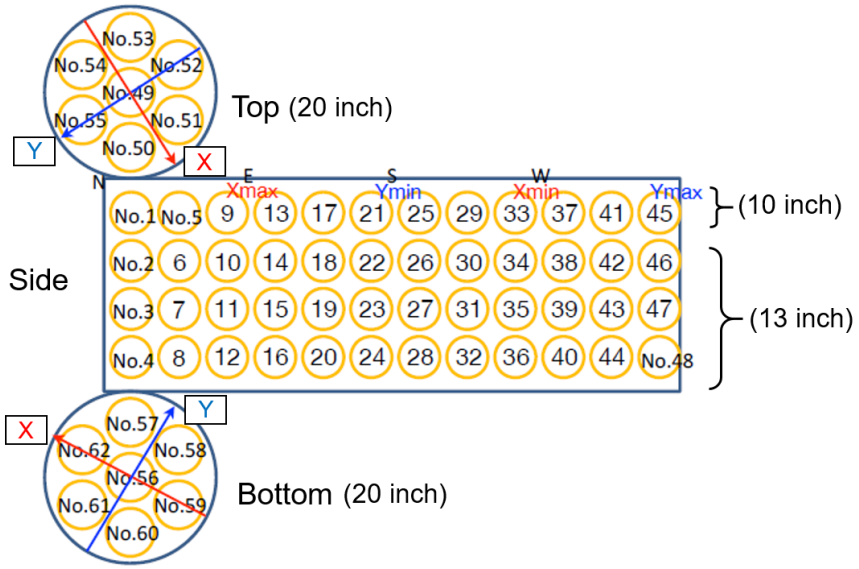

Figure 2.4: PMT Layout of the CANDLES Ⅲ Detector

Dual Gate Trigger [27]

We take the CaF_2 events with Dual Gate Trigger (DGT). This trigger system can reject LS pulse events only by the integrated digital pulse of two gate as S1 and S2 (Tab. 2.5). The waveform of CaF_2 can exceed the threshold of two gates since the decay time constant is longer than the delay time between S1 and S2. Waveforms of events taken by DGT can be categoriszed into 3 types as follows. We can take three types waveform as follows.

- Waveform of CaF_2 crystal
- Waveform of CaF_2 crystal added LS pulse
- Accidental double pulse

The second and third one can be rejected by pulse shape discrimination. I will explain about pulse shape discrimination later.

Minimum Bias Trigger

Minimum Bias Trigger(MBT) which is to take data without applying bias acquire almost LS event. The reference pulse of LS is used by MBT events

Table 2.5: Setting of Dual Gate Trigger

Gate	Time Width [ns]	Threshold [ADC Count]	Delay Time [ns]
S1	128	3026	384
S2	168	3158	0

and we studied overshoot and overflow of LS pulse. Trigger threshold of MBT is 0.5 times of DGT and gate width is 64 ns. Trigger rate after pre-scale is adjusted to 1 Hz, which is 1/2000 of original rate.

2.2.3 Energy threshold

Energy threshold is checked crystal by crystal because light yield has crystal dependence. We installed Low Dual Gate Trigger with lower threshold than DGT. Energy threshold of each crystal is analyzed by coincidence events of two triggers. The number of events taken by DGT is compared by the number of events taken by Low DGT and the acquirement efficiency of DGT is estimated. Fig. 2.5 shows energy threshold of 90% of each crystal. Average energy threshold is about 769 keV. This is enough low to take a ^{212}Bi alpha ray whose visible energy is about 1.6 MeV. As will be described later, this event is an important event for rejecting the background of $0\nu\beta\beta$ decay. ^{40}K gamma ray (1.46MeV) also can be taken and we check detector performance by ^{40}K events.

2.3 Characteristic of Pulse Shape

As described previous section, observed waveform in the CANDLES Ⅲ detector can be categorized into three types as shown in Fig. 2.6.

1. Waveform of LS
2. Waveform of CaF_2 added LS
3. Waveform of only CaF_2 crystal

The first one is rejected by DGT (Sec. 2.2.2). The second one is almost external background and called CaF_2+LS event. The third one has two kinds of waveform as alpha pulse and beta pulse. The origin of alpha and beta pulse are internal and external radiation. CaF_2 crystals are contaminated by ^{238}U, ^{232}Th and ^{235}U. Their contaminations emit some kinds of alpha ray and beta ray. In addition, environmental gamma ray as ^{40}K and ^{208}Tl

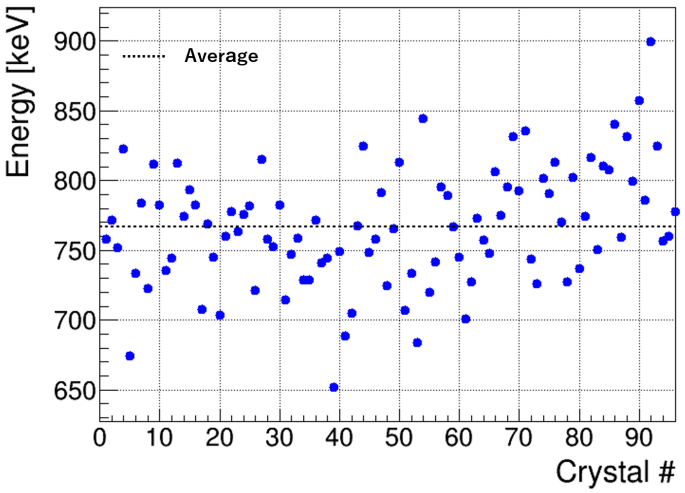

Figure 2.5: Energy threshold of each crystal of 90%. The average energy threshold is about 769 keV

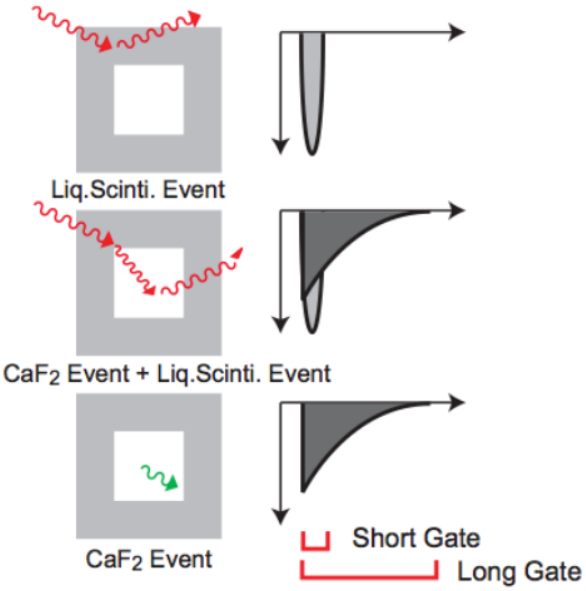

Figure 2.6: Characteristic of waveform in the CANDLES III detector. White square means CaF_2 crystal and gray region means LS. The decay time constant of CaF_2 crystal is longer than LS.

come from component of the CANDLES Ⅲ detector and outside of detector. Gamma rays energy transfer their energy to electron by photoelectric effect or compton scattering and the electron in CaF_2 crystals or LS. The CANDLES Ⅲ detector observe gamma ray waveform same as beta ray when the gamma ray is fully cntained in the CaF_2 crystal

We define Ratio parameter due to separate only CaF_2 and CaF_2+LS pulse.

$$\text{Ratio} = \frac{\text{Short Gate}}{\text{Long Gate}} \tag{2.2}$$

where short gate means integral value from start channel of waveform to 200 ns and long gate means integral value from start channel of waveform to 4μs in Figure2.6. I show the relation between Energy and Ratio in Figure2.7. The ratio of LS events appears about 1 and CaF_2 one appears from 0.12 to 0.22. There is difference between alpha ans beta waveform of CaF_2 crystal. The alpha events are around 0.2 at 1.4 MeV and the beta events are 0.12. Distinction of alpha event and beta event within a waveform is essential in $o\nu\beta\beta$ decay study. I will explain its details in Sec. 5. The event described around 1.4 MeV is ^{40}K gamma ray. The energy of ^{40}K gamma ray becomes smaller as the ratio becomes larger because the light yield is different between CaF_2 crystal and LS. So it is important to calibrate the energy of each scintillator.

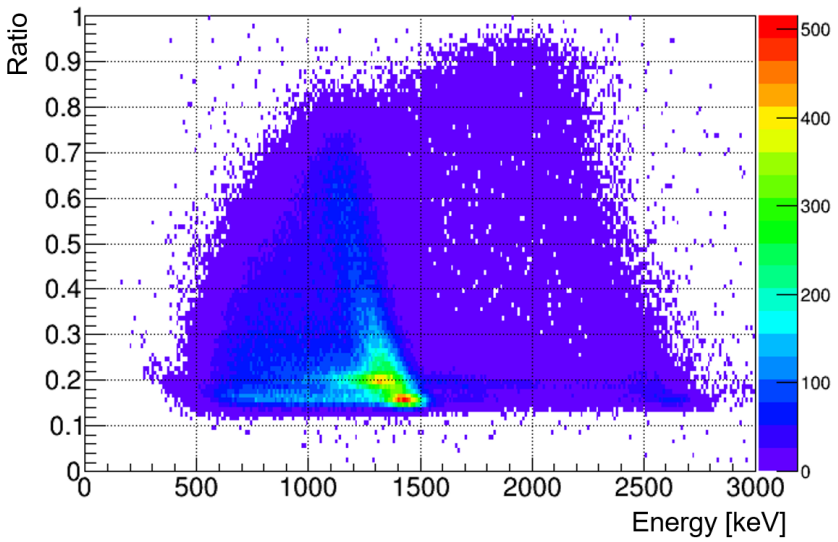

Figure 2.7: 2D histogram of Ratio and Energy.Draw using data of about one day.

Chapter 3

Event Reconstruction

Event position and energy are reconstructed by observed waveform with 62 PMTs. The flow of analysis is as follows.

1. Event quality check (Sec.3.1)
2. Timing correction of each PMT waveform (Sec.3.2)
3. Integration of charge
4. 1p.e. gain calibration (Sec.3.3)
5. Position reconstruction (Sec.3.4)
6. Energy reconstruction (Sec.4)
7. Pulse Shape Discrimination (Sec.5)

Our analysis have two steps called "PreAnalysis" and "Candles main Analysis Tool(CAT)". PreAnalesis processes from first to third above itemization and CAT processes the others. After process of CAT, we evaluate the stability of some parameters and detector.

3.1 Event Quality check

Good and bad example waveform are shown in Figure3.1. The events are categorized into good or bad events by PreAnalysis. Fig.3.1-(a) shows a only CaF_2 event and Fig.3.1-(b) shows a CaF_2+LS event. They are categorized into good events. Some bad events can be accidentally triggered by the CANDLES Ⅲ DAQ system. The criteria of bad event are as follows.

- Event with saturated PMT signal (Fig.3.1-c).

- Start channel error (Fig.3.1-d). There is no start channel in first 512 ns range.
- Event with overshoot PMT signal (Fig.3.1-e)

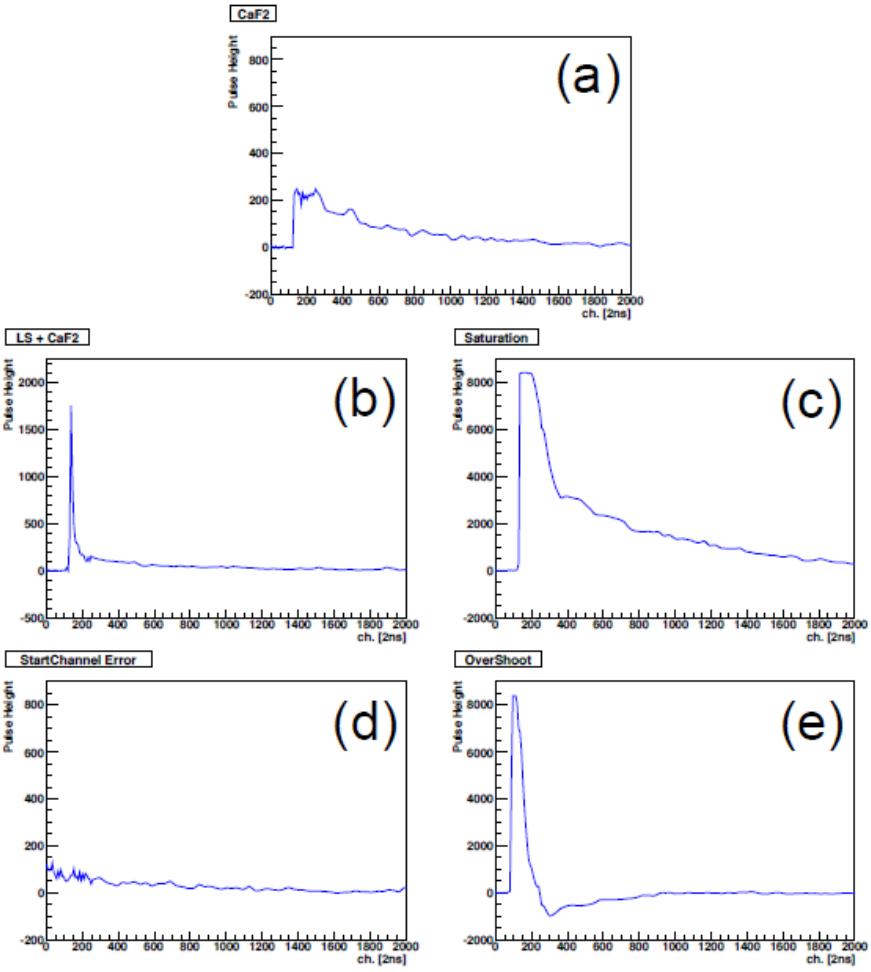

Figure 3.1: Good and bad sample events. (a)A only CaF_2 event. (b)A CaF_2+LS event. (c)A event saturated PMT signal. (d)A event of start channel error. (e)A event with overshoot PMT signal.

3.2 Timing Correction

We add 62 waveforms of PMTs and use sum waveform for analyzed energy reconstruction, Pulse Shape Discrimination (PSD). The cable length from each PMT to FADC is different. Also the applied voltage of each PMT is different. Therefore, it is necessary to adjust timing at start channel (SCHANNEL) of each PMT. The start channel means rise of waveform and defines a channel that 20 counts away from the pedestal.

The reference SCHANNEL is defined as that of PMT2. The difference between the SCHANNLE of each PMT and the reference SCHANNEL is defined as following equation.

$$\text{SCHANNEL Diff (i)} = \text{SCHANNEL (i)} - \text{SCHANNEL (2)} \tag{3.1}$$

Where i is PMT number($1 \sim 62$). LS events are used for making SCHANNEL Diff distribution because the rise time of LS is faster than CaF_2. The events around center of acrylic tank are selected to avoid artificial offset due to time of flight. The each SCAHNNEL Diff is distributed like Fig. 3.2 and is fitted by Gaussian function.

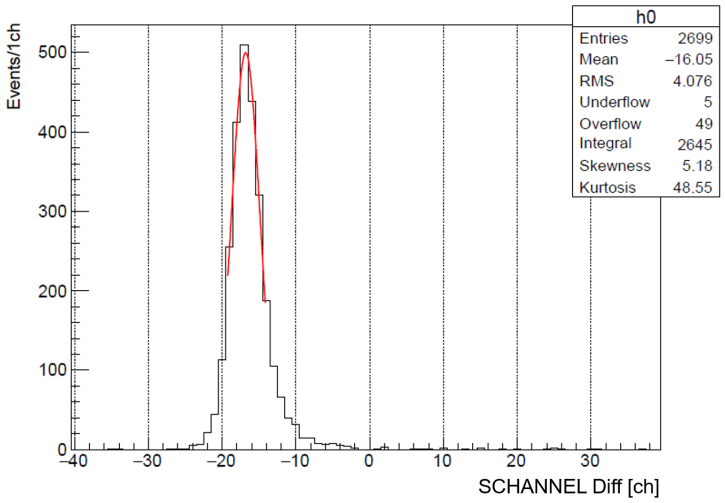

Figure 3.2: Distribution of SCHANNEL Diff. This is distributed by PMT 21.

Fig. 3.3 shows LS waveform before and after timing correction. The width of LS in the right figure of Fig. 3.3 is narrower than the left figure. We check whether all data is corrected with the same quality. Fig. 3.4 shows

time stability of average SCHANNEL Diff of 62 PMTs after corrected timing. All plot in Fig. 3.4 is stable under 1 ch.

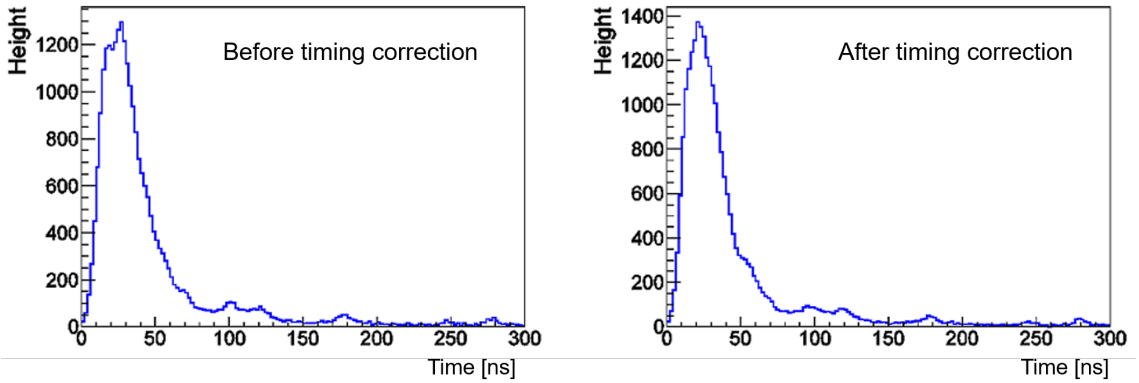

Figure 3.3: Comparison of waveform before and after timing correction

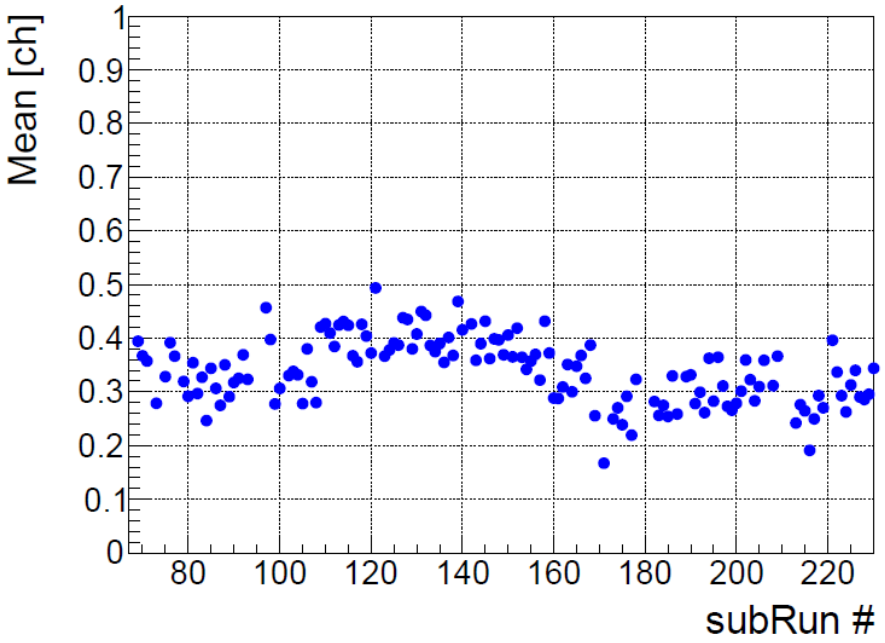

Figure 3.4: Time stability of SCHANNEL Diff. Mean is average SCHANNEL Diff of 62 PMTs.

3.3 1 Photo Electron Gain Correction

In the CANDLES detector, 1 photo electron (1 p.e.) is introduced to evaluate the stability of PMTs. Furthermore, we use integral value of 1 p.e. to reconstruct energy and position. Even if the gain of PMTs varies, energy and position parameter is stable by considering time dependence of 1 p.e. gain. We check stability of 1 p.e. gain ant rate to evaluate the PMT status.

1p.e. events are taken by clock trigger. Clock trigger is taken forcibly data at 3 Hz. We use the start channel for 1 p.e. to search 1 p.e. candidate in 0 to 450 ns region. The start channel for 1 p.e. defined as continuous 2 channels that have above 2 count away from pedestal. 1 p.e. events are integrated ± 60 ns from peak of waveform and 0 p.e. events are integrated from 330 ns to 450 ns. Fig. 3.5 shows example waveforms of 1 p.e. and 0 p.e. and integrated region. Then, each integrated value is filled in histograms (Fig. 3.6). The red histogram describes 1 p.e. distribution and the black one describes 0 p.e.. Fig. 3.6 shows example distribution of each kind of PMT. The mean value is calculated from 1 p.e. distribution and this value defines 1 p.e. gain. 1 p.e. gain is calculated for each PMT and each sub Run which corresponds to almost 1 day. Fig. 3.7 shows the gain of each PMT. We set 1 p.e. gain to under 70 ch and all plots of 1 p.e. gains distribute under 70 ch in Fig. 3.7. The Average of 1 p.e. gain is calculated to be 59 ch.

I check time stability of 1 p.e. gain and rate to estimate data quality. The rate is defined as follows equation.

$$\text{Rate (i)} = \frac{\text{Number of 1 p.e. events (i)}}{\text{Total event of clock trigger}} \tag{3.2}$$

Fig. 3.8 shows time stability of average gain and rate of 62 PMTs and I check gain and rate stability for each PMT. All plots is stable in both figures.

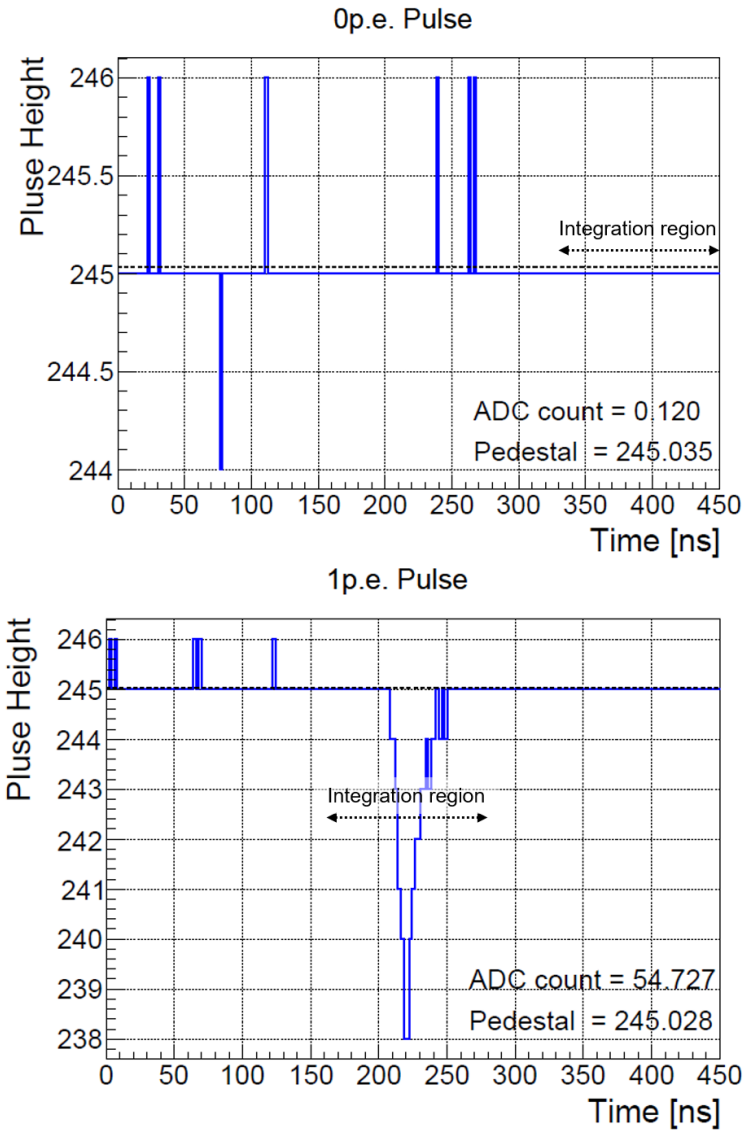

Figure 3.5: 1 p.e. and 0 p.e. example waveform. These are waveform of 13 inch PMT.

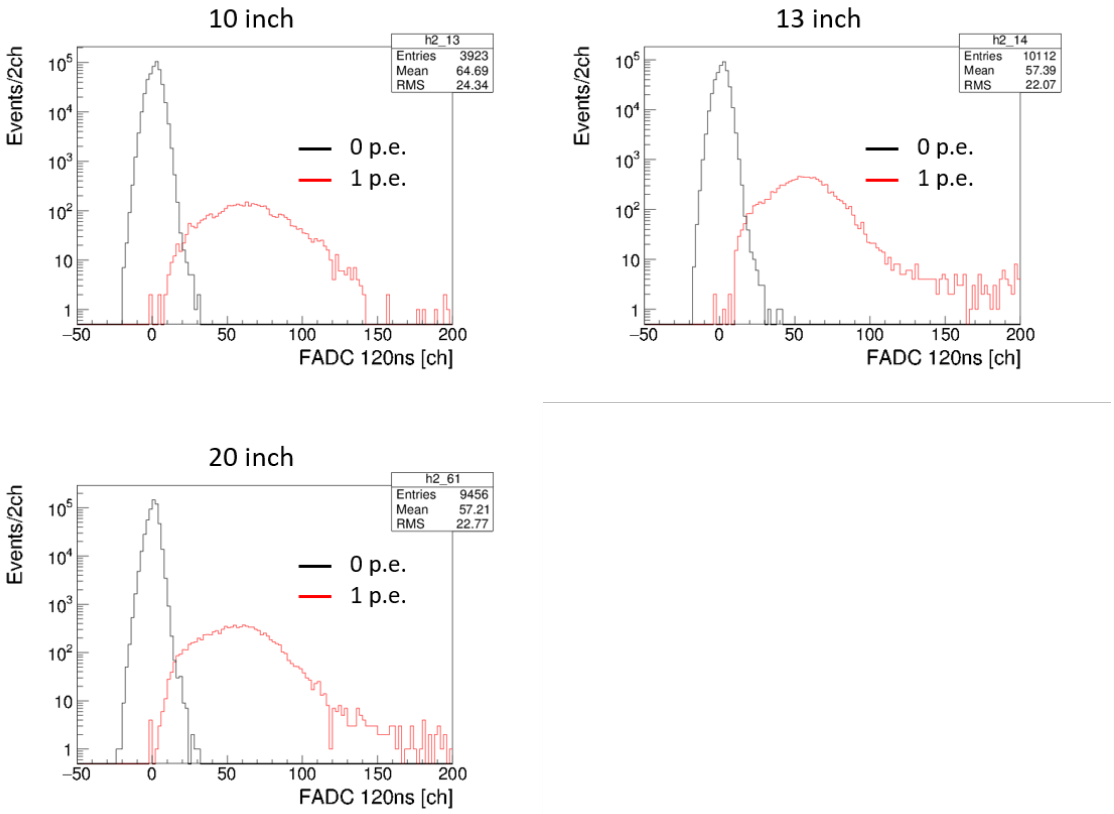

Figure 3.6: 1 p.e. and 0 p.e. distribution of each PMT. The red line corresponds to 1 p.e. and the black line corresponds to 0 p.e..

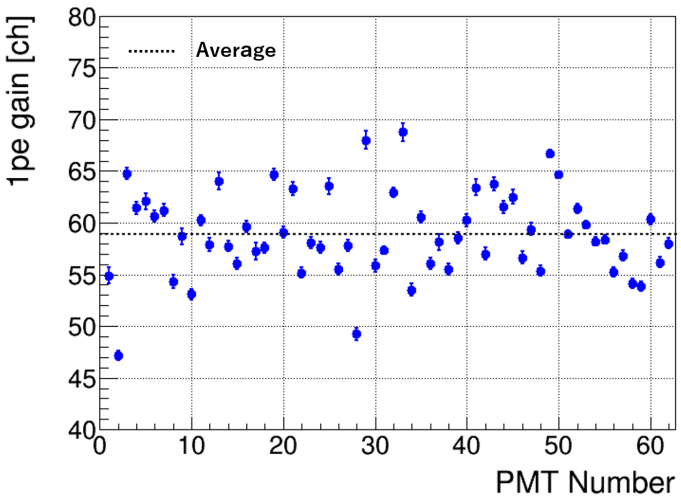

Figure 3.7: 1 p.e. gain of each PMT. Average 1 p.e. of each PMT is 59 ch.

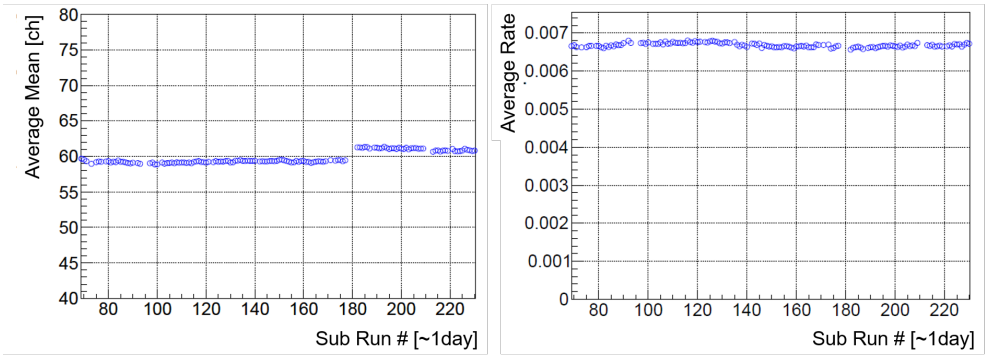

Figure 3.8: The time stability of average 1 p.e. gain and rate

3.4 Crystal Position Reconstruction

We have to know in which crystal gamma ray deposits energy since light yield of each crystal differs from crystal by crystal. Also, it is important to analyze decay with short half-life in ^{238}U and so on. For example, it is ^{219}Rn - ^{215}Po sequential decay in ^{235}U chain. As I explained in the Sec. 2.1.1, the size of CaF_2 crystal is cube with a side of 100 mm. The distance between crystals and layers is 100 mm. We define crystal number and each axis as Fig. 3.9. The 1st layer is near the top of the CANDLES Ⅲ detector . Crystals with

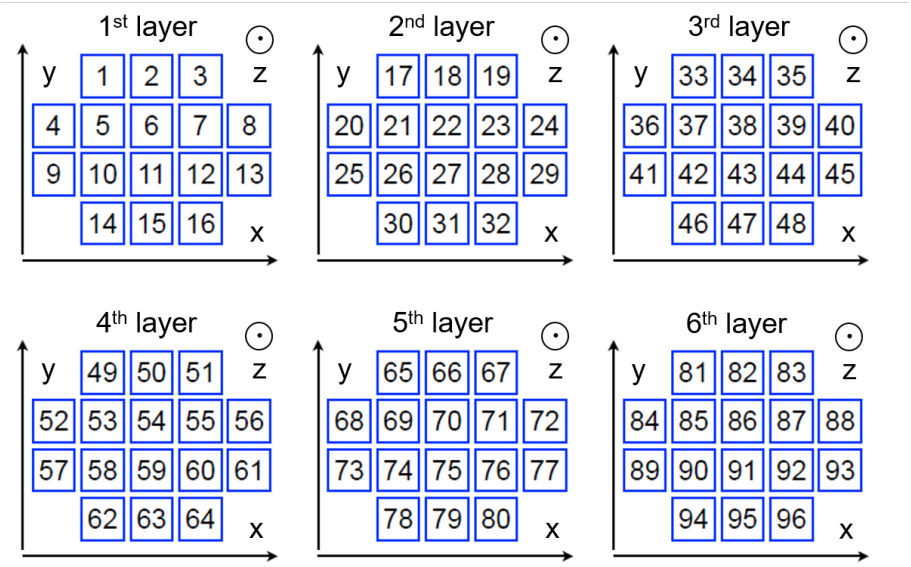

Figure 3.9: CaF_2 crystal layout of the CANDLES Ⅲ detector

a lot of radioactive contamination of ^{232}Th are installed in upper layer and crystals with low contamination are installed the middle layer because the 4π shield and lead shield works effectively for the center region. The detail of the contamination is explained in Sec. 6.2. The Cr11 called calibration crystals is most contamination of ^{238}U and ^{232}Th. This crystal is used to study of alpha waveform and some alpha backgrounds.

We use weighted mean method of number of photo electrons to reconstruct position as following equation.

$$\overrightarrow{r} = \frac{\sum \mathrm{NPE\,(i)} \times \overrightarrow{\mathrm{PMT\,(i)}}}{\mathrm{NPE\ Total}} \tag{3.3}$$

Where $\overrightarrow{r}$ is position vector as (x, y, z). i is PMT number $(1 \sim 62)$. NPE is

number of photo electrons. $\overrightarrow{\mathrm{PMT}}$ is position vector of each PMT. NPETotal is total number of photo electrons of a event.

Fig. 3.10 shows reconstructed position of ^{208}Tl gamma events. Events are projected to each axis and we obtain the mean and sigma of each crystal by Gaussian fitting. Fig. 3.11 shows the example distribution of each axis. At this analysis, ^{40}K events that are the most statistic are used by about 10 sub Runs same as about 10 days around beginning of physics data. Fig. 3.12 shows the sigma value of each axis and crystal. Every sigma value is smaller than distance of between crystals such as 100 mm. The average sigma of each axis is summarized in Tab. 3.1. In all energy region, selection region of the central crystal for each axis is determined by this result. From above, we can identify the crystal in which event occur.

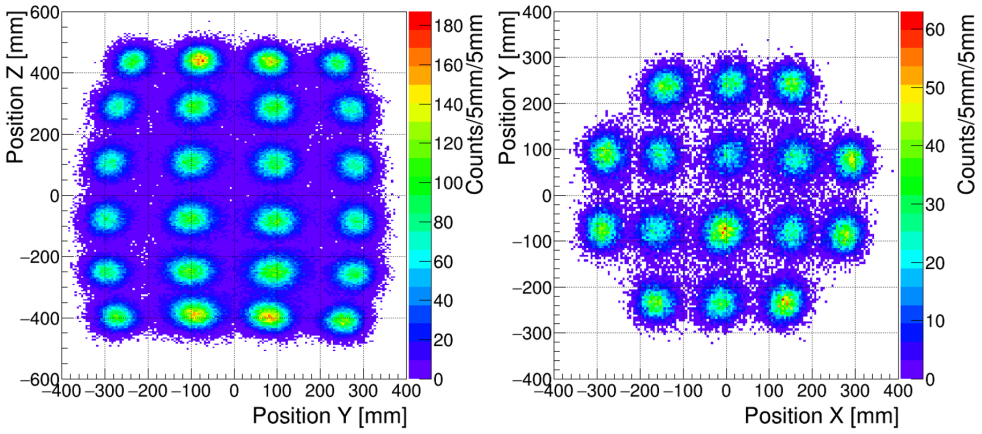

Figure 3.10: The distribution of reconstruction position by ^{208}Tl events. The left figure describes from side view (y-z axis). The right figure describes 1st layer from top view (x-y axis).

Table 3.1: The average sigma of each axis.

σ	Average [mm]
X	29.43 ± 0.03
Y	28.92 ± 0.03
Z	32.91 ± 0.03

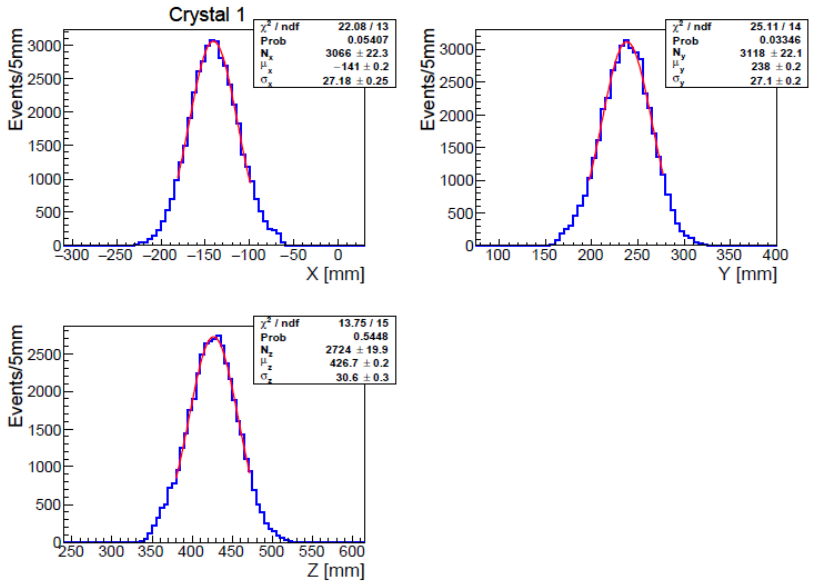

Figure 3.11: The example distribution of each axis. These distributions are Cr1.

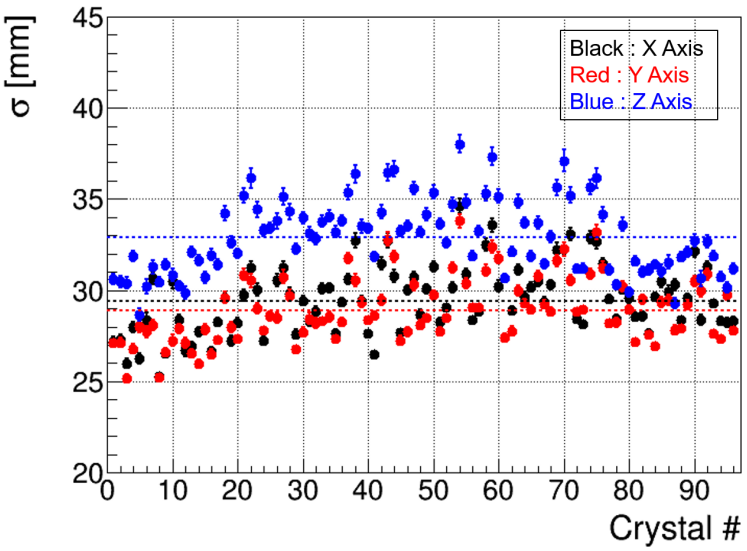

Figure 3.12: The sigma value of each axis and crystal.

The sigma value of each axis have energy dependence. As explained above, the position reconstruction is analyzed by gamma ray of ^{40}K. Therefore, it is necessary to evaluate the sigma value at Q value region and the detection efficiency of position selection for $0\nu\beta\beta$ decay. The physics data is low statistic around Q value region and above energy region. Hence, neutron calibration data is used for this analysis because the (n, γ) reactions is emitted the gamma ray with higher energy than Q value region. Neutron calibration will be explained in next chapter. Even if neutron calibration data is used, the energy dependence of sigma of each crystal cannot be analyzed. Therefore, the energy dependence of average sigma of all crystals for each axis is estimated. Fig. 3.13 shows the energy dependence of average sigma for each axis and each plot is fitted by following equation.

$$\sigma = \frac{a}{\sqrt{\text{Energy}}} + b \tag{3.4}$$

Where " a " and " b " are free parameter. The result of fitting as " a " and " b " is summarized in Tab. 3.2. The sigma value of each axis at Q value is calculated by the fitting result. Then, the ratio of average sigma in Tab. 3.1 and sigma at Q value for each axis is obtained. The results of the sigma at Q value and ratio are summarized in Tab. 3.2. From above, the detection efficiency of position cut for $0\nu\beta\beta$ decay can be estimated.

Table 3.2: The fitting result of energy dependence and the sigma value at Q value. Ratio corresponds the average sigma value divided by the sigma value at Q value.

Axis	a	b	σ at Q value [mm]	Ratio
X	707.2 ± 5.4	10.15 ± 0.13	20.97	1.40
Y	716.1 ± 5.2	9.52 ± 0.13	20.47	1.41
Z	955.0 ± 5.3	7.07 ± 0.13	21.68	1.52

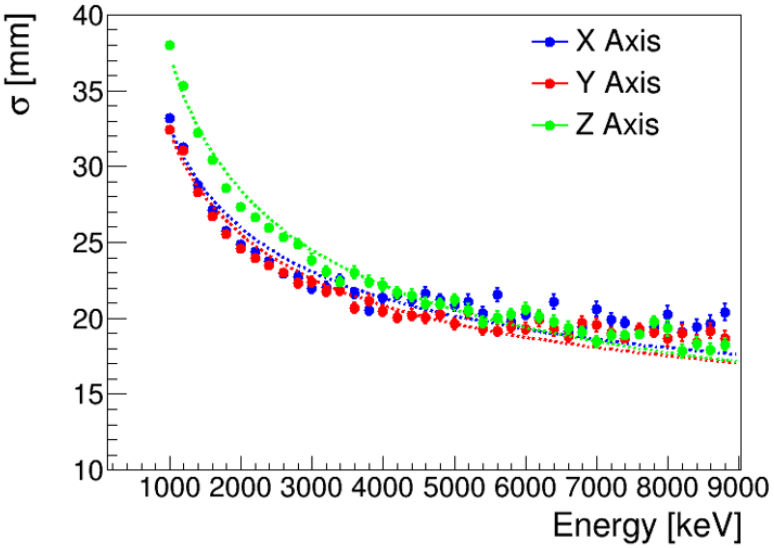

Figure 3.13: The energy dependence of position sigma value. This study is analyzed by neutron calibration data because gamma ray events of (n, γ) reactions exist from 5 MeV to 10 MeV. The function as 3.4 fit to sigma value of each axis.

Chapter 4

Energy Reconstruction and Estimation

Observed energy is calculated from integrated charge for 4 μsec from the start channel. Energy is calculated by following equation,

$$\text{Energy} = \text{F}\,(\text{i}) \sum_{\text{m}=1}^{62} \text{NPE}\,(\text{m}) \tag{4.1}$$

where F(i) is energy calibration factor, i is crystal number, NPE(m) is the number of photo electrons, m is PMT number. Energy calibration factor need to be determined crystal by crystal, because the light yield depends no crystal. Energy calibration factor of each crystal is obtained by ^{88}Y source. Energy resolution and linearity are evaluated by gamma ray of neutron capture.

4.1 Calibration Sources

4.1.1 ^{88}Y Source

We use ^{88}Y source to determine F(i) in Eq. 4.1. ^{88}Y source emits 898 keV and 1836 keV gamma rays with electron capture and has a half-life of 106.6 days (Fig. 4.1). 1836 keV gamma ray that is closer than 898 keV is used for energy calibration factor. 898 keV gamma ray is near energy threshold that is around 800 keV as explained in Sec. 2.2.3. Therefore, data of this gamma ray cannot be taken efficiently.

We have to install ^{88}Y source close to crystals into the LS acrylic tank to calibrate energy to each crystal. There were some requirement to develop energy calibration system. ^{88}Y source is installed through the teflon tube

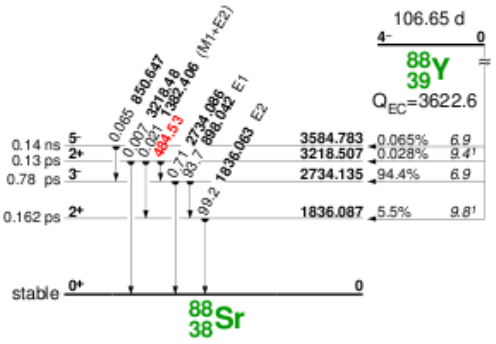

Figure 4.1: Decay scheme of ^{88}Y

with a diameter of 3/4 inch to avoid 20 inch PMTs. Hence, The size of ^{88}Y source is about 5 mm. As above requirement, we developed energy calibration system with a size of 300 × 200 × 200 mm for the CANDLES Ⅲ detector as Fig. 4.2 shows. This system is attached to top of the tank when the energy of each crystal is calibrated. Fig. 4.3 shows the schematic view of the jacket for ^{88}Y source and the size of source A stainless steel wire and a reel are attached to the calibration system. A jacket that is a diameter of 100 mm and a height of 220 mm is suspended. The diameter of ^{88}Y is 10 mm and the height is 22 mm to set in the jacket. The work of ^{88}Y installation near crystal is used the handle that is turned by hand. .

Fig. 4.4 shows the example of number of photo electrons spectrum in ^{88}Y. The three peaks can be observed in this figure. The middle peak corresponds to 1836 keV gamma ray and the left peak corresponds to 898 keV. The right peak is sum peak of 898 keV and 1836 keV. The sum peak with the energy of 2734 keV has a lot of accidental backgrounds contaminated by 2614keV gamma ray from ^{208}Tl. Hence, the sum peak can not be used energy calibration of each crystal. The peak of 1836 keV is fitted by Gaussian function, and mean and sigma value of 1836 keV peak is obtained. The resolution of energy is defined as following equation.

$$\text{Resolution} = \frac{\sigma}{\text{Mean}} \tag{4.2}$$

Fig. 4.5 shows mean values of 1836 keV gamma ray for each crystal. The energy scale of each crystal is calibrated by this result. The average of mean value is 1824.3 ± 0.2 p.e. and 993.6 ± 0.1 p.e./MeV is obtained. Fig. 4.6 shows resolution at each crystal. The average of resolution value is 4.01 ±

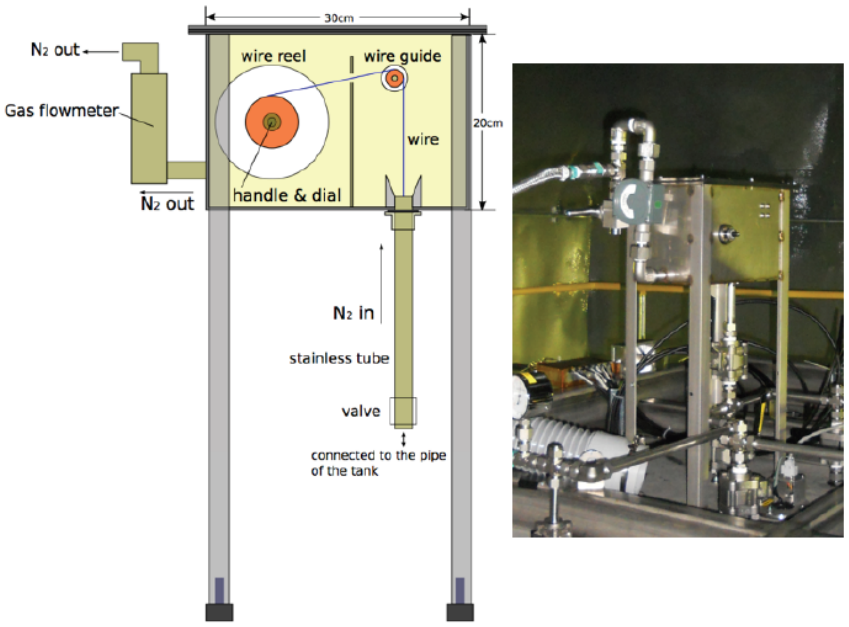

Figure 4.2: Energy calibration system

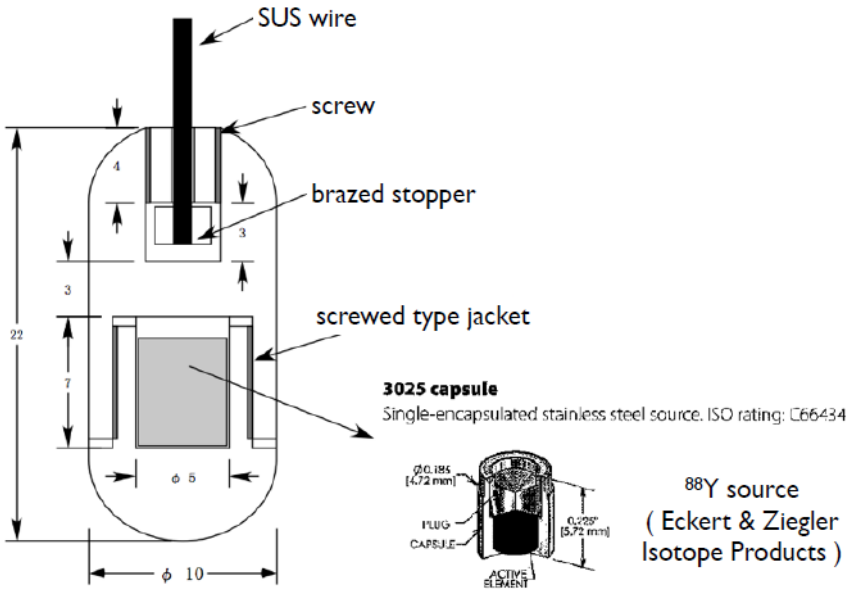

Figure 4.3: Size of ^{88}Y jacket and source

0.01%. The energy resolution at Q value of ^{48}Ca is discussed in Sec.4.2 by the result of ^{88}Y and neutron capture source.

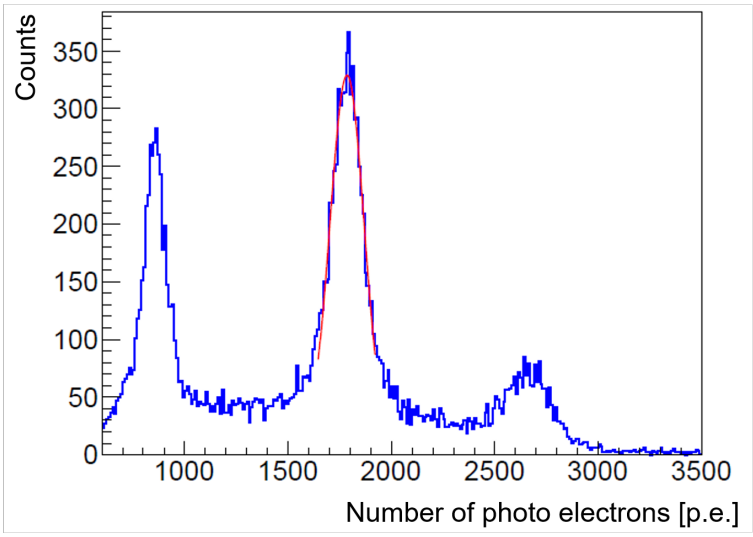

Figure 4.4: Energy spectrum in ^{88}Y. The middle peak corresponds to 1836 keV gamma ray and the left peak corresponds to 898 keV. The right peak is sum peak of 898 keV and 1836 keV.

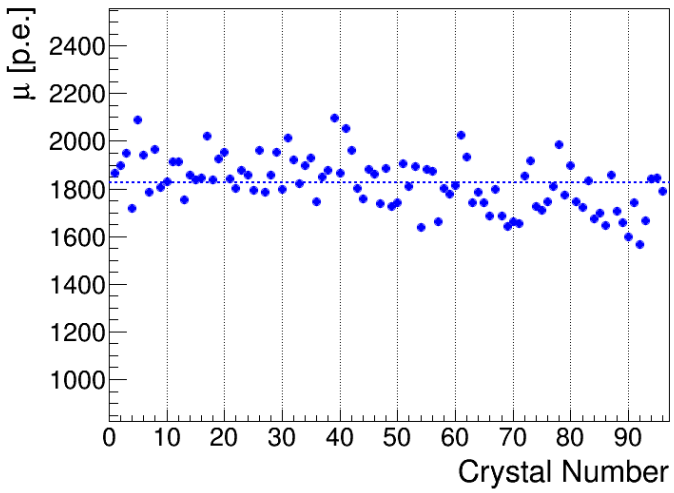

Figure 4.5: The mean value of ^{88}Y at each crystal. The average value is 1824 p.e..

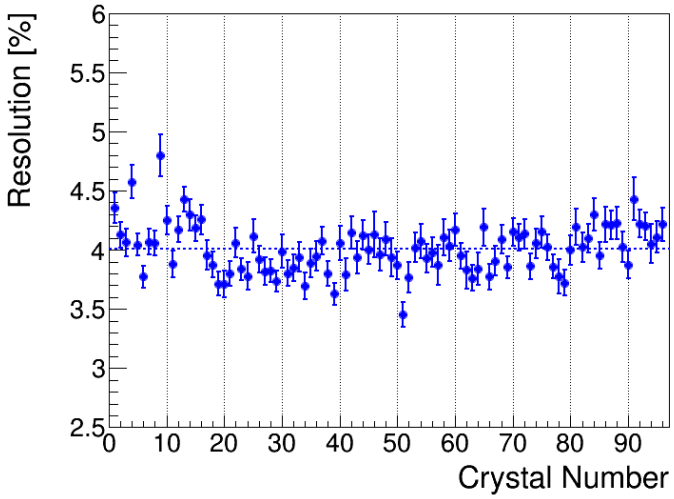

Figure 4.6: The resolution value of ^{88}Y at each crystal. The average value is 4.01%

4.1.2 Gamma ray with Neutron Capture

After the energy calibration by ^{88}Y, we need gamma ray source with energy around Q value or higher to estimate linearity and resolution at Q value region. In natural radioactive decay chain, there are no gamma ray above 3 MeV. However, gamma ray originated from neutron capture on nucleus could be even higher than Q value of 4.27 MeV. I summarize several useful nuclei for calibrated the CANDLES III detector in Tab. 4.1. The useful element

Table 4.1: Neutron cross section and energy of gamma ray

Element	Cross section [barn]	Energy of gamma ray [keV]
^{1}H	0.33	2223
^{28}Si	0.17	3539, 4934
^{56}Fe	2.56	7631
^{58}Ni	4.39	8534, 8994

of ^{1}H and ^{56}Fe is included in the CANDLES III detector as pure water and stainless steel. Hence, neutrino capture reaction is caused and gamma rays is emitted from stainless steel and water when neutron source that is ^{252}Cf is set on the detector. At this time, ^{252}Cf is surrounded by polyethylene for thermalization fast neutron from ^{252}Cf. On the other hand, ^{28}Si and ^{58}Ni are contained low in stainless steel. We develop new calibration system of neutron capture used ^{28}Si and ^{58}Ni. The form of ^{28}Si calibration system is consist of 36 blocks and each block size is 50 $\times$ 100 $\times$ 200 mm. The ^{58}Ni calibration system is 8 blocks with the size of 200 $\times$ 200 $\times$ 200 mm. I summarize the component of silicon and nickel in Tab. 4.2. Pb block is set close ^{252}Cf neutron source to shield gamma ray from ^{252}Cf.

Table 4.2: The composition of silicon and nickel block

Element	Component material	Ratio [%]
^{28}Si	Silicon	63.5
	High molecular polyethylene	16.5
	Adhesion bond (Araldite)	20.0
^{58}Ni	Nickel oxide	35
	Polyethylene + Adhesion bond (Araldite)	65

We calibrate previously energy scale of each crystal. Therefore, neutron calibration data is analyzed used events for all the crystals are summed up.

Gamma ray with neutron capture is emitted from the external of the detector. Therefore, we have to remove events of CaF_2 added LS waveform to calibrate using only CaF_2 events like $0\nu\beta\beta$. As details will be explained in next chapter, CaF_2 + LS events is removed by PSD.

Fig. 4.7 shows energy distributions of neutron calibration and the mean and resolution is obtained by fitting result. The energy distribution of ^{1}H in Fig. 4.7 has two peaks. The left peak is gamma ray of ^{1}H neutron capture and the right peak is ^{208}Tl gamma ray as environment background. The neutron cross section of ^{28}Si is the lowest in Tab. 4.1. Hence, the intensity of ^{28}Si is weak in both figures of ^{28}Si. Additionally the energy distributions of ^{28}Si have a lot of backgrounds contaminated by gamma rays from ^{56}Fe neutron capture whose energy is 6.0 MeV or 7.6 MeV. Two gamma rays of ^{58}Ni with neutron capture emit as Tab. 4.1. Gamma rays from ^{56}Fe and ^{58}Ni neutron capture, 7.631 MeV and 8.994 MeV respectively, contaminate the energy region of ^{58}Ni neutron capture gamma ray of 8.534 MeV. Therefore, the distribution of gamma ray of ^{58}Ni neutron capture with 8.534 MeV becomes broad and This gamma ray cannot be used to estimate energy resolution and linearity.

4.2 Energy Linearity and Resolution

Fig. 4.8 shows energy resolution and linearity. The alpha event of ^{220}Rn and ^{215}Po is added in this figure. The energy of alpha ray is obtained lower than Q value by quenching effect. I will explain the characteristic of alpha ray in next chapter. All plots of energy resolution are fitted by the function as follows.

$$\text{Resolution} = \frac{\text{a}}{\sqrt{\text{Energy}}} \tag{4.3}$$

Where a is free parameter and is obtained to be 1.725 by fitting result. The resolution at Q value is calculated to be 2.6% by above equation.

Next, the energy linearity at Q value is evaluated. Difference of vertical axis in below Fig. 4.8 is defined as follows.

$$\text{Difference} = \frac{\text{Energy from Literature}}{\text{Observed Energy}} \tag{4.4}$$

The difference is larger under 1.5 MeV then other energy region. It is not a serious problem to study of $0\nu\beta\beta$ decay because this region is smaller than energy of Q value. The uncertainty of energy at Q value is under 0.4%. This value is sufficiently smaller than the energy resolution of 2.6%.

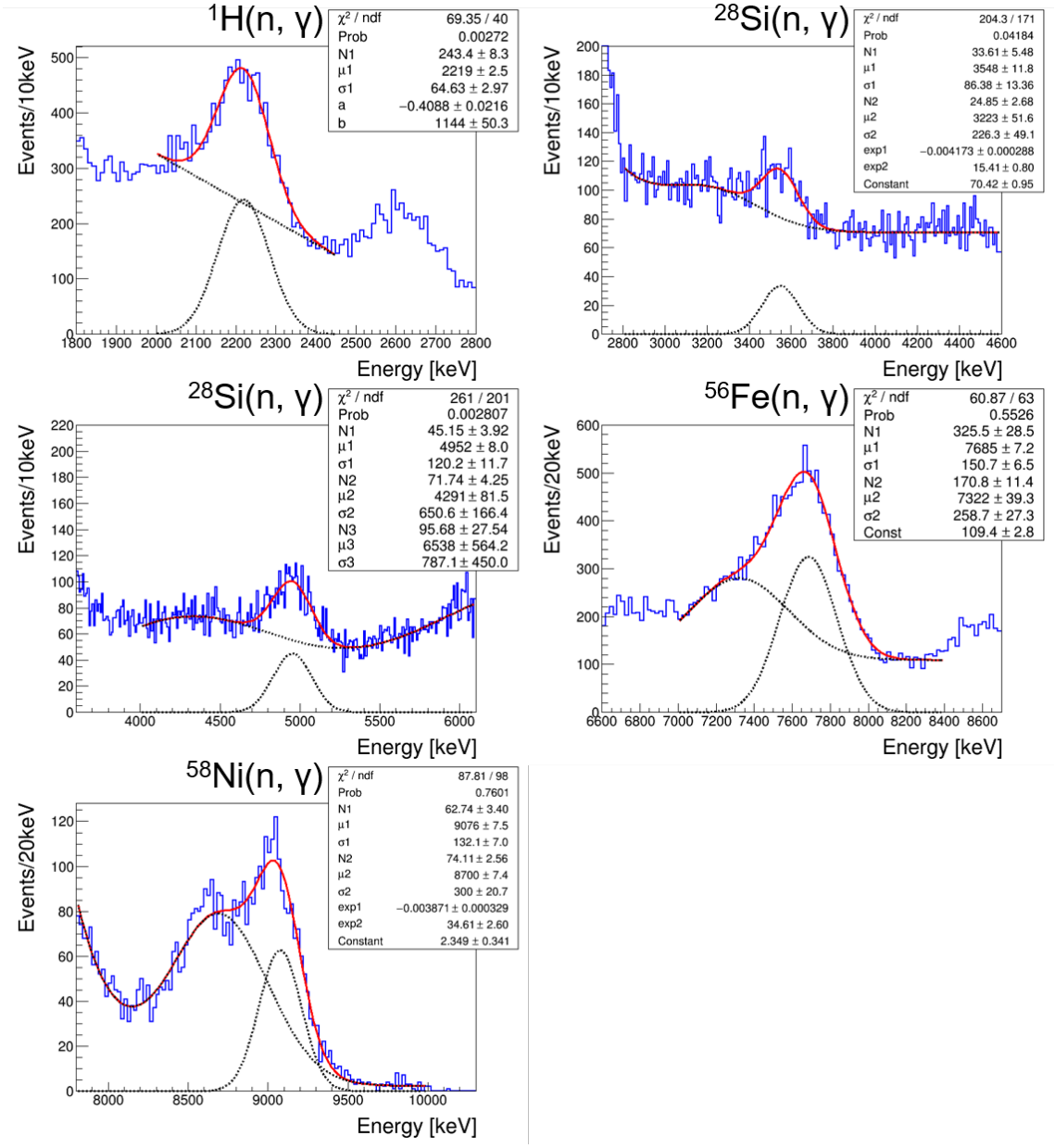

Figure 4.7: Energy distributions of each (n, γ) reactions. Shape of background is assumed by some functions to fit to the peak of (n, γ) reactions.

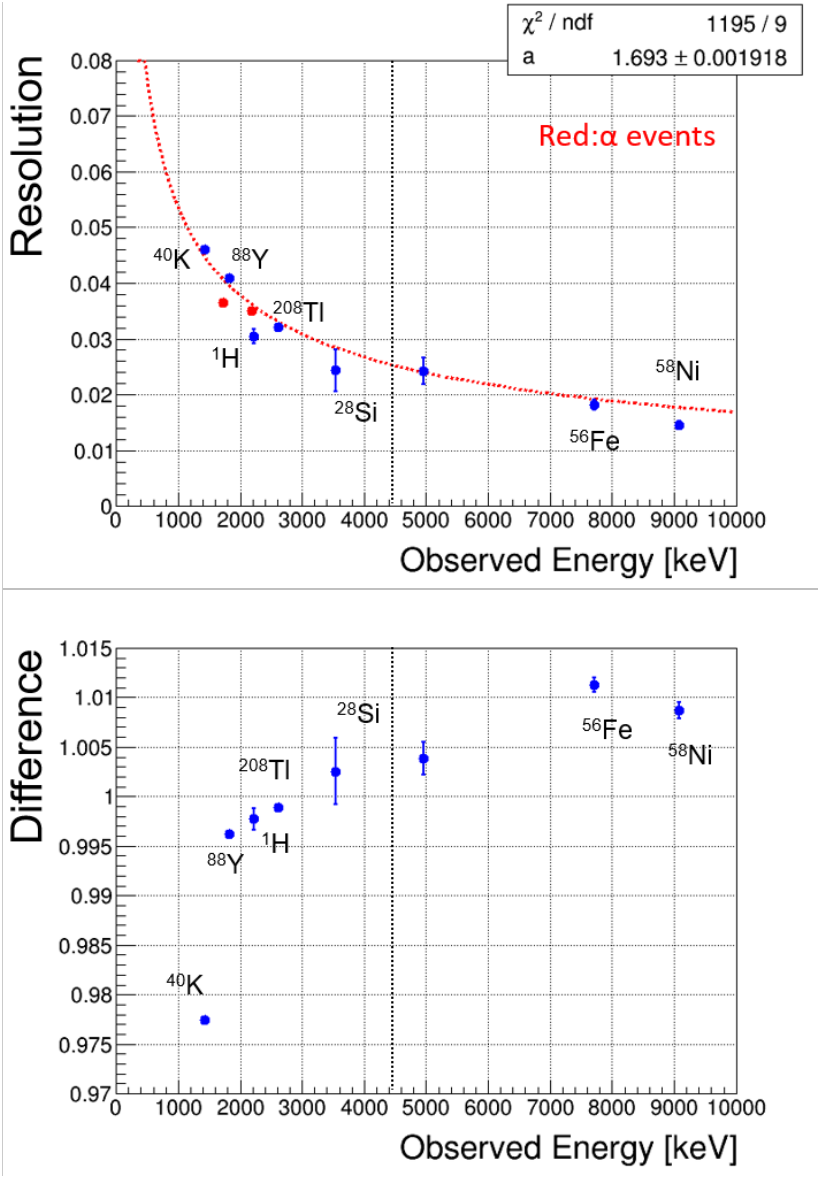

Figure 4.8: Energy resolution and linearity. Energy resolution plots are fitted by Eq. 4.3.

4.3 LS Calibration

As described previous section, the light output between CaF_2 crystal and LS is different. Therefore, the energy of each scintillator has to be calibrated individually. Additionally, the events of gamma ray that deposit energy

under 100 keV into LS is background. Hence, the characteristic of light yield of LS under 100 keV is important. The area ratio of beta and LS waveform can be obtained by PSD as described next section. Then, the area of LS is converted to the energy of LS.

The calibration data for LS is taken by gamma ray of ^{88}Y with the energy of 1.8 MeV. The radiation source of ^{88}Y is installed at the center of the CANDLES Ⅲ detector to observe simultaneously scintillation light of LS with all PMT. Fig. 4.9 shows the Ratio parameter distribution of LS data. Ratio parameter of LS events appears about 1 as described in Sec. 2.3. The position of peak is larger than 1 by influence of overshoot. The right in Fig. 4.9 shows the distribution of NPETotal applied cut condition as 0.8 < Ratio < 1.2. The NPETotal is defined the number of photo electrons in waveform. At this time, the event with saturated PMT is removed. The right peak is expected gamma ray of ^{88}Y in the right figure of Fig. 4.9. The only Gaussian function fit to the peak of ^{88}Y gamma events to obtain the mean value. The light output between CaF_2 crystal and LS is summarized in Tab. 4.3. The ratio of light yield of CaF_2 crystal and LS is calculated to be 0.675 and the energy calibration factor for LS is obtained 671.2 ± 2.3 p.e./MeV.

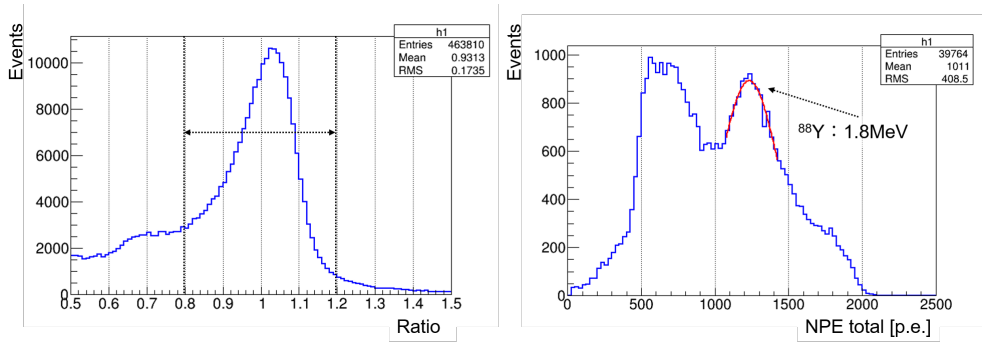

Figure 4.9: The distribution of Ratio and NPETotal of ^{88}Y for LS calibration

Table 4.3: The comparison of characteristic of light yield between CaF_2 and LS at 1.8 MeV

The mean of CaF_2 [p.e.]	The mean of LS [p.e.]	Ratio
1824.3 ± 0.2	1232.4 ± 4.2	0.675 ± 0.002

The characteristic of light yield of LS under 100 keV is evaluated by PSD using 2.8 MeV gamma ray of ^{208}Tl [28]. The reference pulses of beta

and LS fit to each events and the ratio of area of CaF_2 and LS is obtained. The number of p.e. for CaF_2 crystal and LS scintillator is calculated from NPETotal using the ratio of waveform area. After that, the energy of CaF_2 crystal and LS is calculated by Eq. 4.5.

$$\begin{aligned} CaF_2 \text{ Energy} &= CaF_2 \text{ Area} \times F(i) \\ \text{LS Energy} &= \text{LS Area} \times \text{LS Calibration Factor} \end{aligned} \tag{4.5}$$

F(i) is already defined in Eq. 4.1. LS energy is selected with a width of 10 keV from 0 to 800 keV and CaF_2 energy converted from a waveform area distribute in Fig. 4.10. The left figure in Fig. 4.10 shows the distribution of CaF_2 energy selected LS energy of 30 keV. The peak is fit to only Gaussian and the mean value is obtained. True LS energy is calculated by 2.6 MeV of ^{208}Tl minus the fitting result. Then, quenching factor is obtained by dividing the true LS energy by the selected LS energy and the right figure in Fig. 4.10 shows quenching factor. Quenching factor under 150 keV region is not analyzed accurately by fluctuation of waveform. The value under 150 keV is extrapolated by exponential function. The separation ability of PSD is evaluated and the number of background is studied by MC simulation using this relationship.

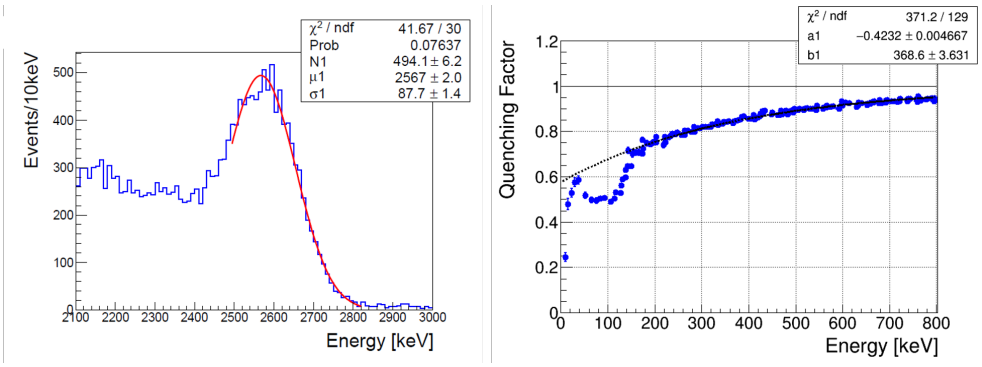

Figure 4.10: The distribution of CaF_2 energy selected LS energy of around 30 keV and quenching factor of LS

Chapter 5

Pulse Shape Discrimination

To search for the $0\nu\beta\beta$ decay, the separation between CaF_2 and CaF_2+LS event and the separation between alpha and beta in CaF_2 crystal are necessary to identify the background events. The pulse shape difference between CaF_2 crystal and LS is described in Sec. 2.3. Fig. 5.1 shows the normalized waveform of alpha and beta events that deposit energy in CaF_2. The clear difference can be seen in the fast component. The reference pulse of alpha, beta and LS are made from background data. All events are fitted by the reference pulse of alpha, beta and beta+LS and the discrimination value is calculated by chi-square method.

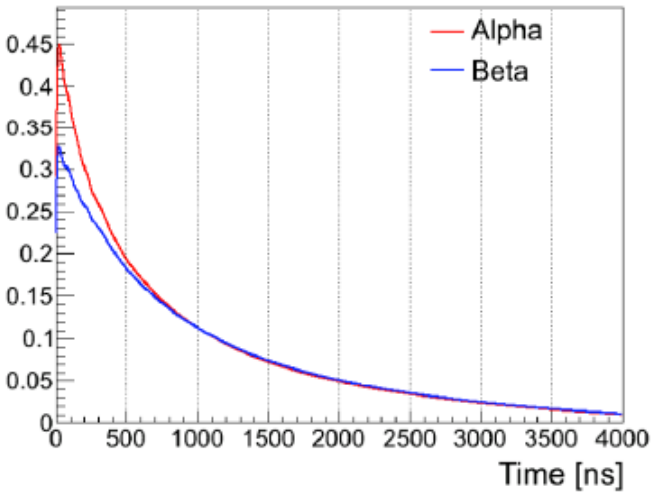

Figure 5.1: The waveform of alpha and beta. The red line shows the average of alpha waveform and the blue line shows the average of beta waveform.

5.1 Reference Pulse

This section explains how to make each reference pulse from data. The reference pulse is made from an average of each sample, such as alpha, beta and LS. Then each event is fitted by the reference pulse and chi-square value is evaluated.

Alpha Reference Pulse

Alpha events from contamination of CaF_2 crystals are used in order to make an alpha reference pulse. The reference pulse of alpha is obtained from ^{215}Po alpha decay. ^{215}Po, in the ^{235}U chain, has a half life of 1.78 ms and undergoes alpha decay. Its parent radioisotope ^{219}Rn also undergoes alpha decay as following equation.

$$^{219}\mathrm{Rn} \xrightarrow[\mathrm{Energy_{visible}=2.0MeV}]{\mathrm{T_{1/2}=3.96sec}} {}^{215}\mathrm{Po} \xrightarrow[\mathrm{Energy_{visible}=2.3MeV}]{\mathrm{T_{1/2}=1.78msec}} {}^{211}\mathrm{Pb} \qquad (5.1)$$

^{219}Rn alpha decay is accompanied by the gamma ray with the branching ratio of 19%. Therefore, alpha events of ^{219}Rn is not used to make the reference pulse. Events occurred in the time window between 500 μsec and 20000 μsec from ^{219}Rn event are selected as the candidate events of ^{215}Po. Distributions of time difference, prompt signal energy and delayed signal energy are shown in Fig. 5.2. On-time is a time gate for selecting signal and from 500 μsec to 10000 μsec. off-time is a time gate for selecting accidental background and from 10500 μsec to 20000 μsec. As Fig. 5.2, accidental rate is low and negligible for making the reference pulse. The ΔT distribution is fitted by exponential function and obtained half-life of 1694 $\pm$ 6 μsec that is near literature value of 1780 μsec .

After making ^{215}Po event list, all alpha waveforms are summed up and the area of waveform in from start channel to 4 μsec is normalized to 1 as Fig. 5.3.

Beta Reference Pulse

^{208}Tl 2.6 MeV gamma rays originate from the outside of the detector are used for making the beta reference pulse. Therefore, gamma rays always pass through LS. When gamma ray deposits energy in LS, Ratio parameter of beta+LS event is larger than beta event. Beta+LS events are removed by Ratio parameter to obtain beta event like $0\nu\beta\beta$ decay. Ratio parameter as explained Sec. 2.3 is used to reduce the influence of LS waveform. Fig. 5.4 shows the energy distribution and the ratio distribution. The light yield

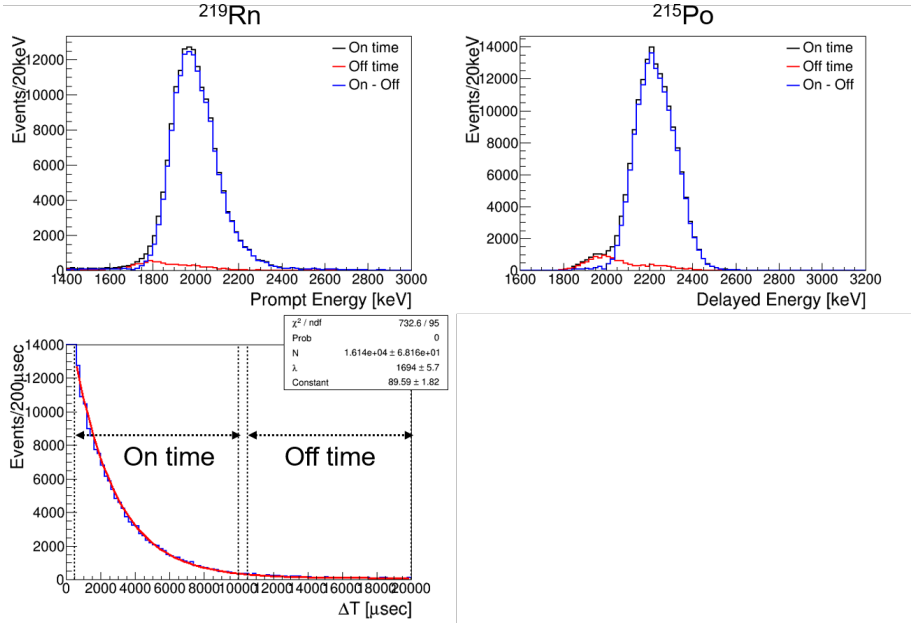

Figure 5.2: Distributions of Energy and ΔT of ^{219}Rn-^{215}Po decay. ^{219}Rn emits alpha ray with gamma ray. Therefore, the energy distribution of ^{219}Rn is not Gaussian and present around 2.3 MeV. The half-life is obtained 1694 $\pm$ 6 μsec by fitting result.

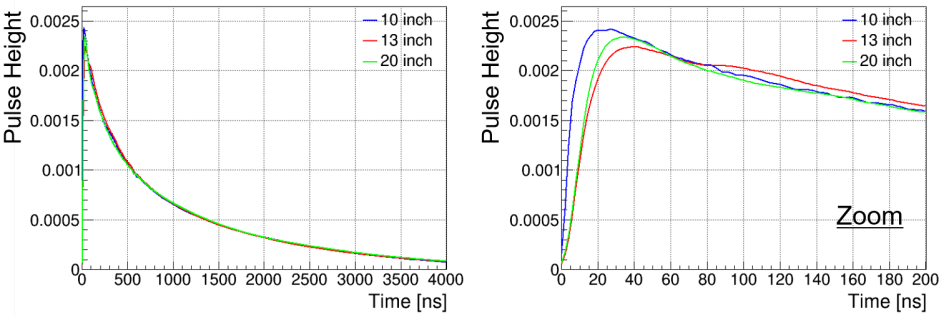

Figure 5.3: The alpha reference pulse of each type PMT. The blue line shows reference pulse of 10 inch PMT. The time resolution is better than other PMT and rising time is quick. The right figure is an enlargement of 0 to 200 ns.

of LS is smaller than that of CaF_2 crystal. Hence, β+LS events distribute region lower than peak of ^{208}Tl energy. In Fig. 5.4 I select energy region

of 2640 to 2770 keV. Moreover, Ratio parameter is used to reduced β+LS events tightly. I select center of Ratio parameter peak as 0.153 to 0.154 in Fig. 5.4.

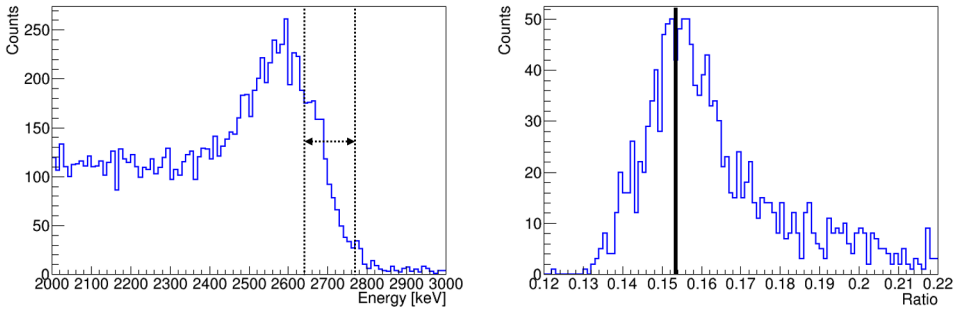

Figure 5.4: The distribution of Energy and Ratio parameter by ^{208}Tl gamma ray. These distributions are used by data of about 1 day.

Fig. 5.5 shows the beta reference pulse of each kind of PMT. The area of beta waveform is normalized same as alpha reference pulse. The statistic of beta event is lower than that of alpha event due to effect of Pb shield. Same of the alpha case shown in Fig. 5.3, the rising time of the beta reference pulse of 10 inch PMT is faster than other PMTs.

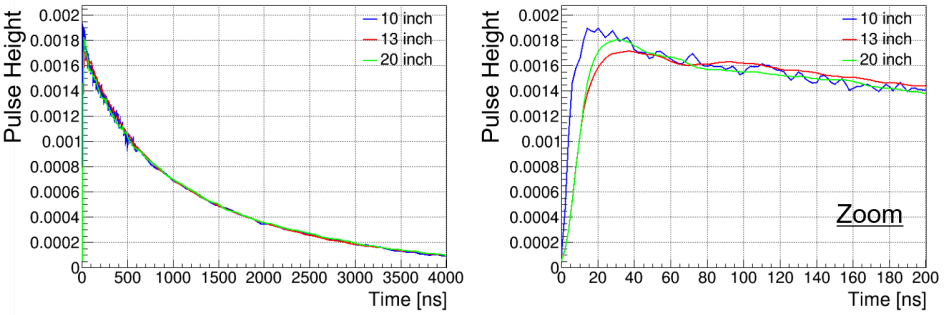

Figure 5.5: The beta reference pulse of each type PMT. The blue line shows reference pulse of 10 inch PMT. The time resolution is better than other PMT and rising time is quick. The right figure is an enlargement of 0 to 200 ns.

We use very tight cut condition for Ratio parameter when the reference pulse of beta event is made from background data. Therefore, we have to

evaluate the bias in the making of the reference pulse. After constructing shield, a data that is installed only CaF_2 crystals in the detector is taken to adjust PMT and electronics response. The waveform from only CaF_2 crystal was taken, since LS was not installed in the detector. Due to adjusting data, live time of data is short, about 70 minutes. The average waveform is made by ^{208}Tl gamma ray selected by same cut condition as beta reference pulse for physics data. Fig. 5.6 shows the comparison of waveform with physics data and only CaF_2 data. The waveform before shield corresponds to physics data and the waveform after shield corresponds to only CaF_2 data. The ratio is defined as the difference between two waveforms. The energy deposit in the LS contributes the discrepancy of the ratio earlier than 50 ns in the Fig. 5.6. The average waveform of physics data is consistent with only CaF_2 data. From above, the beta waveform can be selected the above conditions as Fig. 5.4.

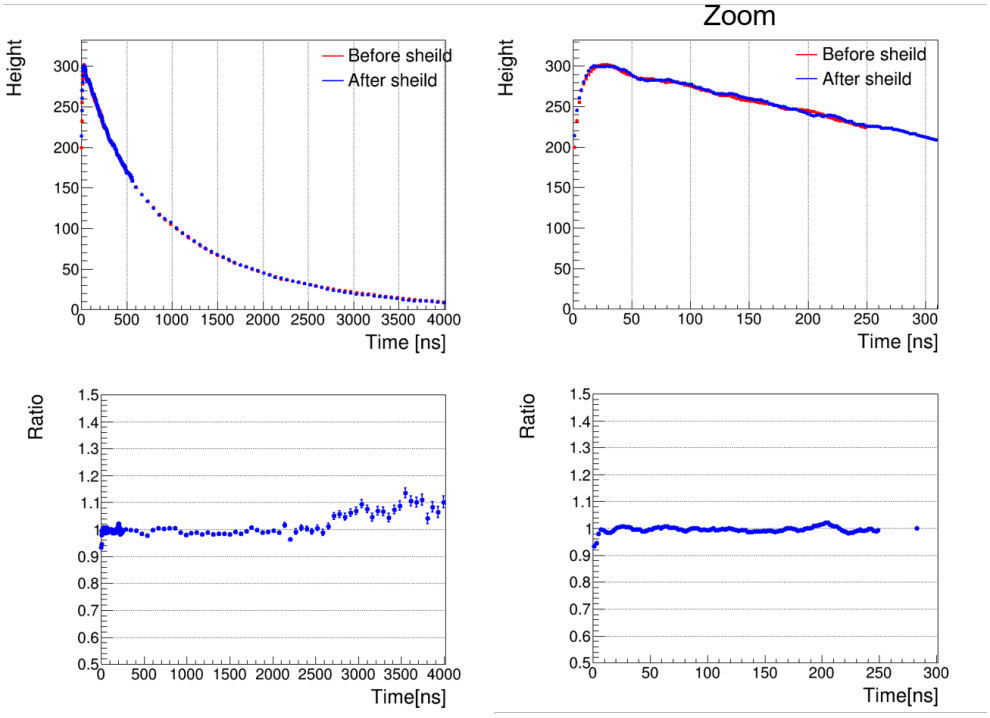

Figure 5.6: The comparison of average waveform with physics data and only CaF_2 data. The right figures is an enlargement of 0 to 300 ns.

LS Reference Pulse

LS events are selected by MBT as explained in Sec. 2.2.2. In order to detect uniformly LS scintillator light in each PMT, events reconstructed within +/- 200 mm from the detector center are selected. Since the dynamic range of FADC is optimized for the waveform of CaF2 crystals, the waveform of LS is often saturated. Therefore, the saturated waveform has to removed when LS reference pulse is made. The energy range is selected above 300 keV to reduce statistical fluctuation of waveform.

Fig. 5.7 shows the LS reference pulse of each PMT. The area of LS waveform in from start channel to 300 nsec is normalized to 1.

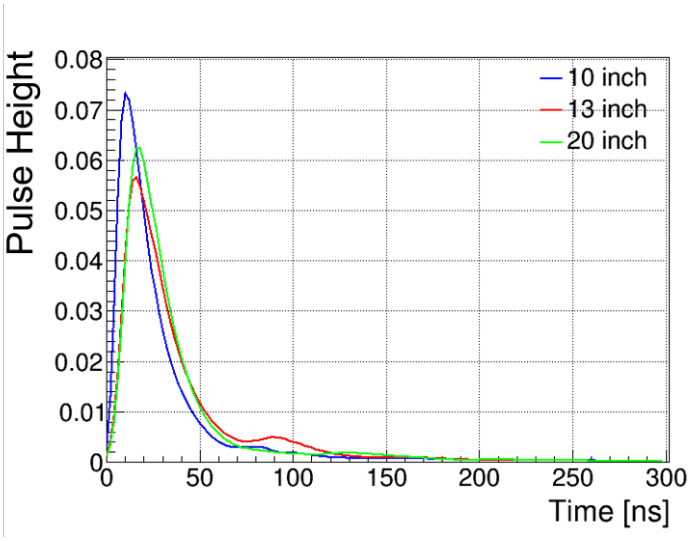

Figure 5.7: The LS reference pulse of each type PMT

5.2 Fluctuation of Pulse and Fitting Method

In general the fluctuation of each bin of waveform is defined by fluctuation of the number of photo electrons as following equation.

$$\text{fluctuation} = \sqrt{\text{NPE}} \tag{5.2}$$

Where NPE means the number of photo electrons. On the other hand, if there is an influence of adjacent bins, it is necessary to evaluate this influence. In the CANDLES experiment, there are two kinds of sampling region such as 2

ns and 64 ns. We have to think how to estimate fluctuation of two sampling regions.

In 2 ns sampling region, the width of bin is narrower than the width of 1 p.e. waveform. Therefore, multiple bins move simultaneously. The width of 1 p.e. waveform is the sigma when the waveform is assumed to be Gaussian. Fig. 5.8 shows the 1 p.e. waveform of each PMT. The width of

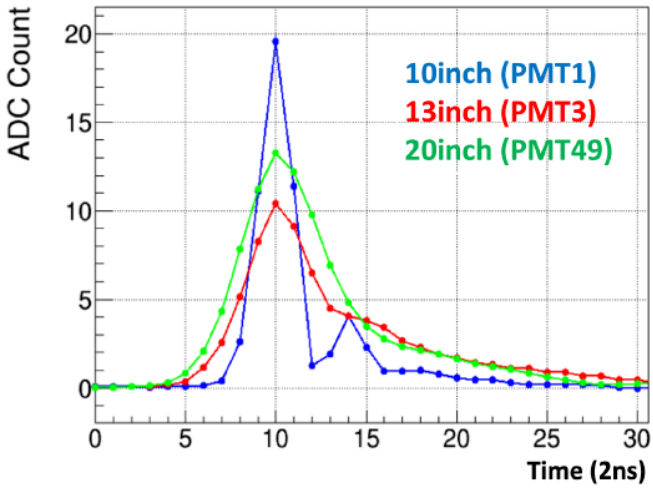

Figure 5.8: The 1 p.e. waveform of each type PMT

1 p.e. waveform is different for each PMT. Among others, the width of 10 inch PMT waveform is quite different. Therefore, the fluctuation of each bin in both 2 ns and 64 ns sampling region is estimated for type of PMT.

In consideration of the above, the fluctuation of each bin in 2 ns sampling region is defined as following Eq.5.3 [29].

$$\text{Fluctuation}^2\,(\text{i}) = \text{Pulse Height}\,(\text{i}) \times \frac{1}{2\sqrt{\pi}} \times \frac{2\,[\text{ns}] \times 1\text{ p.e. charge}\,(\text{i})}{1\text{ p.e. width}\,(\text{i})} \quad (5.3)$$

Where i is the type of PMT such as 10, 13 and 20 inch. 1 p.e. charge is the average of integral value of 1 p.e. waveform and 1 p.e. width is also the average value. 1 p.e. charge and width are summarized in Tab. 5.1.

Next I will explain how to estimate the fluctuation in 64 ns sampling region. The width of each bin such as 64 ns is wider than the width of 1 p.e. waveform. Therefore, we need to consider an influence of adjacent bins. The fluctuation of each bin in 64 ns sampling region is defined as following equation [29].

$$\text{Fluctuation}^2\,(\text{i}) = \text{Pulse Height}\,(\text{i}) \times \frac{1\text{p.e. charge}\,(\text{i})}{32} \quad (5.4)$$

Table 5.1: The 1 p.e. charge and width of each PMT.

Charge [ch]	10 inch	62.3
	13 inch	58.8
	20 inch	59.3
Width [ns]	10 inch	3.2
	13 inch	8.7
	20 inch	7.5

When pulse hight is close to 0, the fluctuation of each bin is calculated by Poison statistics. We set to the criterion for considering Poison statistics as pulse hight is less than 1 p.e. charge and the fluctuation of each bin is defined as following equation.

$$\text{Fluctuation}^2\,(\text{i}) = \left(\frac{\text{1p.e. charge}\,(\text{i})}{32}\right)^2 \tag{5.5}$$

Chi-square value is defined as following equation.

$$\chi^2 = \frac{1}{d}\sum_i \left(\frac{f_i - e_{r,i}}{\sigma_i}\right)^2 \tag{5.6}$$

Where d is the degree of freedom, i is bin number, f_i is the observed pulse height of event, r is the type of reference pulse such as alpha, beta and beta + LS, $e_{r,i}$ is the pulse height of each reference pulse after fitting to event and σ_i is the fluctuation of each bin.

Fig. 5.9 shows the result of fitting. The block points correspond to alpha example waveform. The red line is alpha reference pulse of fitting result and the blue line is beta reference pulse of fitting result. In the left figure of Fig. 5.9, alpha and beta reference pulse fit to alpha event using all bins. Even though the difference between alpha and beta waveform is from 0 to 500 ns, the fitting result in left figure of Fig.5.9 is not used efficiently using this difference. Alpha and beta reference pulse fit to events using 500 to 4000 ns since waveform from 500 to 4000 ns between alpha and beta is same intensity. The right figure in the Fig.5.9 shows the result of fitting range which is set from 500 to 4000 ns. The calculation range of chi-square is used 2 ns sampling region to emphasize difference between alpha and beta waveform. This method is defined as " PSD " parameter because it is not definition of chi-square. " PSD_α " identifies whether an event seems to be alpha event. The case of beta is defined as "PSD_β" and the case of beta+LS is defined as " $\text{PSD}_{\beta+\text{LS}}$ "

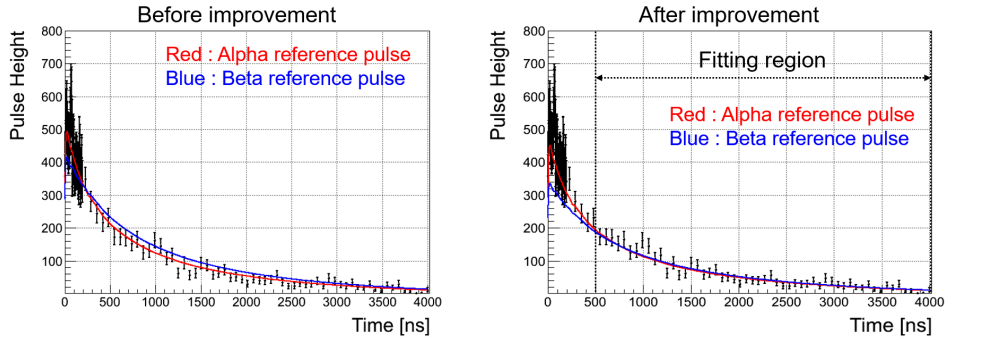

Figure 5.9: The example of reference pulse is fitting to event. The black points correspond to the alpha example waveform. The red line is the alpha reference pulse and the blue line is the beta reference pulse.

5.3 Separation Ability

In this section, the separation ability by PSD_α and PSD_β is evaluated using alpha, beta and beta+LS example events. Alpha example events are used alpha event of ^{215}Po. Beta example events are used gamma ray of ^{208}Tl which deposits energy under 10 keV into LS. These events is selected using LS Energy Parameter described in Sec. 4.3.

α and β Separation

Average sigma is defined as following equation to estimate separation ability of alpha and beta events.

$$\overline{\sigma_{\alpha/\beta}} = \sqrt{\sigma_\alpha^2 + \sigma_\beta^2} \tag{5.7}$$

Fig. 5.10 shows distributions of PSD_β and PSD_α using alpha and beta example events. In left figure of Fig. 5.10, the distance between peaks is divided by $\overline{\sigma_{\alpha/\beta}}$ to be calculated 2.3 ± 0.1. In right figure of Fig.5.10, it is calculated 2.2 ± 0.1 and is obtained almost same result of left figure of Fig. 5.10.

α and β+LS Separation

The separation ability between alpha and beta+LS events using PSD_α is evaluated while LS Energy parameter is changed. Average sigma value is defined as following equation like previous analysis.

$$\overline{\sigma_{\alpha/\beta+\mathrm{LS}}} = \sqrt{\sigma_\alpha^2 + \sigma_{\beta+\mathrm{LS}}^2} \tag{5.8}$$

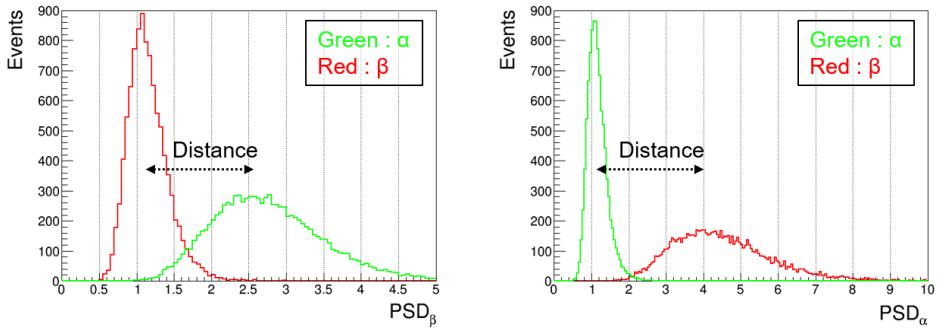

Figure 5.10: The separation ability of alpha and beta events. In the left figure, Horizontal axis is PSD$_\beta$. In the right figure, horizontal axis is PSD$_\alpha$.

The left figure in Fig. 5.11 shows distributions of PSD$_\alpha$ using alpha and beta+LS example events. The right figure in Fig. 5.11 shows separation ability of each LS Energy cut condition. When LS Energy is around 100 keV, it is difficult to separate alpha and beta+LS events.

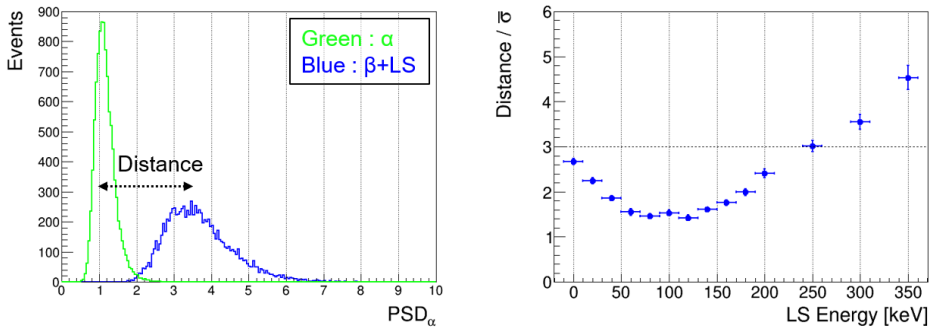

Figure 5.11: The separation ability of alpha and beta+LS. Green line corresponds to alpha events. Blue line corresponds to beta+LS events. In left figure, gamma ray of ^{208}Tl deposits energy of about 250 keV.

β and β+LS Separation

The separation ability between beta and beta+LS events using PSD$_\beta$ is evaluated. Average sigma value is defined as following equation.

$$\overline{\sigma_{\beta/\beta+\mathrm{LS}}} = \sqrt{\sigma_\beta^2 + \sigma_{\beta+\mathrm{LS}}^2} \tag{5.9}$$

The left figure in Fig. 5.12 shows distributions of PSD_β using beta and beta+LS example events. The right figure in Fig. 5.12 shows separation ability of each LS Energy cut condition. When LS Energy is over 140 keV, beta and beta+LS can be separated efficiently over 3σ. The detection of beta events like $0\nu\beta\beta$ decay is estimated in Chap. 7.

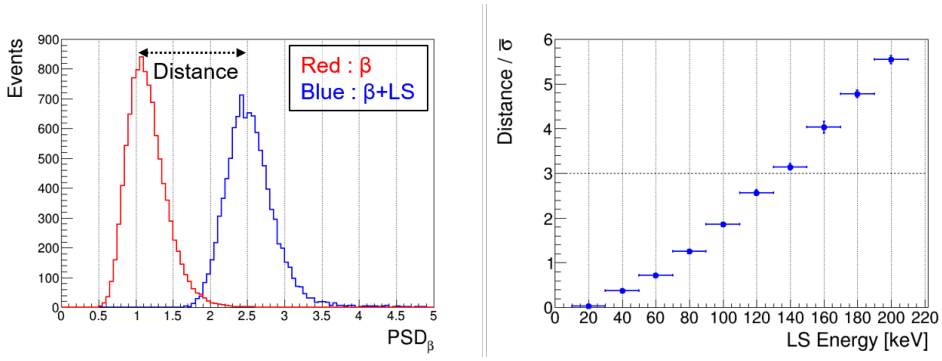

Figure 5.12: The separation ability of beta and beta+LS.

Chapter 6

Detector Performance

The time stability of some parameter is studied to evaluate the detector performance. The radioactive contamination within CaF_2 crystals is evaluated to estimate the number of backgrounds in ^{232}Th chain. The observed energy of alpha event in CaF_2 crystal is lower than the literature energy by quenching effect. Quenching factor of CaF_2 crystal for alpha event is study to predict energy region distributed alpha event.

6.1 Stability of crystal and time dependence

6.1.1 Crystal Dependence

The stability of energy about each crystal is studied by gamma ray of ^{208}Tl (2.6 MeV). The energy distribution of each crystal is fitted by Gaussian function to obtain the mean value.

The left figure in Fig. 6.1 shows the crystal dependence of the mean value of ^{208}Tl. The difference between top layer and bottom layer is about 60 keV. This value is same as energy resolution of about 3% at 2.6 MeV. ^{88}Y emits simultaneously two gamma ray in Fig. 4.1. Beta + LS events of accidental background are contaminated around 1.8 MeV region. Therefore, the situation between physics data and calibration data is different. The crystal dependence is corrected for each layer. The right figure in Fig. 6.1 shows the crystal dependence of the mean value of energy after layer correction. The mean of Cr 57 is the most difference in all crystals since the CaF_2 module of Cr 57 is contaminated air. $0\nu\beta\beta$ decay is analyzed except Cr 57. The average mean value is 2619.12 $\pm$ 0.32 keV. The root mean square (RMS) of mean value in all crystals is calculated to be 8.08 $\pm$ 0.58 keV for fluctuation estimation. The fluctuation of mean value in all crystals is 0.3% that is less

than 1% and it is negligible.

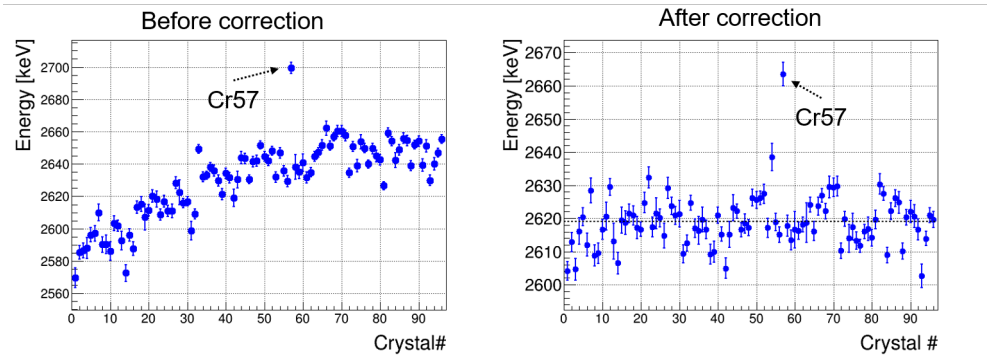

Figure 6.1: The crystal dependence of the mean value of ^{208}Tl. Horizontal dotted black line is the average mean value.

Fig. 6.2 shows the crystal dependence of the sigma value. The average sigma value is 77.01 ± 0.25 keV and the RMS of sigma value is 4.72 ± 0.34 keV. Energy resolution is estimated using events of all crystals including the fluctuation of sigma value.

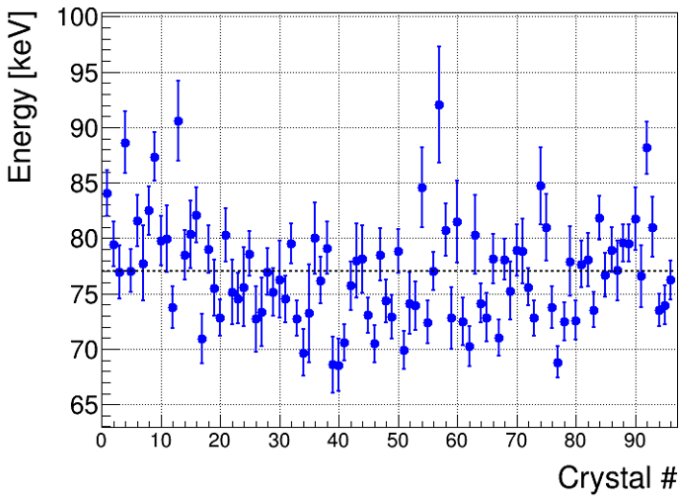

Figure 6.2: The crystal dependence of the sigma value of ^{208}Tl. Horizontal dotted black line is the average mean value.

The mean value of crystal dependence is also analyzed using gamma ray of ^{56}Fe (n, γ) reactions. Fig. 6.3 shows the crystal dependence of the mean

value of ^{56}Fe. Neutron source of ^{252}Cf is set to top of the detector and gamma ray of ^{56}Fe (n, γ) reactions is emitted from top of the detector. Therefore, the statistics of ^{56}Fe events in 5th and 6th layer is lower than other layer and the mean value of crystal dependence cannot be obtained. After layer correction, the layer dependence is nothing.

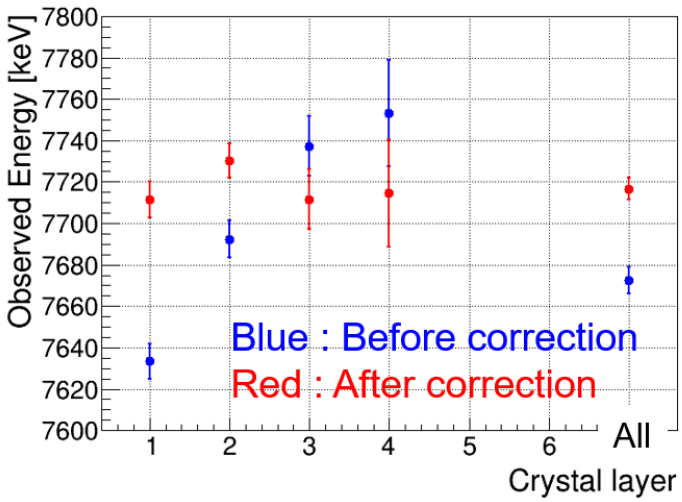

Figure 6.3: The crystal dependence of the mean value of ^{56}Fe. Blue plots corresponds to before layer correction and red plots corresponds to after layer correction.

6.1.2 Time Dependence

After layer correction, the time dependence of mean and resolution value of energy is studied by gamma ray of ^{208}Tl (2.6 MeV). The time dependence of mean and sigma of position is also studied by gamma ray of ^{40}K (1.46 MeV).

Fig. 6.4 shows the time dependence of the mean and resolution value of energy. The average mean value of energy is calculated to be 2615.74 $\pm$ 0.37 keV and the RMS of mean value of energy is calculated to be 5.19 $\pm$ 0.32 keV. This fluctuation is 0.2% that is less than energy resolution of 3%. The average resolution value is calculated to be 0.0306 $\pm$ 0.0001 and the RMS value of energy resolution is calculated 0.0013 $\pm$ 0.0001. From above result, the uncertainty of energy resolution is estimated. The energy resolution at Q value region is calculated to be 2.64% by Fig. 4.8. The fluctuation of energy resolution is calculated to be 0.11% at Q value region.

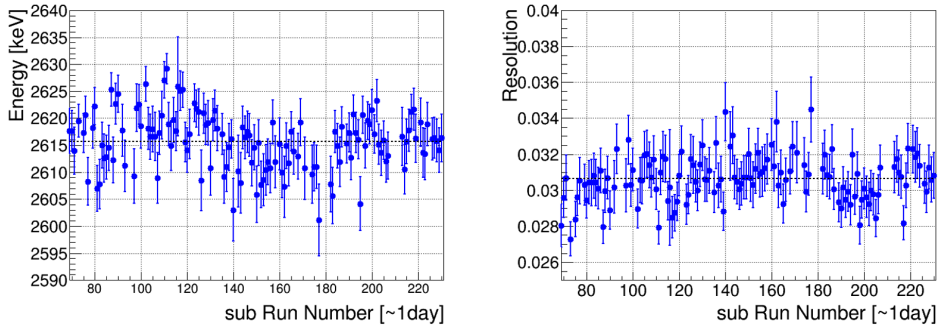

Figure 6.4: The time dependence of the mean and resolution of ^{208}Tl. Horizontal dotted black line is the average value.

Fig. 6.5 shows the time dependence of the mean and sigma value of position for each axis. The reference position of each axis is calculated crystal by crystal and the difference between reconstructed position of each event and the reference position is distributed around 0. This distribution is fitted by Gaussian function and the mean and sigma value of each axis are obtained. The average and RMS of mean and sigma value are summarized in Tab. 6.1. The average mean value of each axis is almost 0 mm and stable. The sigma value of each axis is gradually increasing. However, it is not serious problem, since the RMS of both mean and sigma is lower than 1 mm.

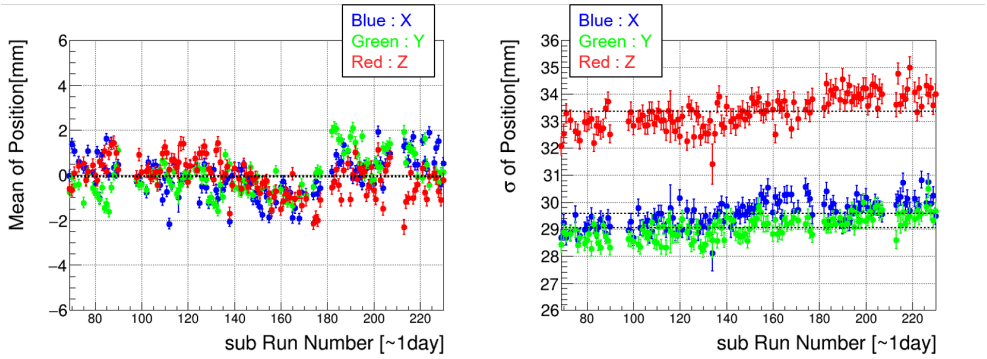

Figure 6.5: The time dependence of the mean and sigma of position for each axis. Horizontal dotted black line is the average value.

Table 6.1: The Average mean and sigma value of position and the RMS of mean and sigma value of position.

	Axis	Average [mm]	RMS [mm]
Mean	X	-0.03 ± 0.02	0.87 ± 0.05
	Y	-0.02 ± 0.02	0.87 ± 0.05
	Z	-0.07 ± 0.02	0.81 ± 0.05
Sigma	X	29.48 ± 0.03	0.50 ± 0.03
	Y	29.05 ± 0.03	0.42 ± 0.03
	Z	33.36 ± 0.03	0.61 ± 0.04

6.1.3 Livetime

Live time is calculated to be 129.5 days for physics data and the efficiency of Live time is evaluated. Fig. 6.6 shows the efficiency of Live time. Run time means the real time from start to stop of DAQ. Live time is except dead time which cannot be accepted data to save data to PC. The average value is calculated 99.9986%. $0\nu\beta\beta$ decay can be measured without dead time.

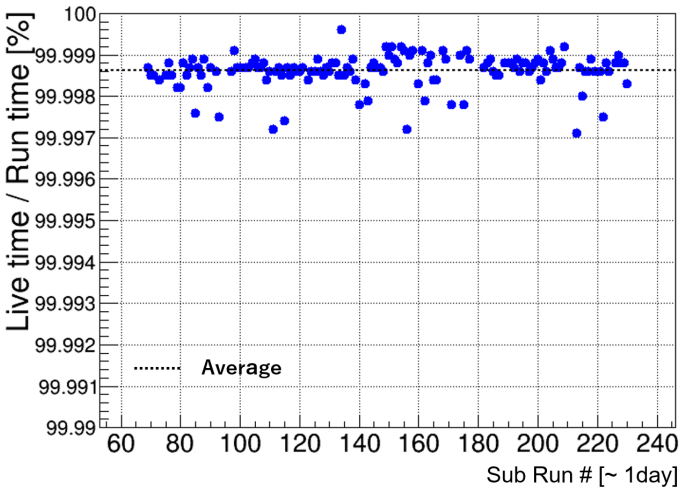

Figure 6.6: The efficiency of Run time and Live time.

6.2 Radioactive Contamination in CaF_2 Crystals

The radioactive contamination level within Cr11 is the highest in the CANDLES III detector. The study of background and $0\nu\beta\beta$ decay is analyzed without Cr11.

^{232}Th

The radioactive contamination of ^{232}Th within crystals is estimated using delayed coincidence analysis of ^{220}Rn-^{216}Po (Eq. 6.1).

$$^{220}\mathrm{Rn} \xrightarrow[\mathrm{Q}_\alpha=6.405\mathrm{MeV}]{\mathrm{T}_{1/2}=55.6\mathrm{sec}} {}^{216}\mathrm{Po} \xrightarrow[\mathrm{Q}_\alpha=6.907\mathrm{MeV}]{\mathrm{T}_{1/2}=0.145\mathrm{sec}} {}^{212}\mathrm{Pb} \tag{6.1}$$

Both ^{220}Rn and ^{216}Po events deposit energy into same CaF_2 crystal due to alpha ray. Accidental background rate is low since half-life of 145 μsec is short. Therefore, it is easy to analyze delayed coincidence of ^{220}Rn-^{216}Po. Fig. 6.7 shows the distribution of energy and dT of ^{220}Rn-^{216}Po. ^{220}Rn - ^{216}Po events are collected during On-time which is set from 60 to 400 msec. off-time is set from 1000 to 1340 msec for estimation of accidental background The radioactive contamination of ^{232}Th for each crystal is calculated by the number of events of ^{220}Rn which is estimated by the distribution of on-time minus off-time. The detection efficiency of on-time is calculated to be 60.3% by half-life. Fig. 6.8 shows the radioactivity contamination of ^{232}Th for each crystal. The average radioactive contamination is 18.7 μBq/kg. CaF_2 crystals of radioactive contamination of the central layer are lower than CaF_2 crystals of top and bottom layer. Radioactive contamination of ^{232}Th under 10 μBq/kg is defined as low radioactive crystal.

6.2.1 Quenching Factor

Basically, quenching factor has energy dependence and each CaF_2 crystal has unique quenching factor.

Fig. 6.9 shows energy peak of each CaF_2 crystal using alpha events of ^{215}Po. The energy peak of Cr54 is difference from other crystals, since quenching factor of Cr54 is lager than that of other crystals. It is difficult to estimate the number of background events and the efficiency of some cut conditions. Therefore, $0\nu\beta\beta$ decay and background study are analyzed except Cr54.

In the CANDLES III detector, some kinds of alpha event can be observed and energy dependence of quenching factor can be studied. Fig. 6.10 shows

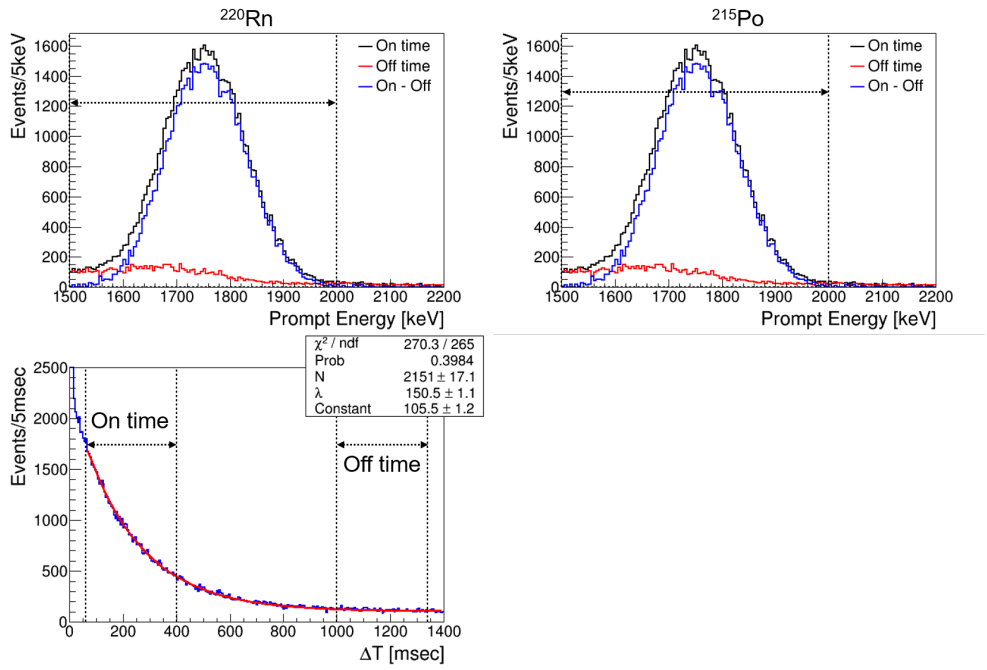

Figure 6.7: Distributions of Energy and ΔT of ^{220}Rn-^{216}Po. The dotted arrow is the selection region.

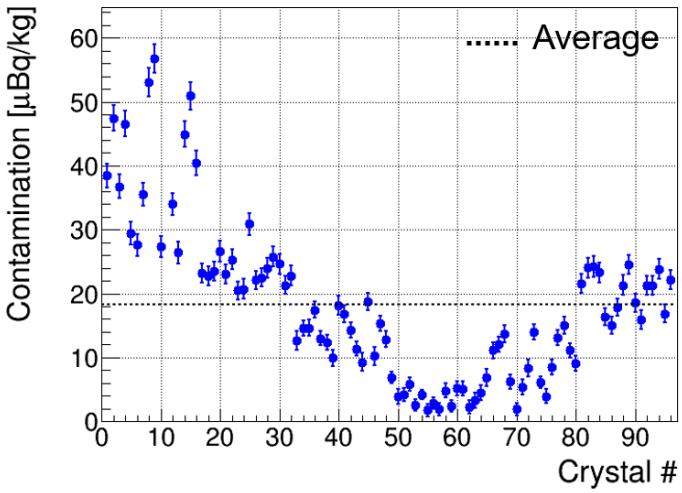

Figure 6.8: The radioactive contamination of ^{232}Th for each crystal

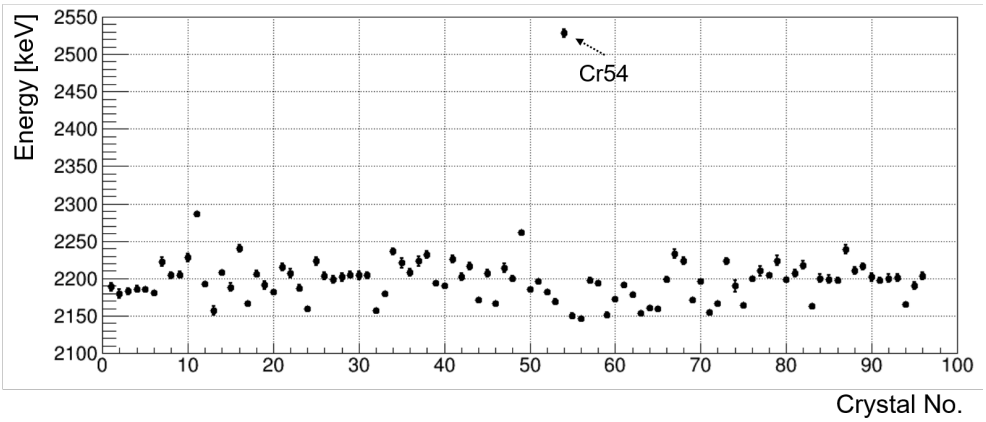

Figure 6.9: Energy peak of ^{215} Po of each CaF_2 crystal

quenching factor of alpha event with CaF_2 crystal. Quenching factor of energy dependence is described by the Birks low which is a rule of thumb. The Birks low is

$$\frac{dL}{dx} = \frac{S\frac{dE}{dx}}{1 + k\beta\frac{dE}{dx}} \tag{6.2}$$

where dL is light yield, dE/dx is intensity of energy deposit and S and kβ is constant [30]. The quenching factor of ^{212}Po alpha event which has Q value of 8.954 MeV is estimated to be 0.326 by Fig. 6.10. The visible energy of ^{212}Po alpha event is calculated to be 2.920 MeV.

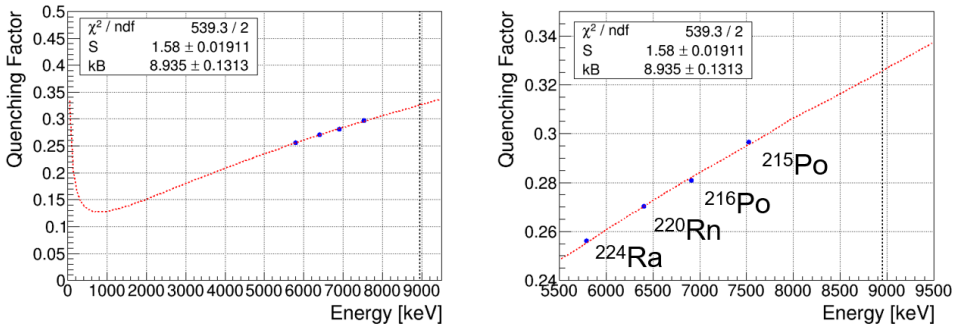

Figure 6.10: The quenching factor of alpha ray with CaF_2. The dotted red line corresponded to the Birks low.

Chapter 7

Background Estimation and Signal Efficiency

7.1 Characteristic of Backgrounds

In this section, the characteristic of backgrounds at Q value is described and the analysis methods for rejecting backgrounds are explained.

7.1.1 ^{212}Bi-Po Sequential Decay

^{212}Bi-^{212}Po sequential decay, which belongs to ^{232}Th series decay chain, take place in the CaF_2 crystal. It has 0.3 μsec half life, which is shorter than the 1 μsec decay time constant of CaF_2 crystal. ^{212}Bi beta and ^{212}Po alpha events are recorded as one event that has 8.6 μsec time window. ^{212}Po alpha event (8.95 MeV) observed as 2.92 MeV event by the quenching effect. The visible energy of ^{212}Bi-Po sequential decay is expected up to about 5 MeV.

$$^{212}\mathrm{Bi} \xrightarrow[\mathrm{Q}_\beta=2.254\mathrm{MeV},\ 64.06\%]{\mathrm{T}_{1/2}=60.55\mathrm{min}} {}^{212}\mathrm{Po} \xrightarrow[\mathrm{Q}_\alpha=8.954\mathrm{MeV}]{\mathrm{T}_{1/2}=0.299\mu\mathrm{sec}} {}^{208}\mathrm{Pb} \tag{7.1}$$

Two methods are used to remove the background of ^{212}Bi-Po decay at Q value. The time difference is obtained by double pulse shape discrimination. The backgrounds of ^{212}Bi-Po can be rejected when time difference is over 20 ns. The event that has too short time difference under 20 ns to be separated into ^{212}Bi beta and ^{212}Po alpha has alpha like waveform. Therefore, these events can be removed by PSD_β that is for selecting beta events. I will discuss the concrete cut condition and detection efficiency of $0\nu\beta\beta$ decay in Sec. 7.3.3.

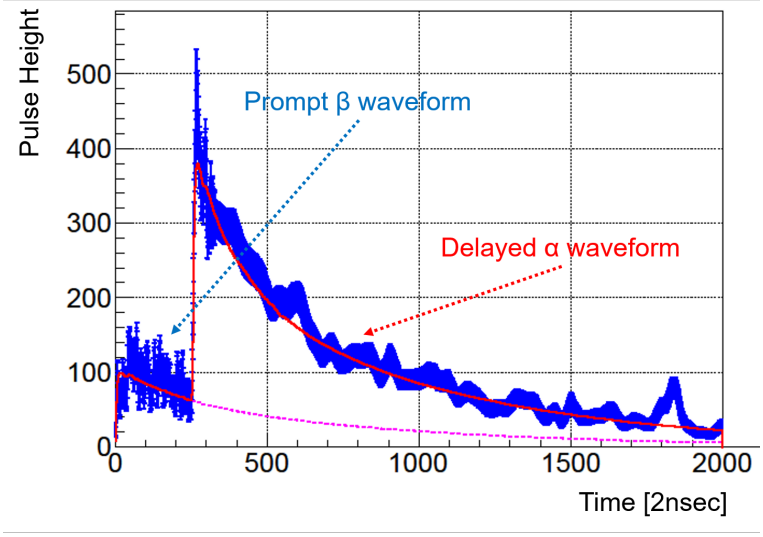

Figure 7.1: The pulse shape of ^{212}Bi-Po sequential decay.

7.1.2 ^{208}Tl Beta Decay

Q value of ^{208}Tl beta decay is 5.0 MeV and half-life is 3.1 minutes as following Eq. 7.2. ^{212}Bi with the Q value of 6.2 MeV, which is parent of ^{208}Tl, undergoes the alpha decay with the visible energy of 1.7 MeV. In ^{208}Tl beta decay, event which deposit energy in CaF_2 by both beta and gamma ray becomes background at Q value region. Survival probability of this event is very low. However, it is important for rare decay search like $0\nu\beta\beta$ decay to evaluate the number of ^{208}Tl events at Q value region. Since this beta+gamma event is identical to beta event, we cannot remove such event by PSD method.

$$^{212}\mathrm{Bi} \xrightarrow[\mathrm{Q}_\alpha=6.207\mathrm{MeV},\ 35.94\%]{\mathrm{T}_{1/2}=60.55\mathrm{min}} {}^{208}\mathrm{Tl} \xrightarrow[\mathrm{Q}_\beta=5.001\mathrm{MeV}]{\mathrm{T}_{1/2}=3.053\mathrm{min}} {}^{208}\mathrm{Pb} \tag{7.2}$$

The delayed coincidence method between ^{212}Bi and ^{208}Tl is used to identify ^{208}Tl event. ^{212}Bi alpha ray are identified by PSD_α. Then, all events within 18 min after observed ^{212}Bi alpha ray in same crystal are vetoed. I will discuss detail in Sec. 7.3.4.

Currently, when the reconstructed positions of parent and daughter are same, most of the events of ^{208}Tl can be selected and vetoed. In the CANDLES Ⅲ detector, the ^{208}Tl multi-hit event is the characteristic background events. Fig. 7.3 shows the schematic view of ^{208}Tl multi-hit event. As described above, ^{208}Tl emits beta ray and gamma ray with the energy of 2.6 MeV. In the multi-hit events, beta ray deposits energy into same CaF_2 crys-

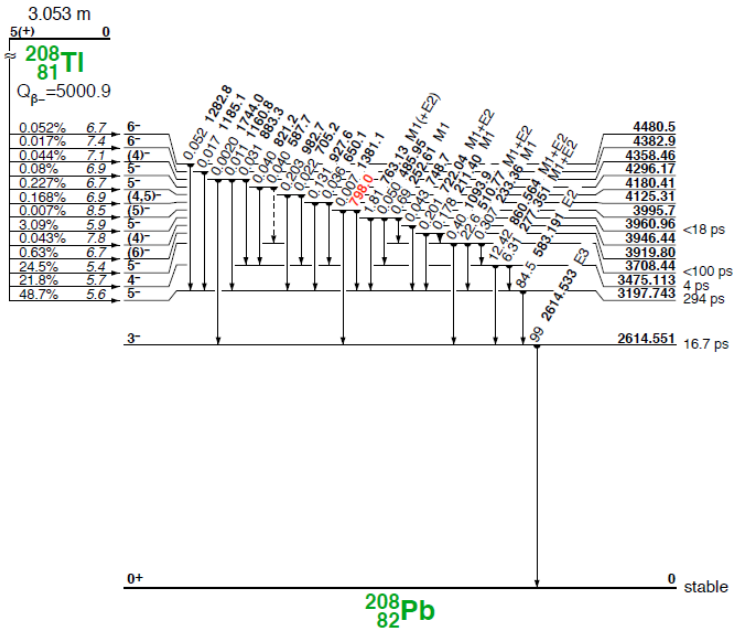

Figure 7.2: Decay scheme of ^{208}Tl.

tal where alpha ray of ^{212}Bi deposits energy. However, gamma ray of ^{208}Tl has high transmittance. Therefore, gamma ray with the energy of 2.6 MeV may deposit energy in the neighbour crystal. In this case, the position of delayed events could be reconstructed in the neighbour crystal. If the reconstructed crystal positions of the parent and daughter nucleus are different, it is difficult to identify by delayed coincidence method.

7.1.3 Gamma ray of Neutron Capture Reactions

As already explained in Sec. 2.1.3, the data taking in 2014 has unexpected background events in the region of interest at 4.3 MeV. We understood with neutron calibration and MC simulation that background is gamma ray of (n, γ) reactions in stainless steel tank and surrounding rock. The background of (n, γ) reactions was dominant and was expected to be 66 $\pm$ 12 events/year in all 96 crystals [31]. We designed gamma and neutron shield by Pb and B sheet with MC simulation in order to reduce the background level as 0.5 event/year in all 96 crystals. After construction of shield, the physics data is taken and analyzed by cut condition of Ratio parameter [32]. Fig. 7.4 shows comparison of energy spectrum before and after shield installation. Every energy spectrum is scaled by live time to compare the number of (n, γ) events

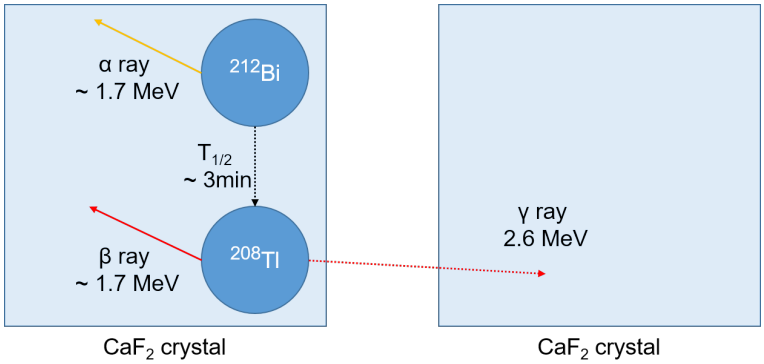

Figure 7.3: The schematic view of ^{208}Tl multi-hit event.

between 5.5 MeV and 10 MeV. The events from 5 to 10 MeV is reduced obviously from the previous data. The background reduction between 5.5 MeV and 10 MeV was analyzed to be 1/35.5 by real data. However, the reduction estimated by MC simulation is expected better than the reduction from physics data. This result is consistent with MC simulation in statistical 2 σ error region. It it difficult to analyze above 5 MeV due to small statistic. Detail study for (n, γ) background should be done with higher statistics in the future. However, (n, γ) background is now negligible after shield installation.

7.1.4 $2\nu\beta\beta$

$2\nu\beta\beta$ and $0\nu\beta\beta$ decay have the same Q value such as 4.28 MeV and neutrinos from $2\nu\beta\beta$ decay cannot be detected by detector in experiments of $0\nu\beta\beta$ decay search. Therefore, events of $2\nu\beta\beta$ decay can not be removed. In the CANDLES experiment, the energy resolution has to be improved to separate $2\nu\beta\beta$ decay. In the current sensitivity of CANDLES III, $2\nu\beta\beta$ decay is not serious background since the number of ^{48}Ca is very small. The number of $2\nu\beta\beta$ events is expected under 0.1 events / year around Q value energy region when the half-life of $2\nu\beta\beta$ decay is assumed the result of NEMO-3 experiment. The result of obtained half-life of $2\nu\beta\beta$ decay is summarized in Tab. 7.1.

After developing enrichment technique for ^{48}Ca, $2\nu\beta\beta$ decay will become a serious background.

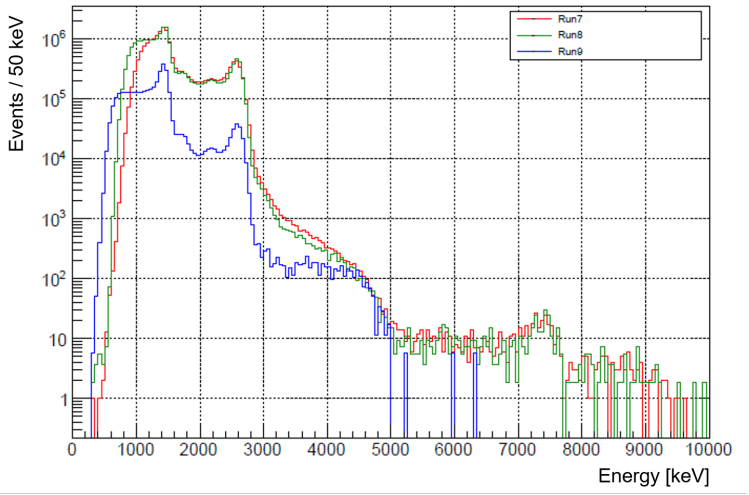

Figure 7.4: Total energy spectrum before and after installed shield. Red and Green line shows before installed shield and the spectra for Red and Green agree well due to similar experiment set up. The (n, γ) events in Blue histogram are reduced above 5 MeV region by shield.

Table 7.1: The result of obtained half-life of $2\nu\beta\beta$.

Experiment	$T^{2\nu}_{1/2} \times 10^{19}$ [year]	Reference
Time Projection Chamber	$4.3^{+2.4}_{-1.1} \pm 1.4$	[36]
TGV	$4.2^{+3.3}_{-1.3}$	[37]
ELEGANTVI	$1.4^{+0.3}_{-0.2} \pm 0.5$	[20]
NEMO-3	$6.4^{+0.7+1.2}_{-0.6-0.9}$	[38]

7.2 Monte Carlo Simulation for Background study

In this section, the energy spectrum and the number of events of backgrounds between physics data and MC simulation are compared to estimate quality of MC simulation response. Cut conditions for selection of ^{212}Bi-Po sequential decay and ^{208}Tl beta decay are determined by physics data. The detection efficiency of each cut condition is estimated by MC simulation. The number of expected events is obtained by detection efficiency of each cut condition and impurity value of ^{232}Th from Sec. 6.2 and is compared with the number of observed events.

The number of expected backgrounds is simulated with the MC simulation based on the Geant4 version 4.10.02.p02 [33], [34], [35]. In the MC simulation, beta decay of ^{208}Tl and beta decay of ^{212}Bi are decayed in the CaF_2 crystals. In the physics data analysis, the position of each event is reconstructed by weighted mean of observed p.e.. On the other hand, in the MC simulation weighted mean of energy deposit position is used for position reconstruction. Therefore, the light output between CaF_2 crystal and LS is important information to understand the MC response. The conversion factor for LS is obtained in Sec. 4.3. Resolutions of energy and position is used by observation from data (Fig. 3.12, Fig.4.8).

^{212}Bi-Po sequantial decay

As Fig. 7.1 shows, candidate events of ^{212}Bi-Po sequential decay are fitted by the beta and alpha reference pulse. The ratio of waveform area of beta and alpha can be obtained by fitting result. Total area is integrated waveform from 0 to 4 μsec and is distributed by the ratio of waveform area of beta and alpha. Energy calibration factor has crystal dependence as explained in Chap. 4. However, both beta ray and alpha ray of ^{212}Bi-Po sequential decay deposit in same CaF_2 crystal. Therefore, the ratio of waveform area corresponds to the ratio of energy. From fitting result, the time difference between beta and alpha waveform.

Fig. 7.5 shows the distribution of prompt energy, delayed energy, delta T, chi-square value. The sum energy (beta+alpha) from 3.0 MeV to 5.5 MeV is selected, when Fig. 7.5 is drawn, because the backgrounds in this energy region are dominated by CaF_2 crystal internal radioactive contamination including ^{212}Bi-Po. The peak around 200 keV is due to failure of fitting in Fig. 7.5(a). I guess that this reason is external background such as gamma ray of ^{208}Tl. These misidentified events are removed from selecting the ^{212}Bi-Po events. Therefore, I select the events whose energy is from 400 keV to 3500 keV. Fig. 7.5(b) shows the distribution of delayed energy and alpha ray of ^{212}Po is distributed to around 3 MeV by the questing effect. Fig. 7.5(c) shows the distribution of time difference from beta and alpha waveform. The half-life of ^{212}Bi-Po is obtained 287.3 $\pm$ 4.0 μsec by fitting result. This result is almost same of the literature value of 299 μsec. The time difference shorter than 20 ns is misidentified by accidental background or ^{212}Bi-Po events with a half-life of about 20 ns or less. Therefore, the events with time difference of above 20 ns are selected as ^{212}Bi-Po events. Fig. 7.5(d) shows the distribution of chi-square. The event whose time difference is shorter than 20 ns is excluded when this figure is drawn.

From the above result, the cut condition for ^{212}Bi-Po selection is summa-

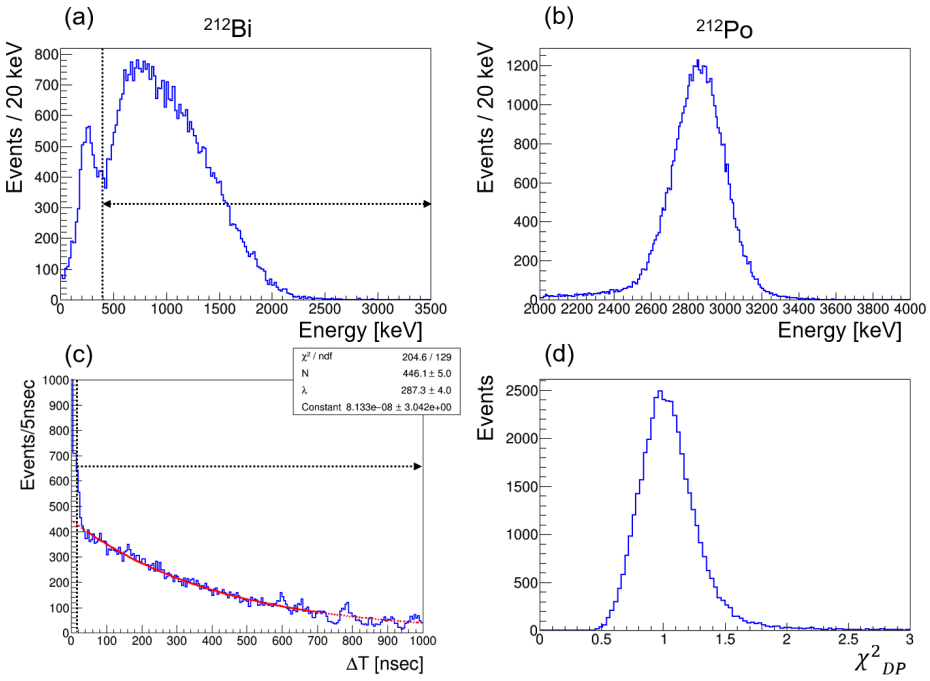

Figure 7.5: The distribution of fitting result of ^{212}Bi-Po. (a) The distribution of prompt energy. The peak around 200 keV is due to failure of fitting. (b) The distribution of delayed energy. Alpha events of ^{212}Po is distributed to around 3 MeV by the questing effect. (c) The distribution of difference from beta and alpha waveform. The half-life of ^{212}Bi-Po is obtained 188.5 ± 6.3 by fitting result. This result is different from the literature value. (d) The distribution of chi-square. The event that the fitting is failed is excluded when this figure is drawn.

rized as follows.

$$400 < \text{Prompt Energy} < 3500 \text{ [keV]}$$
$$2000 < \text{Delayed Energy} < 4000 \text{ [keV]}$$
$$20 < \Delta\text{T} < 3800 \text{ [nsec]}$$
$$\chi^2_{\text{DP}} < 3$$

The cut conditions described above are applied for both data and MC. Fig. 7.6 shows the comparison of energy distribution of data and MC simulation. The energy distribution of physics data above 3.7 MeV region is consist with MC simulation but this distribution from 3.0 to 3.5 MeV is not consistent. One of reason is that the energy of prompt beta ray is lower than the threshold of DGT and only delayed alpha ray is observed. Therefore, I guess only

alpha ray is removed by double pulse analysis. The detection efficiency of prompt energy for ^{212}Bi-Po is calculated using the result that the energy distribution above 4 MeV is consistent between physics data and MC simulation. After that, the number of calculated events of ^{212}Bi-Po is compared with the number of observed events and the uncertainty of our estimation by MC simulation. The number of observed events above 4 MeV is 11200 events in physics data. The detection efficiency of each parameter is summarized in Tab. 7.2. The efficiency of prompt energy cut and sum energy cut is estimated by MC simulation. In total, the efficiency of detection efficiency for ^{212}Bi-Po is 29.9%.

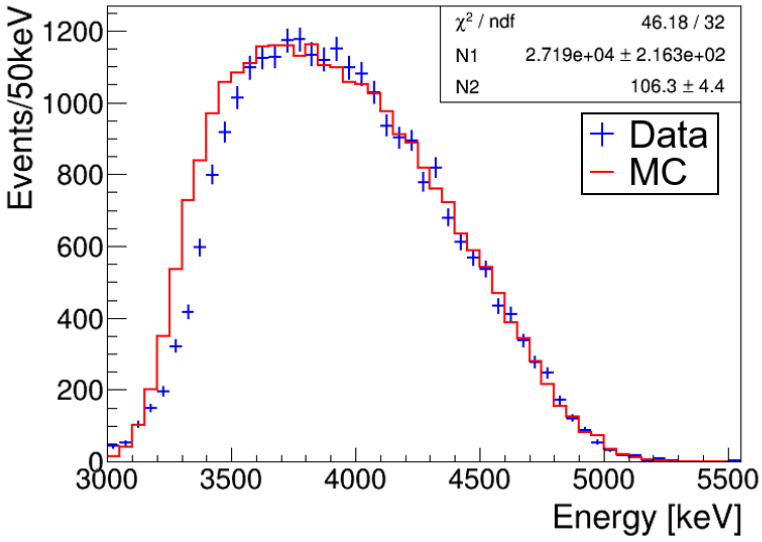

Figure 7.6: The comparison of energy distribution of data and MC simulation. Blue points correspond to physics data and red line corresponds to MC simulation.

Table 7.2: The detection efficiency of each parameter for ^{212}Bi-Po

Parameter	Efficiency [%]
Prompt energy cut (E > 400 keV)	80.0
Delayed energy cut	∼ 100
ΔT (20 < dT < 3800)	96.5
Sum energy cut (4.0 < E < 5.5 MeV)	39.4

The expected number of background events is calculated using the contamination of ^{232}Th of 5490 μBq and the detection efficiency in Tab. 7.2. The total number of ^{212}Bi-Po events is estimated to be 39374 events. The number of events above 4 MeV is 11762 events when this value is multiplied by the detection efficiency of 29.9%. The ratio of data and MC of the number of events is 1.05. Consequently, the uncertainty of MC simulation is about 5%.

The number of expected backgrounds of ^{212}Bi-Po can be calculated by the method described above. However, the events whose time difference exists less than 20 ns, are removed by other PSD method. Therefore, the rejection efficiency of ^{212}Bi-Po by other PSD method will be discussed. Details will be explained later.

^{208}Tl decay

The uncertainty of MC simulation for ^{208}Tl is evaluated by same method as described ^{212}Bi-Po sequential decay that is the comparison of the energy distribution and the number of events between physics data and MC simulation. ^{208}Tl events are selected by delayed coincidence analysis. Since the half-life of ^{208}Tl is 183.2 sec as Eq. 7.2, a lot of accidental backgrounds of delayed coincidence exists. Therefore, it is difficult to observe ^{208}Tl events using delayed coincidence method.

Fig. 7.7 shows the energy distribution of prompt and delayed events and the time difference between prompt and delayed event. ^{212}Bi-^{208}Tl events are collected during the On-time region which is from 10 to 490 sec. Off-time is set from 1520 to 2000 sec and used for evaluating the accidental background rate. Alpha events of ^{212}Bi are distributed around 1.7 MeV by the quenching effect in Fig. 7.7-(a). Around 1.7 MeV gamma events from ^{40}K and ^{208}Tl exist and they become the accidental backgrounds of ^{212}Bi alpha events. Alpha events of ^{212}Bi are selected by PSD method to remove the accidental gamma events. After that, other alpha events from ^{238}U, ^{232}Th and ^{235}U that have energies close to that of ^{212}Bi become problems. The largest peak from 1.0 to 1.5 MeV in the energy distribution is composed by alpha events and β + LS event of ^{40}K.

Fig. 7.7-(b) shows the distribution of delayed ^{208}Tl events. It is determined that the accidental backgrounds are contaminated from 3 MeV in the energy distribution of ^{208}Tl. I guess that the origin of these events is gamma ray of ^{208}Tl with the energy of 2.6 MeV from outside of the CANDLES Ⅱ I detector. These gamma events are observed as beta waveform. Therefore, these cannot be removed by PSD method. I select the energy distribution from 3.5 to 5.1 MeV to reduce the accidental background as gamma ray of

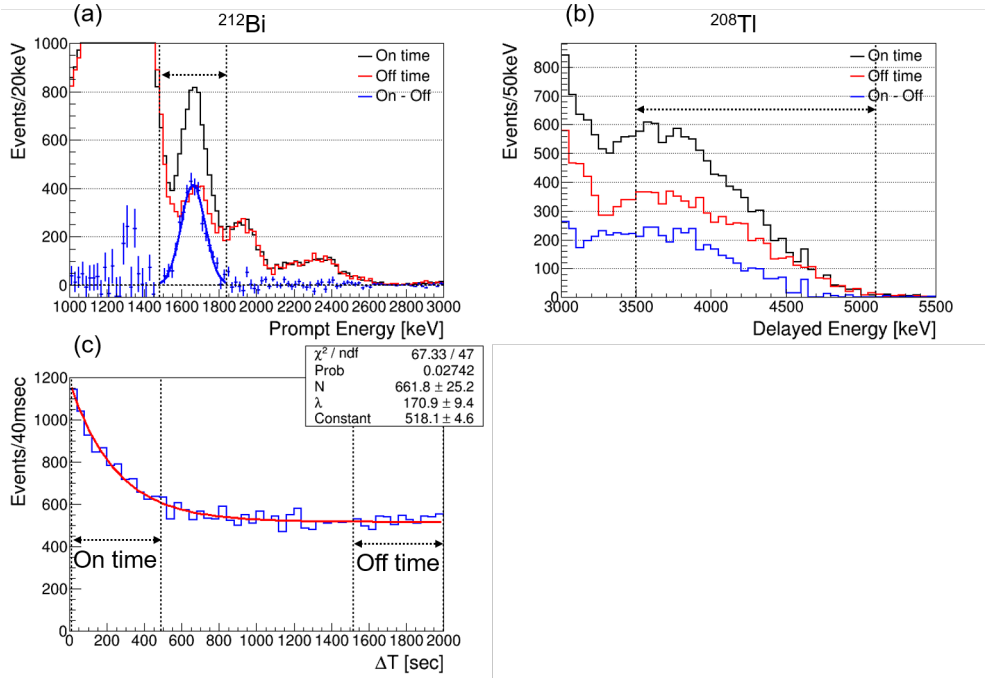

Figure 7.7: The distribution of Energy and ΔT of ^{212}Bi-^{208}Tl sequential decay. The half-life is obtained 170.9 ± 9.4 sec. This value is consistent with the literature value such as 183.2 sec.

^{208}Tl.

The time difference of ^{212}Bi-^{208}Tl is fitted by exponential function and the half-life is obtained to be 170.9 ± 9.4 sec (Fig. 7.7-(c)) This value is consistent with the literature value of 183.2 sec. Thereby, ^{208}Tl events can be selected by delayed coincidence analysis method.

Fig. 7.8 shows the comparison of the energy distribution of physics data and MC simulation. The energy distribution of physics is ^{208}Tl events of on-time minus off-time in Fig. 7.7-(b). The energy distribution of physics data above 3.5 MeV is consistent with MC simulation. The number of observed events from 3.5 to 5.1 MeV is compared with the number of expected ^{208}Tl events calculated from impurity. For evaluating the remaining number of ^{208}Tl events, detection efficiency of energy cut both for prompt and delayed events are calculated. Additionally, the detection efficiency of PSD for selecting the alpha events is also calculated. The detection efficiency for evaluating the remaining number of ^{208}Tl events is summarized in Tab. 7.3 The detection efficiency of PSD is obtained 95.0% by analyzing the alpha event example of ^{220}Rn in ^{232}Th chain which can be purely collected by delayed

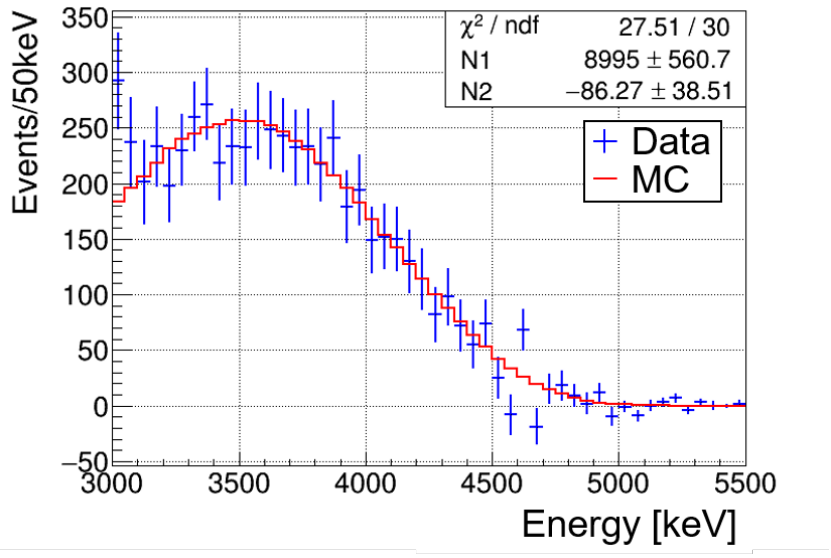

Figure 7.8: The comparison of the energy distribution of physics data and MC simulation

coincidence method as explained in Sec. 6.2. As a reason for using alpha event of ^{220}Rn, the accidental event rate of ^{220}Rn is lower than ^{212}Bi. Details will be explained in next section. The energy cut condition is $\pm 3\ \sigma$ from the peak of ^{212}Bi. Therefore, the detection efficiency of energy cut for prompt events is about 99.7%. The efficiency of ^{212}Bi-^{208}Tl coincidence in on-time is 80.7% which is calculated from the half-life of 183.2 sec. The detection efficiency of energy cut condition for ^{208}Tl from 3.5 to 5.1 MeV is calculated 17.7% by MC simulation. At this time, the cut condition is applied same cut condition which is the crystal of generated ^{208}Tl and reconstructed event position. In total, the detect efficiency for evaluating the remaining number of ^{208}Tl events is 13.4%.

Table 7.3: The detection efficiency of each parameter for ^{212}Bi-^{208}Tl

Parameter	Efficiency [%]
Prompt energy cut	99.7
PSD for selection ^{212}Bi	95.0
ΔT (10 < dT < 490)	80.7
Delayed energy cut	17.7

The number of calculated events is 2958 event and the ratio between the number of calculated events and observed events is 1.11. Therefore, the uncertainty of MC simulation is estimated to be about 11%. As one of the reason of inconsistency, the energy calibration of LS is not enough under 200 keV (Fig. 4.10). This affects the reconstruction of event position in MC simulation.

7.3 Background estimation and Detection Efficiency for $0\nu\beta\beta$

In this section, the method of reduction for each background is described in details. The detection efficiency for $0\nu\beta\beta$ decay is discussed. The cut condition of reconstructed position which is $\pm$ 2 σ from the mean of CaF_2 crystal is used for analysis in this section.

7.3.1 Energy cut condition

As described in Sec. 7.1.4, $2\nu\beta\beta$ decay are distributed continuously up to the Q value and are background for $0\nu\beta\beta$ decay. In the lower region than Q value, the selection of energy is determined 1 σ and in higher region, the selection of energy is determined 2 σ. The region of $0\nu\beta\beta$ decay is narrow around the energy region lower than Q value to reduce backgrounds like $2\nu\beta\beta$ decay. Therefore, the selection region for $0\nu\beta\beta$ analysis is determined as follows.

$$4170 < \text{Energy} < 4480 \text{ [keV]}$$

$0\nu\beta\beta$ events are simulated into CaF_2 crystals by MC simulation and the detection efficiency by energy cut is evaluated. Fig. 7.9 shows the energy distribution by MC simulation. It can be seen that some events are continuously distributed from the peak to low energy region. There are two reasons. At first, electron deposits energy in surrounding material for example acrylic box for CaF_2 crystal. The second is due to bremsstrahlung. X-ray due to bremsstrahlung deposit energy with the exception of CaF_2 crystal. From above, the detection efficiency of energy cut is 64.5%.

7.3.2 LS Events Rejection

PSD_β cut condition is optimized for $0\nu\beta\beta$ decay and its detection efficiency is estimated. The PSD_β parameter is used to select β events like $0\nu\beta\beta$ decay

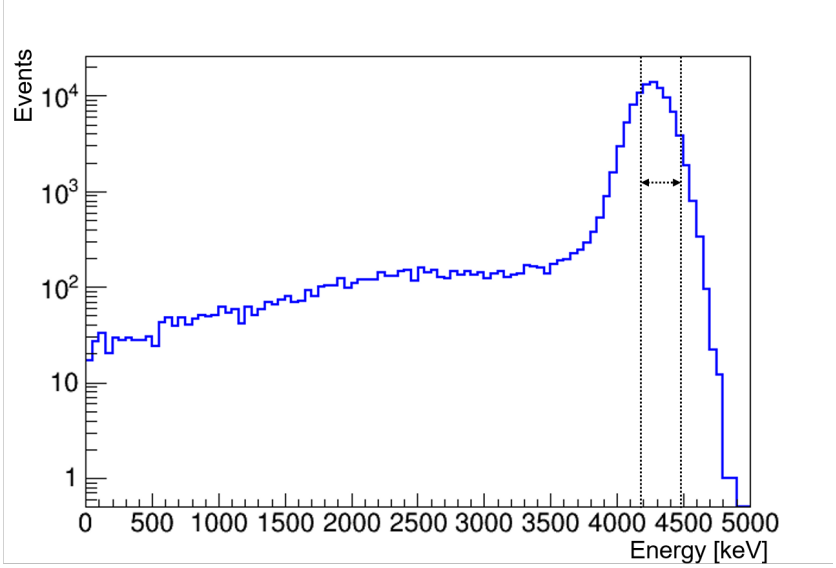

Figure 7.9: The energy distribution of $0\nu\beta\beta$ decay by MC simulation. The region indicated by the arrow is analysis region.

and remove β+LS events. This parameter can remove gamma ray of (n, γ) reactions and the event that the gamma ray emitted from ^{208}Tl within CaF_2 crystal deposit energy at the LS.

The ^{208}Tl events tagged by delayed coincidence analysis as Fig. 7.7 is used to optimize the PSD_β parameters. The figure of merit (FOM) is defined as follows:

$$\mathrm{FOM} = \frac{\mathrm{Signal}}{\sqrt{\mathrm{Signal} + \mathrm{Noise}}} \tag{7.3}$$

, where Signal is defined the number of ^{208}Tl events in On-time minus Off-time and Noise is the number of ^{208}Tl events in Off-time in Fig. 7.7. When the FOM is maximum, the cut condition of PSD_β is optimum. Fig. 7.10 shows the FOM of each cut condition of PSD_β. It is understood from the Fig. 7.10 that the optimal condition of PSD_β is less than 1.5

.

The detection efficiency of PSD_β for $0\nu\beta\beta$ decay is studied by external gamma ray of ^{208}Tl with physics data and only CaF_2 data (Sec. 5.1). Moreover, it is confirmed whether the detection efficiency with physics data is consistent with only CaF_2 data. Fig. 7.11 shows the distribution of PSD_β and plots of the detection efficiency. When the PSD_β is less than 1.5, the

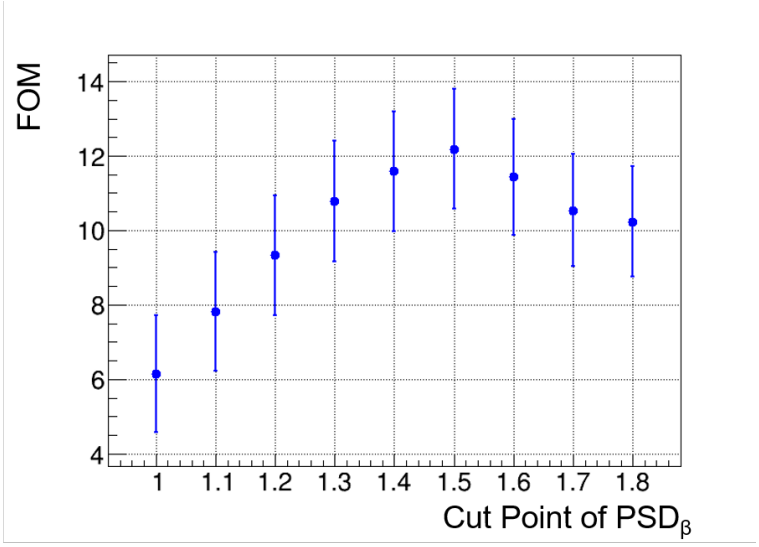

Figure 7.10: The FOM of PSD$_\beta$

detection efficiency of PSD$_\beta$ is 91.9%. This result is combined with the result of previous section, when the detection efficiency of $0\nu\beta\beta$ decay. The detection efficiency of each parameters for $0\nu\beta\beta$ decay will be summarized in next chapter.

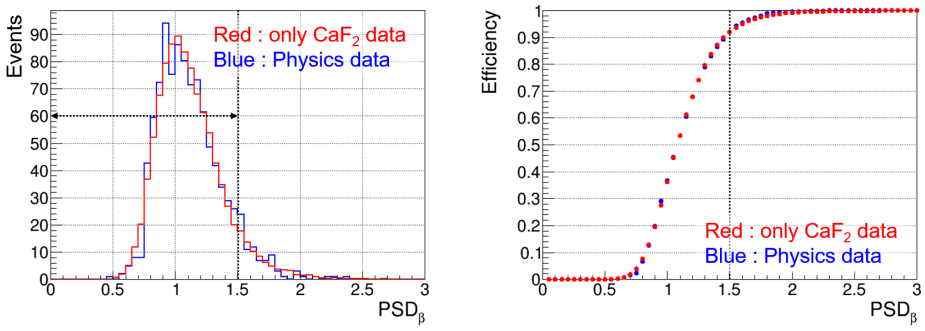

Figure 7.11: The detection efficiency of PSD$_\beta$ for $0\nu\beta\beta$

7.3.3 Double Pulse Discrimination

In the case of the time difference above 20 ns of ^{212}Bi-Po sequential decay, this events are removed by double pulse shape discrimination. The events

of time difference above 20 ns can be removed about 100% by double pulse shape discrimination, since the number of events with physics data is consistent with MC simulation as described in Sec. 7.2. On the other hand, the events whose time difference is shorter than 20 ns are difficult to be removed by double pulse cut and need to be removed by PSD_β cut. The rejection efficiency of ^{212}Bi-Po events by PSD_β has to be calculated and the number of events at Q value is evaluated.

The rejection efficiency by applying PSD_β under 1.5 is evaluated by the fake double pulse event. The fake double pulse is made artificially as follows. Fig. 7.12 shows the example of fake double pulse. The beta waveform from gamma ray of ^{208}Tl and the alpha waveform from ^{214}Po is selected individually. These waveforms are given an arbitrary time difference and are added. As a reason for using ^{208}Tl and ^{214}Po events, the gamma ray of ^{208}Tl with the energy of 2.6 MeV plus the alpha ray of ^{214}Po with the visible energy of 2.4 MeV equals total energy of about 5.0 MeV close to Q value region. Fig. 7.13 shows the rejection efficiency of double pulse events applied PSD_β under 1.5. The blue plots correspond to the fake double pulse events and the red plots correspond to the physics data. The rejection efficiency with the fake events over 10 ch (20 ns) is almost consistent with the physics data. The rejection efficiency with PSD_β under 20 ns is estimated conservatively to be 88.0%. The area ratio of alpha and beta waveform of ^{212}Bi-Po is different from that of fake double pulse and the area of alpha waveform of ^{212}Bi-Po is larger than that of the fake double pulse. I guess the rejection efficiency is better than 88.0%, since the ^{212}Bi-Po whose time difference is shorter than 20 ns is closer to alpha waveform than the fake double pulse.

The number of ^{212}Bi-Po events is estimated from the rejection efficiency and radioactive contamination of CaF_2 crystals. The survival probability of ^{212}Bi-Po events is summarized in Tab. 7.4. The survival probability of energy selection ($-1\sigma \sim +2\sigma$) is evaluated by MC simulation. In addition to this, the dead time by ^{208}Tl veto is 26.5% as described in next section. In total, the survival probability is 0.046%. The total number of ^{212}Bi-Po events is 39374 events by ^{232}Th contamination within CaF_2 crystals and the expected number of events at Q value is 18.1 ± 0.1 (stat.) $\pm$ 0.7 (syst.). The systematic error is dominated by MC simulation of 5%.

7.3.4 ^{208}Tl Beta Decay

As described in Sec. 7.1, the events of ^{208}Tl are removed by delayed coincidence method. Additionally, the events which deposit energy in LS can be removed by PSD_β. The rejection efficiency of 208Tl veto depends on the detection efficiency of ^{212}Bi alpha events and veto time. Therefore, the

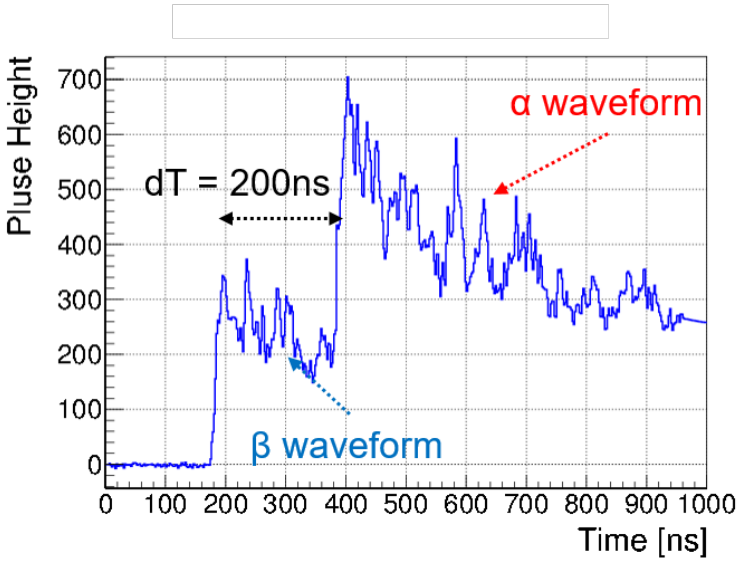

Figure 7.12: The example of fake double pulse. β waveform is made by ^{208}Tl gamma ray and α waveform is made by ^{214}Po.

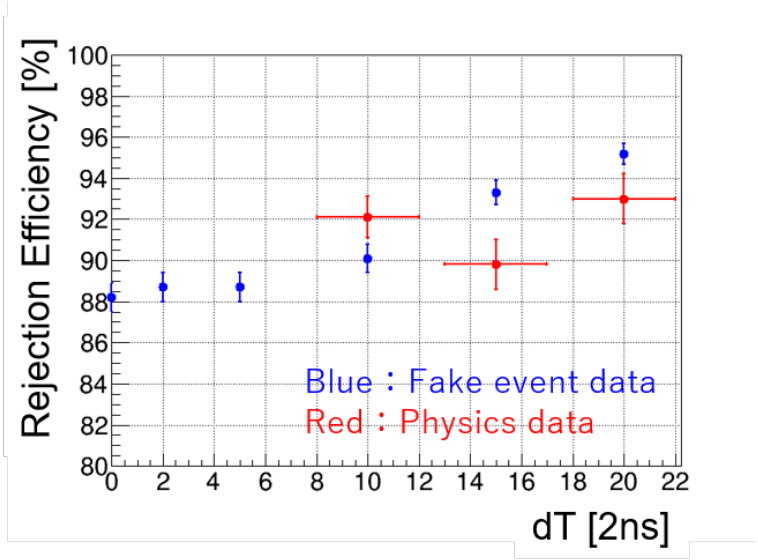

Figure 7.13: The rejection efficiency of double pulse events by PSD$_\beta$

cut condition for selecting ^{212}Bi alpha events has to be optimized and the detection efficiency of alpha event is evaluated.

Table 7.4: The survival probability of ^{212}Bi-Po with each parameters

Parameter	Survival probability	The number of events
Crystal selection ($\pm$ 2σ)	87.1	2520.6
Energy selection	13.4	3377.7
ΔT ($<$ 20 ns)	4.5	152.0
PSD$_\beta$ ($<$ 1.5)	$\sim$ 12	18.1

The parameters of PSD$_\alpha$ and PSD$_{\beta+\mathrm{LS}}$ are used to select alpha events of ^{212}Bi. As described in Sec. 5.3, discrimination by PSD between alpha and beta+LS events which deposit energy less than 200 keV in LS is difficult. In order to discriminate efficiently, these parameters are combined. The left figure in Fig. 7.14 shows two-dimensional distribution of PSD$_\alpha$ and PSD$_{\beta+\mathrm{LS}}$ using ^{220}Rn alpha events. The new PSD$_\theta$, defined as an angle in 2 dimensional space of PSD$_\alpha$ and PSD$_{\beta+\mathrm{LS}}$, is calculated for each event. The right figure of Fig. 7.14 shows 1 dimensional distribution of PSD$_\theta$ for ^{220}Rn events. The detection efficiency of alpha ray is estimated by this distribution. The reason using ^{220}Rn for estimation of the detection efficiency is the visible energy of ^{220}Rn which is about 1.8 MeV close to ^{212}Bi.

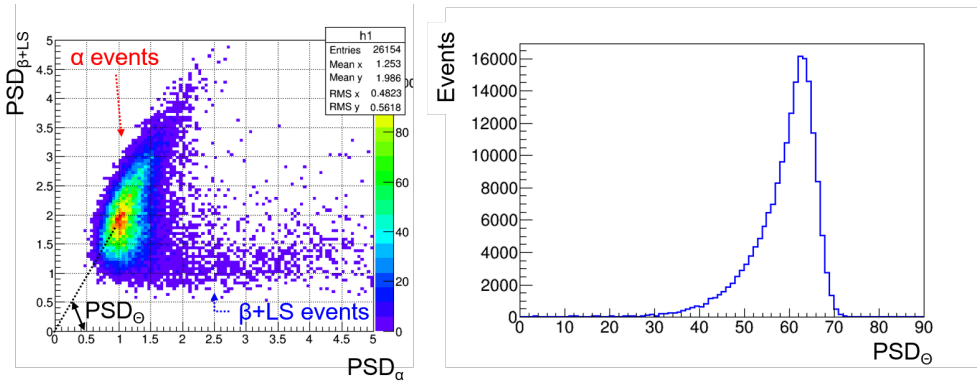

Figure 7.14: The two-dimensional distribution of PSD$_\alpha$ and PSD$_{\beta+\mathrm{LS}}$ and the distribution of PSD$_\theta$

The cut condition of PSD$_\theta$ is optimized by tagging alpha events of ^{212}Bi as Fig. 7.7 and the FOM is calculated by Eq. 7.3. Signal is defined as the number of ^{212}Bi events in On-time minus Off-time and Noise is the number of ^{212}Bi events in Off-time in Fig.7.7. Fig. 7.15 shows the FOM of each cut condition of PSD$_\theta$. The FOM of PSD$_\theta$ using 45 to 90 degree region

is maximum and the detection efficiency by applying this cut condition is 95.1%. The veto time is set to be 18 min that is 6 times longer than half-life of ^{208}Tl. The dead time by veto is 26.5%. Therefore, the detection efficiency of vetoed ^{208}Tl for $0\nu\beta\beta$ decay is 73.5%. The detection efficiency of each cuts for $0\nu\beta\beta$ decay will be summarized in the next chapter.

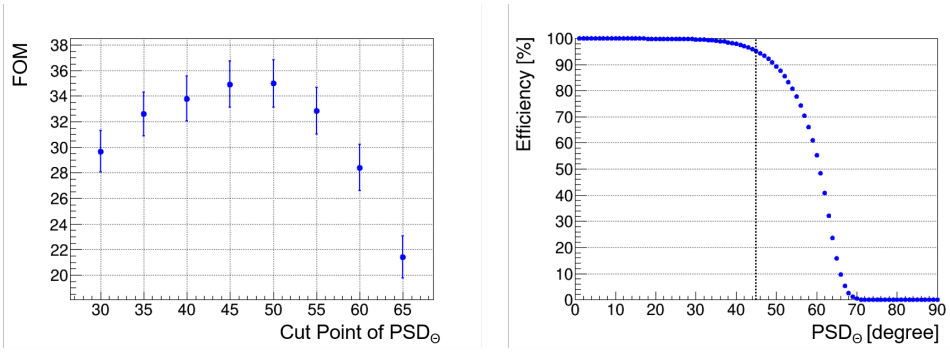

Figure 7.15: The FOM and the detection efficiency for α event of PSD$_\theta$

The events of ^{208}Tl which deposit some energy in LS can be also removed by PSD$_\beta$. In MC simulation, these events are removed by LS deposit energy instead of PSD$_\beta$. LS deposit energy dependence of PSD$_\beta$ rejection efficiency is studied. This information is necessary for estimating the number of backgrounds using MC simulation and is evaluated by analyzing the events of ^{208}Tl from physics data after appling PSD$_\beta$ less than 1.5. We searched the cut point of LS deposit energy in MC that is consistent with PSD$_\beta < 1.5$ cut in data using ^{208}Tl events in 4-5 MeV. Fig. 7.16 shows the comparison of the number of ^{208}Tl events from data and MC simulation applied cut condition of several LS deposit energy in MC. Difference is defined as follows,

$$\text{Difference} = (\text{Data} - \text{MC})/\sqrt{\text{Data}} \tag{7.4}$$

where Data is the number of observed ^{208}Tl events from 4 to 5 MeV applied PSD$_\beta < 1.5$ and MC is the number of ^{208}Tl events applyied LS depostit energy in MC simulation. Difference has the same meaning of σ. From this figure, LS cuts from 160 keV to 210 keV are consistent with PSD$_\beta < 1.5$ cut within 2 σ. The relation between PSD$_\beta$ and LS deposit energy is studied by several kinds of gamma ray, e.g. ^{88}Y, ^{208}Tl and Fe(n, γ) from data. Fig. 7.17 shows 2 dimension histgram of PSD$_\beta$ and LS deposit energy. Upper edge of LS energy at PSD$_\beta$ 1.5 is extracted from this figures by eye scan. The relation between gamma ray energy and LS deposit energy applied PSD$_\beta$

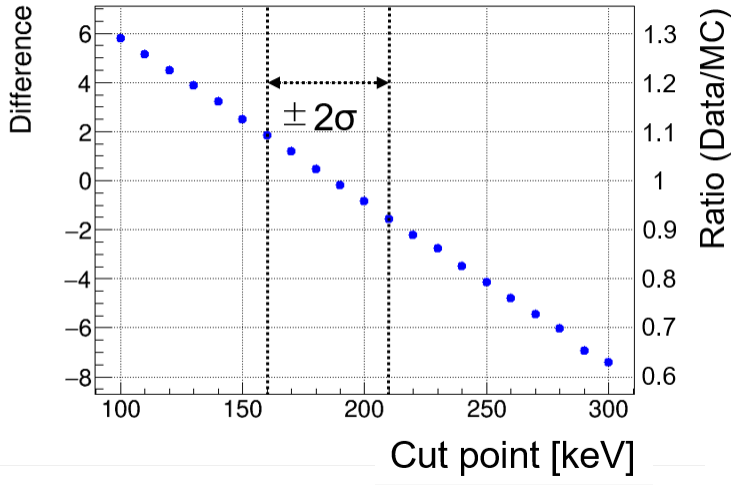

Figure 7.16: Comparison of the number of ^{208}Tl events from data and MC simulation applied cut condition of several LS deposit energy in MC.

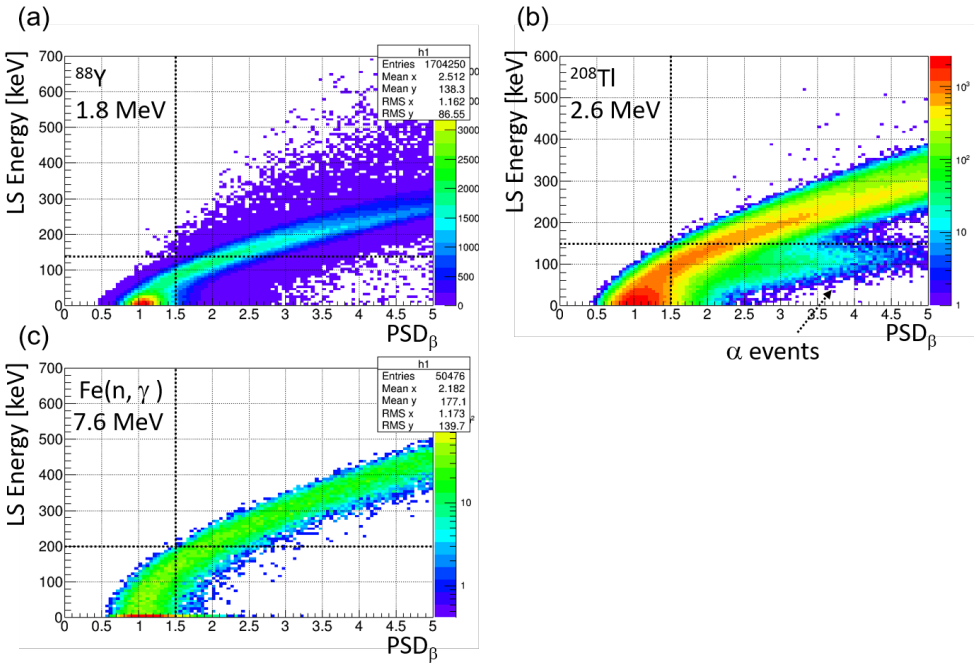

Figure 7.17: The relation between PSD$_\beta$ and LS deposit energy.

less than 1.5 is summarized in Tab. 7.5 and is shown in Fig. 7.18. Fitting function for Fig. 7.18 is as follows.

$$\text{LS Energy} = \text{p0} \times \sqrt{\text{Total Energy}} + \text{p1} \tag{7.5}$$

LS energy after appling PSD_β less than 1.5 is about 170 keV at Q value in Fig. 7.18 and this result is consistents with Fig. 7.16. LS energy cut condition for MC simulation is determined from 160 to 210 keV. The number of expected ^{208}Tl events at Q value is estimated using this result.

Table 7.5: The relation between PSD_β and LS deposit energy

	γ ray energy	LS Energy at $PSD_\beta < 1.5$
^{88}Y	1.8 MeV	140 keV
^{208}Tl	2.6 MeV	150 keV
Fe(n, γ)	7.6 MeV	200 keV

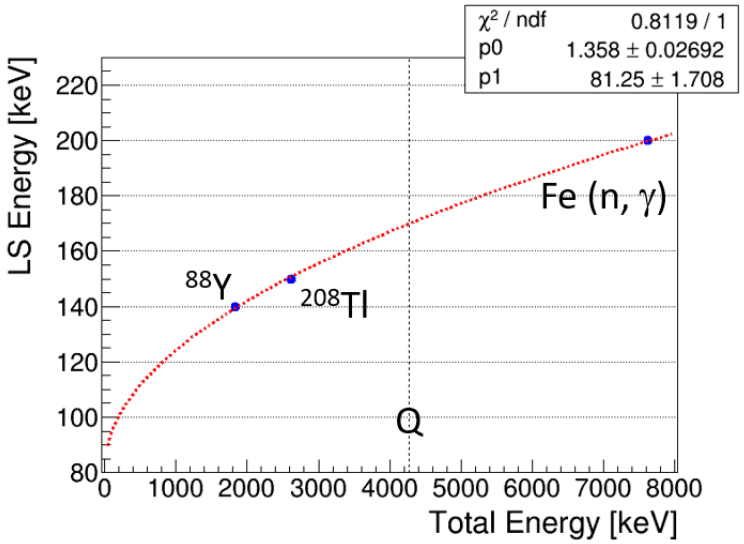

Figure 7.18: The dependence of LS energy applied $PSD_\beta < 1.5$.

The number of ^{208}Tl events is estimated from the rejection efficiency for each parameters. The survival probability of ^{208}Tl events is summarized in Tab. 7.6. The expected number of events at Q value is from 9.2 to 11.9 events . The systematic error is estimated by MC simulation which is estimated to be about 10%.

Table 7.6: The survival probability of each parameters for ^{208}Tl

Parameter	Sigle-Hit		Multi-Hit	
	Survival probability	The number of events	Survival probability	The number of events
Crystal selection ($\pm 2\sigma$)	57.9	12768.1	26.5	5843.8
Energy ($-1\sigma \sim +2\sigma$)	5.3	676.7	1.7	99.3
Veto (18 min)	7.6	51.4	73.5	73.0
PSD$_\beta$ (< 1.5)	13.4 - 17.4	6.9 - 8.8	3.1 - 4.2	2.3 - 3.1

Chapter 8

Neutrinoless Double Beta Decay Analysis

The information of target mass and the detection efficiency is summarized in this chapter. The cut condition for $0\nu\beta\beta$ decay discussed in the previous chapter is applied to physics data and the remaining number of events at Q value region is obtained. Half-life of ^{48}Ca and the effective Majorana neutrino mass are obtained.

8.1 Lower limit of ^{48}Ca half-life

Half-life of ^{48}Ca is analyzed using two types of crystal selection. The first is all crystals except special 3 crystals as explained in Sec. 6.2. Cr11 has the highest radioactive contamination among all CaF_2 crystals, Cr54 has the largest quenching factor among all CaF_2 crystals and Cr57 has a contamination of air. The second is 26 crystals that has low radioactive contamination under 10 μBq/kg. 0 background measurement is expected in the second selection. The number of targets is summarized in Tab. 8.1.

Table 8.1: The number of targets for ^{48}Ca

	93 crystals	26 crystals
^{48}Ca [g]	340.37	95.16
Live time [days]	129.5	

The detection efficiency of $0\nu\beta\beta$ decay is summarized in Tab. 8.2. In total, the detection efficiency of $0\nu\beta\beta$ decay is 43.3%.

Table 8.2: The detection efficiency of $0\nu\beta\beta$ decay

Contents	Efficiency [%]
Live time	~ 100
Energy window	64.5
Crystal cut	99.4
Beta event selection (PSD_β)	91.9
Dead time by ^{208}Tl veto	73.5

The cut condition for $0\nu\beta\beta$ decay discussed in the previous chapter is applied to physics data. Fig. 8.1 shows energy spectra before and after $0\nu\beta\beta$ cut. The top figure is for 93 crystals and the bottom figure is for 26 crystals. The number of events remaining after cut at Q value region is obtained. In 26 crystals, background free measurement at Q value region is achieved.

Observed and expected the number of events are summarized and Lower limit of half-life of ^{48}Ca is obtained and shown in Tab. 8.3. Half-life of ^{48}Ca more than 1.08×10^{23} with 26 crystals is better than that in 93 crystals. The result of the ELEGANT VI experiment is 5.8×10^{22}yr as explained in Sec. 1.3.3. Half-life using 26 crystals is longer than half-life of the ELEGANT VI experiment.

Table 8.3: ^{48}Ca $0\nu\beta\beta$ limits of half-life

	93 crystals	26 crystals
$T^{0\nu}_{1/2}$ [yr]	$> 0.36 - 0.44 \times 10^{23}$	$> 1.22 - 1.37 \times 10^{23}$
Observed background [Counts]	31	0
Sensitivity [yr]	$> 0.44 - 0.50 \times 10^{23}$	$> 0.34 - 0.35 \times 10^{23}$
Expected background [Counts]	27.3 - 30.0	2.10 - 0.92

8.2 Discussion on the Neutrino Mass

The effective Majorana neutrino mass is discussed in the previous section. Half-life is calculated by the following equation.

$$\left(T^{0\nu}_{1/2}\right)^{-1} = G_{0\nu}|M^{0\nu}|^2 \langle m_{\beta\beta}\rangle^2 \tag{8.1}$$

The PSF is calculated as following equation [39].

$$G_{0\nu} = G_{0\nu}^{(0)} \frac{{g_A}^4}{{m_e}^2} \tag{8.2}$$

where ${g_A}^4 \simeq 1.27$ and $G_{0\nu}^{(0)} = 24.81 \times 10^{-15}$ are used. It is calculated to be 2.470×10^{-25} [yr^{-1}eV^{-2}].

Double beta half-life limit can be converted into the limit of Majorana neutrino mass. The effective Majorana neutrino mass is limited by obtained limit of $0\nu\beta\beta$ half-life using 26 crystals applying the NME in Tab. 1.2.

$$\langle m_{\beta\beta} \rangle < (2.08 - 11.34)\,\mathrm{eV}\,(90\%\ \mathrm{C.L.}) \tag{8.3}$$

In the case of 93 crystals, it is limited as,

$$\langle m_{\beta\beta} \rangle < (3.77 - 20.51)\,\mathrm{eV}\,(90\%\ \mathrm{C.L.}) \tag{8.4}$$

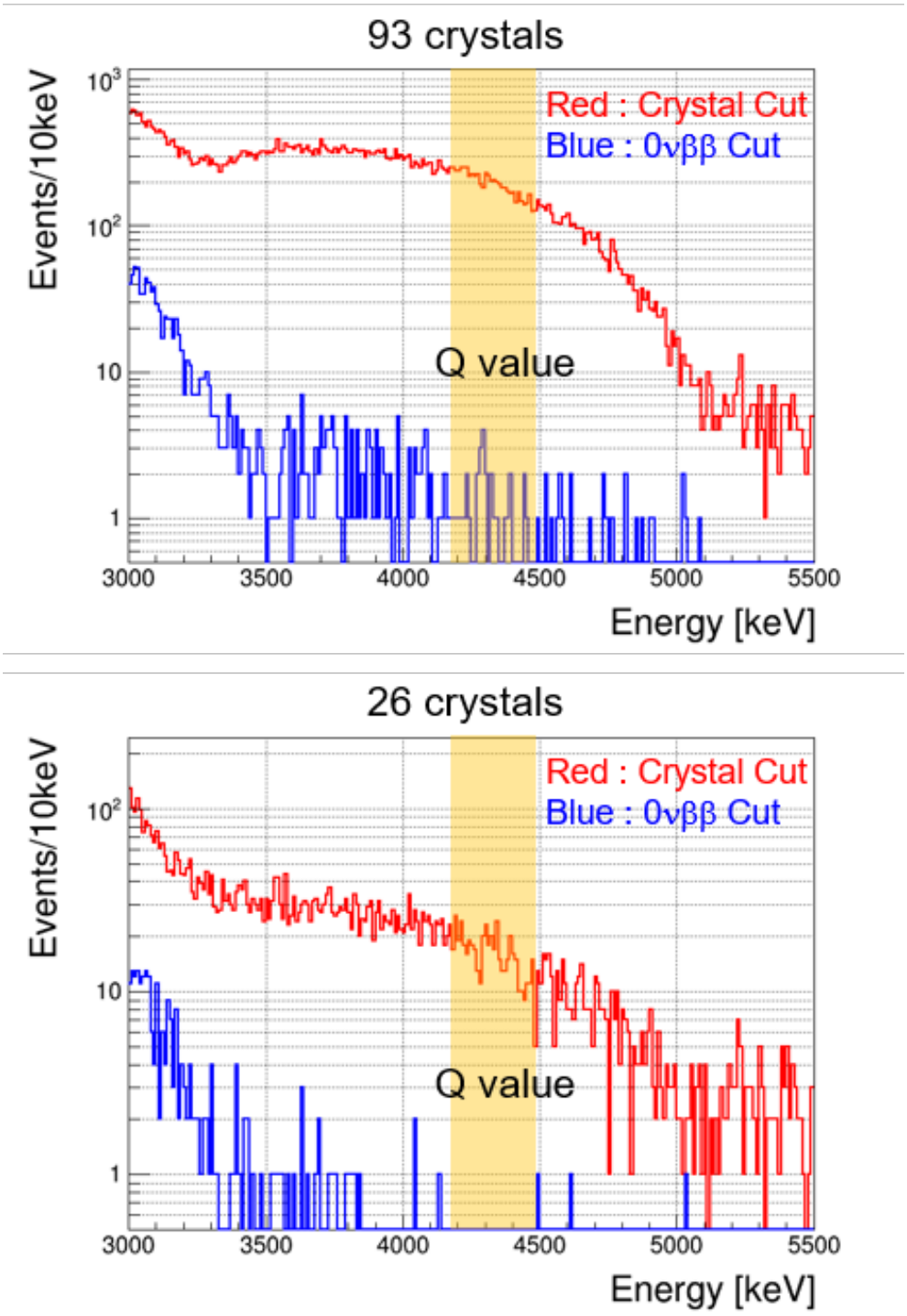

Figure 8.1: Energy spectra applied the cut condition for reduced background. Red line corresponds to crystal selection cut and blue line corresponds to $0\nu\beta\beta$ selection.

Chapter 9

Conclusion and Future Prospect

Observation of $0\nu\beta\beta$ decay demonstrates existence of a process beyond the Standard Model. This decay requires lepton number violation and demonstrates Majorana nature of neutrino. $0\nu\beta\beta$ decay rate gives Majorana effective neutrino mass scale. The CANDLES experiment is performed to search for $0\nu\beta\beta$ decay of ^{48}Ca, which is the highest Q value of 4.3 MeV among all $0\nu\beta\beta$ candidate nuclei. taking advantage of this, we aim to achieve background free measurement.

The CANDLES Ⅲ detector is operated at Kamioka Observatory. The number of expected backgrounds at Q value region is estimated using the physics data taken from June 2016 to December 2016, which is live time of 129.5 days. The radioactive contamination of ^{232}Th contained in CaF_2 crystal is dominant background. Among many radioactivity in ^{232}Th chain gives the most serious background which are ^{212}Bi-Po sequential decay and ^{208}Tl beta decay. After reduction by analysis, the number of backgrounds existing in Q value region is estimated by MC simulation and impurities value of CaF_2 crystals as follows,

$$^{212}\text{Bi-Po} : 18.1 \pm 0.1 \text{ (stat.)} \pm 0.7 \text{ (syst.) events}$$
$$^{208}\text{Tl} : 9.2 \text{ - } 11.9 \pm 0.1 \text{ (stat.)} \pm 1.2 \text{ (syst.) events}$$

where the number of used crystals is 93.

A new limit on the half-life of $0\nu\beta\beta$ decay is obtained using 93 crystals.

$$T^{0\nu}_{1/2} > 0.33 \times 10^{23} \text{ yr (90\% C.L.)}$$

In using 26 crystals that are low radioactivity, we achieve background free measurement and obtain lower limit on the half-life of $0\nu\beta\beta$ decay.

$$T^{0\nu}_{1/2} > 1.08 \times 10^{23} \text{ yr (90\% C.L.)}$$

Enrichment technique is necessary to study for the Majorana effective neutrino of normal hierarchy in Fig. 1.1. We are developing some kinds of enrichment technique [41], [42], [43]. If ^{48}Ca is able to be enriched about 20%, sensitivity becomes better by two order of magnitude. Background rate is assumed to be same as the current CANDLES III detector and live time is 1 year.

$$T^{0\nu}_{1/2} > 7.3 \times 10^{24} \text{ yr (90\% C.L.)}$$

The technique will be developed to reduce the radioactive contamination within CaF_2 crystals and the analysis will be modified to reduce the number of background events. If background free measurement will be achieved with about 20% enriched crystals, sensitivity of the half-life for $0\nu\beta\beta$ decay estimated to be:

$$T^{0\nu}_{1/2} > 4.4 \times 10^{25} \text{ yr (90\% C.L.)}$$

The CANDLES detector will be able to approach the inverted hierarchy structure.

Appendix A

Decay in Nature

A.1 ^{238}U series decay chain

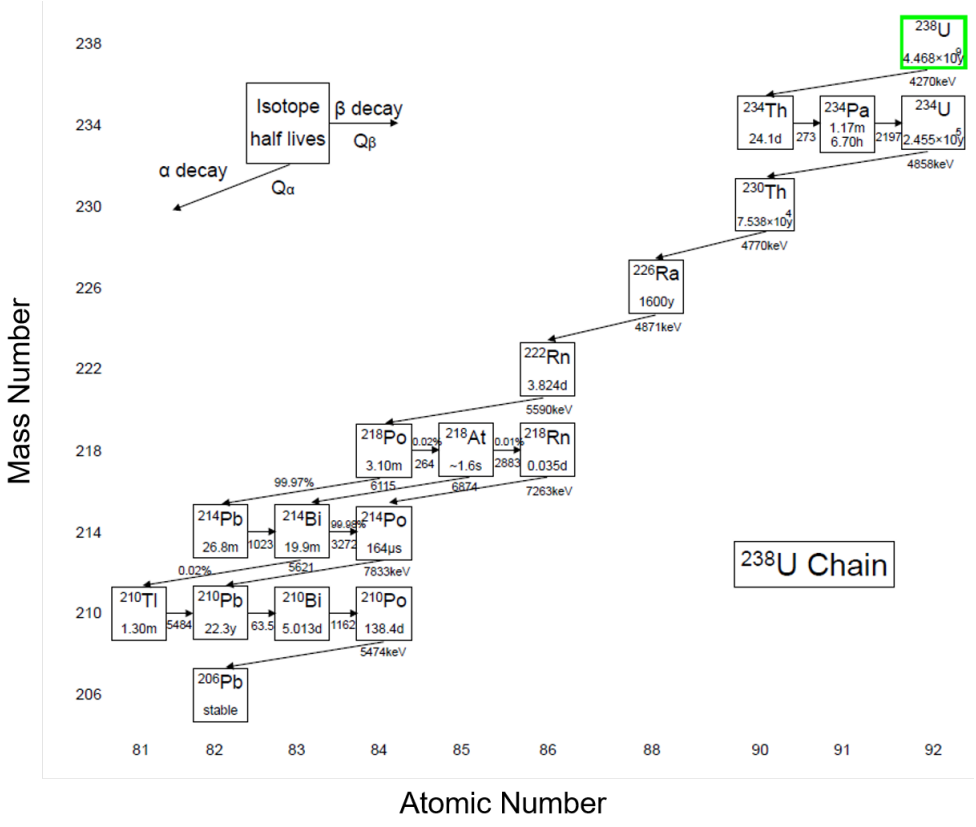

Figure A.1: ^{238}U series decay chain

A.2 ^{232}Th series decay chain

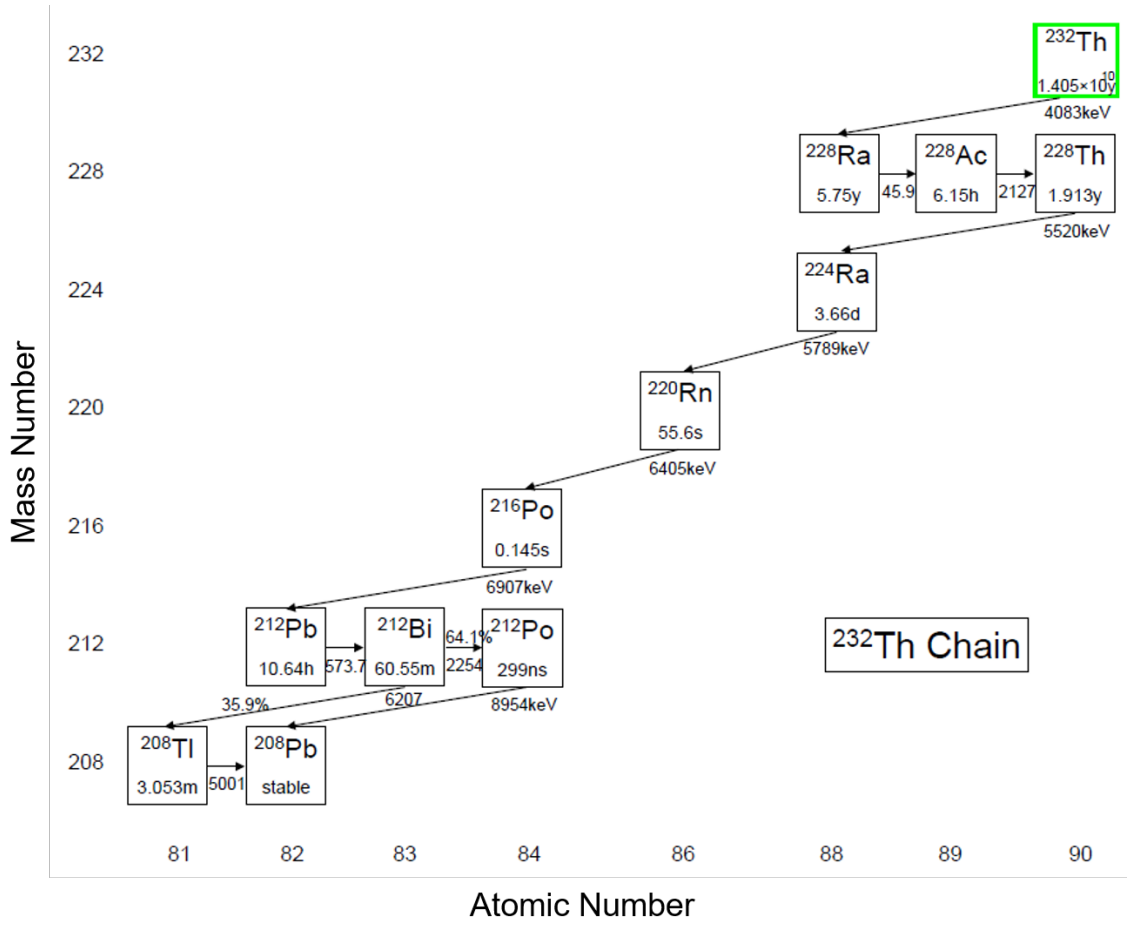

Figure A.2: ^{232}Th series decay chain

A.3 ^{235}U series decay chain

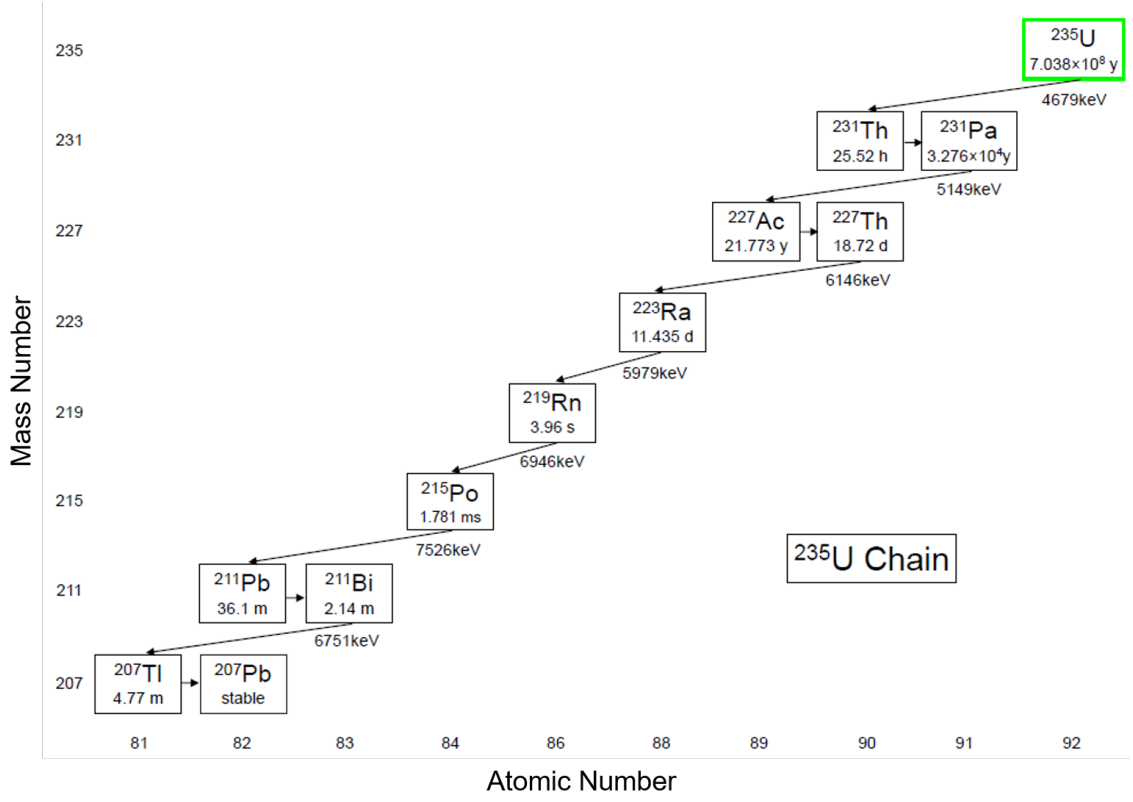

Figure A.3: ^{235}U series decay chain

A.4 ^{212}Bi-Po

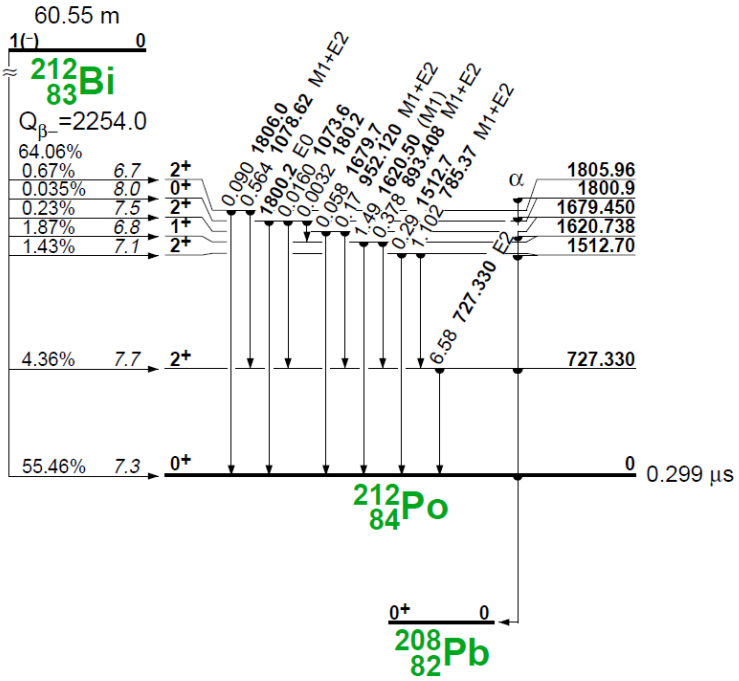

Figure A.4: Level diagram of ^{212}Bi-Po

A.5 ^{40}K

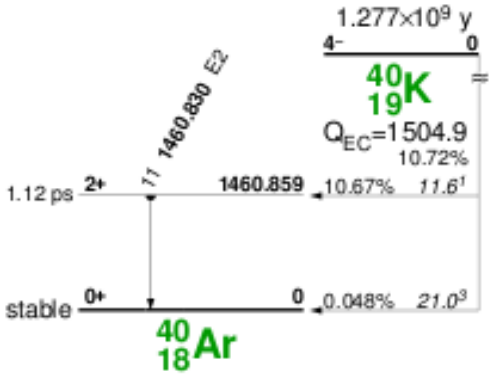

Figure A.5: Level diagram of ^{40}K

A.6 ^{214}Bi

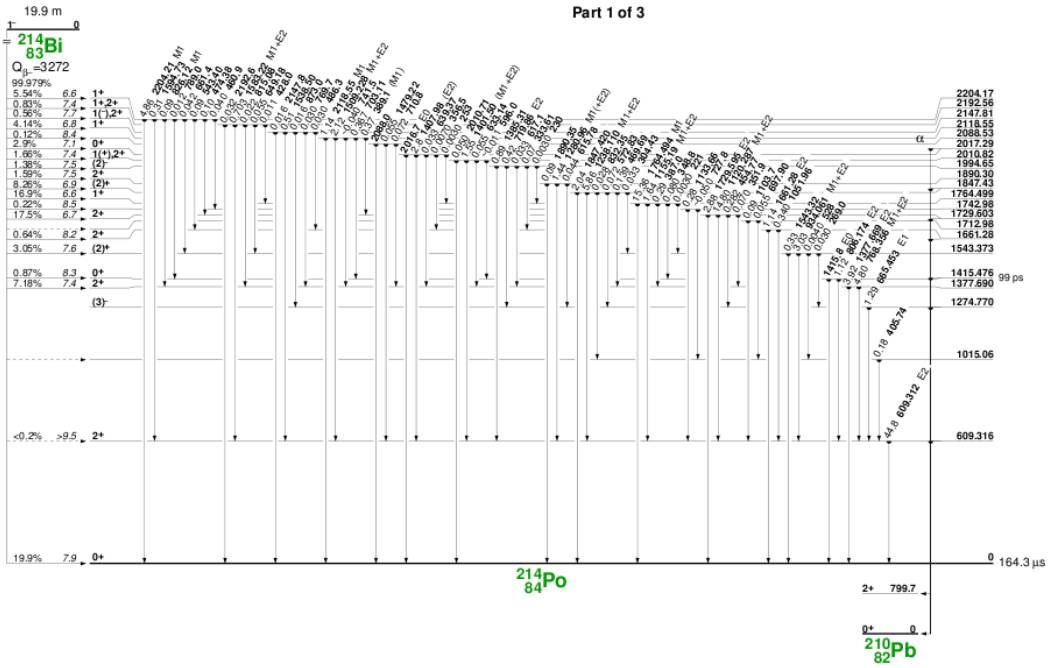

Figure A.6: Level diagram of ^{214}Bi (1)

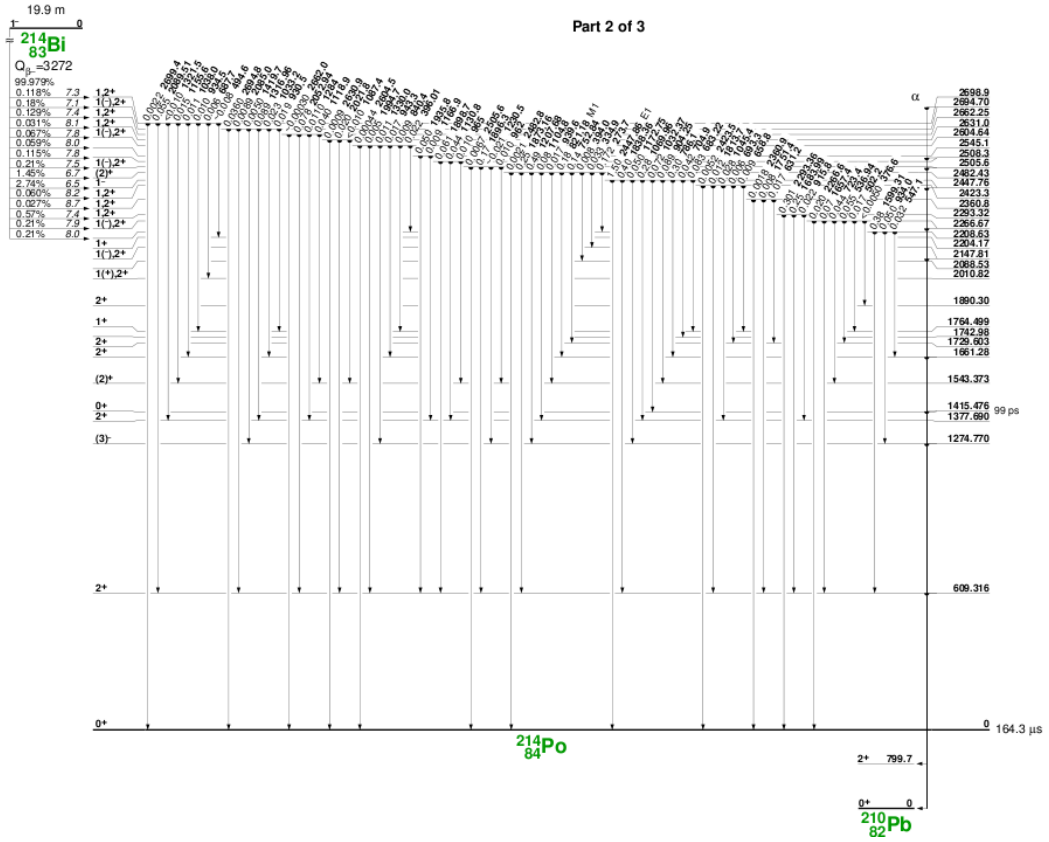

Figure A.7: Level diagram of ^{214}Bi (2)

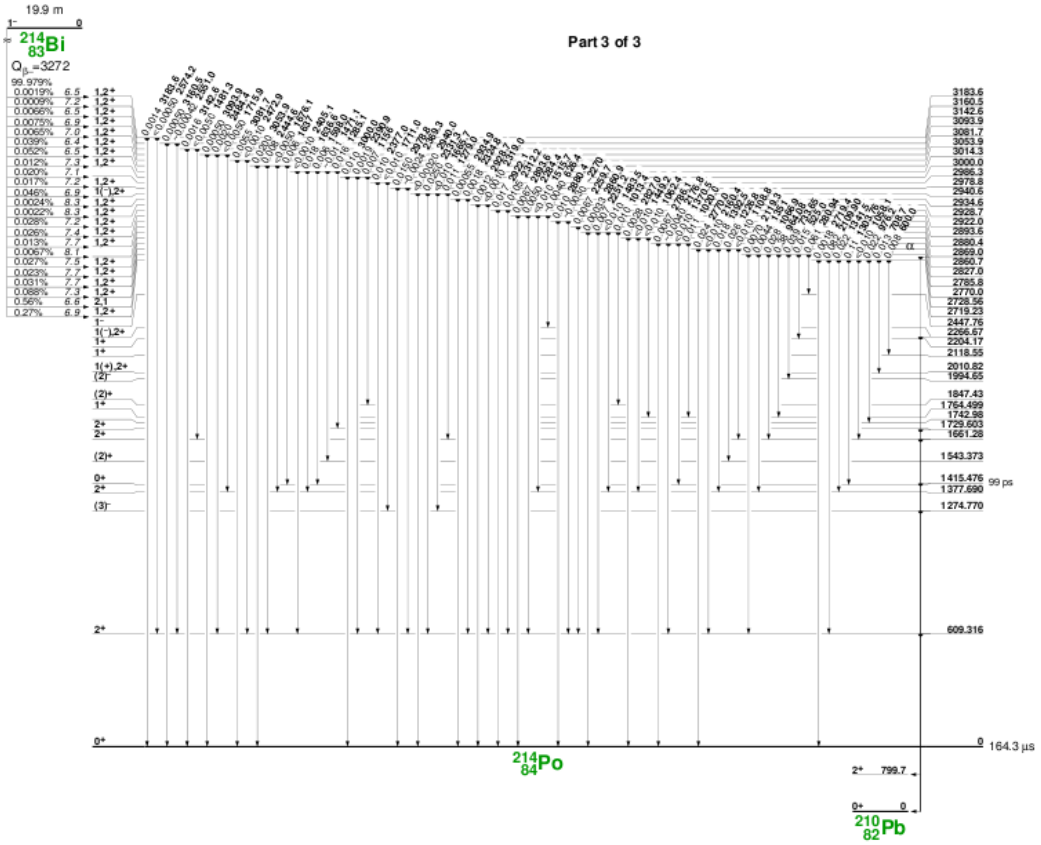

Figure A.8: Level diagram of ^{214}Bi (3)

Appendix B

Radioactive contamination of CaF_2 crystals

B.1 ^{238}U

The radioactive contamination of ^{238}U within crystals is estimated using delayed coincidence analysis of ^{214}Pi-^{214}Po (Eq. B.1).

$$^{214}\mathrm{Bi} \xrightarrow[\mathrm{Q}_\beta=3.272\mathrm{MeV}]{\mathrm{T}_{1/2}=19.9\mathrm{min}} {}^{214}\mathrm{Po} \xrightarrow[\mathrm{Q}_\alpha=7.833\mathrm{MeV}]{\mathrm{T}_{1/2}=164\mu\mathrm{sec}} {}^{210}\mathrm{Pb} \tag{B.1}$$

Fig. B.1 shows the distribution of energy and dT of ^{214}Bi-^{214}Po. on-time is time gate for selected signal events of ^{214}Bi-^{214}Po and is from 10 to 500 μsec. off-time is time gate for accidental background of ^{214}Bi-^{214}Po and is from 1010 to 1500 μsec. The detection efficiency of ^{214}Bi in on-time is calculated to be 83.8%. In energy distribution of ^{214}Bi, the peak around 2.0 MeV region is alpha events of ^{219}Rn. Visible energy of ^{214}Po and ^{215}Po is close and half-life of ^{215}Po is longer than ^{214}Po. Therefore, selection region which is the dotted arrow in Fig. B.1 is used for analysis. The detection efficiency of selection region of ^{214}Bi is estimated by MC simulation. Fig. B.2 shows the comparison of the energy distribution of physics data and MC simulation for ^{214}Bi. The detection efficiency of selection region is estimated 22.8%. Fig. B.3 shows the radioactivity contamination of ^{238}U for each crystal. The average radioactive contamination is 14.5 μBq/kg.

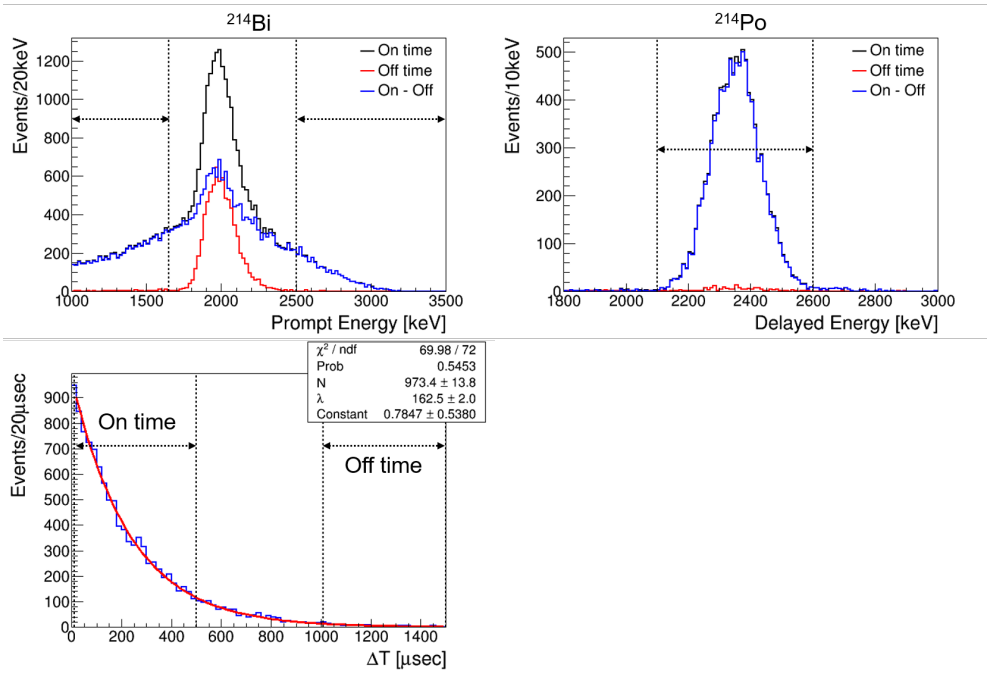

Figure B.1: Distributions of Energy and ΔT of ^{214}Bi-^{214}Po decay. The dotted arrow is the selection region.

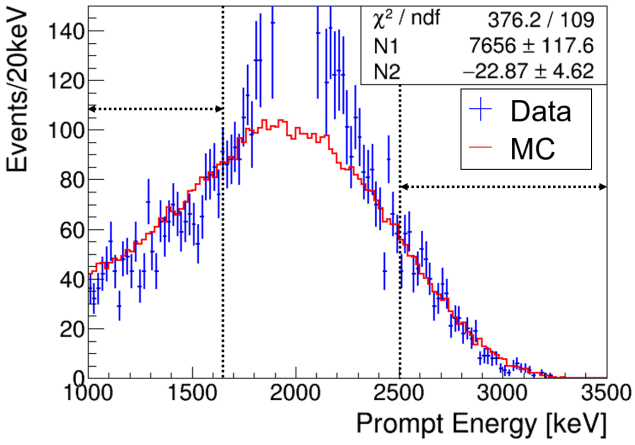

Figure B.2: The comparison of the energy distribution of physics data and MC simulation for ^{214}Bi

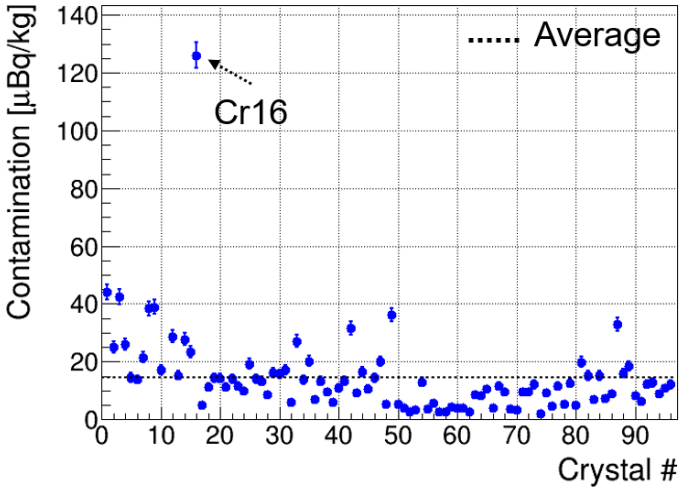

Figure B.3: The radioactive contamination of ^{238}U for each crystal

B.2 ^{235}U

The radioactive contamination of ^{235}U within crystals is estimated using delayed coincidence analysis of ^{219}Rn-^{215}Po in Fig. 5.2 (Eq. B.2).

$$^{219}\mathrm{Rn} \xrightarrow[\mathrm{Q}_\alpha=6.946\mathrm{MeV}]{\mathrm{T}_{1/2}=3.96\mathrm{sec}} {}^{215}\mathrm{Po} \xrightarrow[\mathrm{Q}_\alpha=7.526\mathrm{MeV}]{\mathrm{T}_{1/2}=1.781\mathrm{msec}} {}^{211}\mathrm{Pb} \tag{B.2}$$

Fig. B.4 shows the radioactivity contamination of ^{235}U for each crystal. The average radioactive contamination is 12.9 μBq/kg.

B.3 Low radioactive contamination of ^{232}Th

CaF_2 crystals of low radioactive contamination of ^{232}Th are summarized in Tab. B.1. Radioactive contamination of ^{232}Th under 10 μBq/kg is defined as low radioactive crystal.

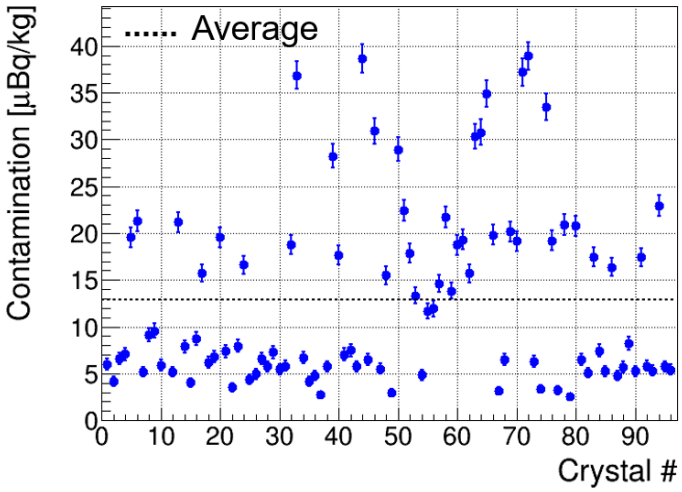

Figure B.4: The radioactive contamination of ^{235}U for each crystal

Table B.1: CaF_2 crystals of low radioactive contamination

Crystal No.	Contamination [μBq/kg]	Crystal No.	Contamination [μBq/kg]
39	9.92	61	5.12
44	9.29	62	4.49
49	6.85	63	3.31
50	3.93	64	4.49
51	4.17	65	6.85
52	5.83	69	6.22
53	2.52	70	1.89
55	1.73	71	5.35
56	2.83	72	8.34
57	1.89	74	6.14
58	4.80	75	3.93
59	2.44	76	8.50
60	5.19	80	9.05

Acknowledgment

The author ' s deepest appreciation goes to Professor T. Kishimoto for his valu- able discussions, suggestions for interpretations on observations and very kind encouragement. He has provided the author with knowledge on physics, scien- tific thinking and the others. His teachings have been very helpful for author ' s research. The author would like to express his gratitude to Professor M. Nomachi for his piercing advice and powerful discussions especially for effect of additional shieldings. The author would also like to express his gratitude to Professor S. Yoshida for his powerful leading, discussions and helpful advice for writing and presentation. The author is also deeply grateful to Dr S. Umehara for permission to refer to her great works in data analysis and helpful advice. The author is also deeply grateful to Dr K. Nakajima for permission to refer to his great works especially in Monte-Carlo simulation, kind advice and helpful discussions. The author is also deeply grateful to Dr T. Iida for his collaborations in measurement and analysis, kind advice and encouragement. The author is also deeply greatful to Dr K. suzuki for his advice about handling the experimental system and kind encouragement. The author is also deeply greatful to Dr K. Ichimura in Tokyo Univ. for his great works in analysis and helpful collaboration. The author also thanks Professor I. Ogawa in Univ. of Fukui, Professor K. Fushimi in Univ. of Tokushima and Professor R. Hazama in Osaka Sangyo Univ. for their kind advice and encouragement.

Bibliography

[1] C. L. Cowan Jr, F. Reines, F. B. Harrison, H. W. Kruse and A. D. McGuire, *Detection of the Free Neutrino: a Confirmation*, Science 20 Jul 1956, Vol. 124, Issue 3212, pp. 103-104

[2] G. Danby, J. M. Gaillard, K. Goulianos, L. M. Lederman, N. Mistry, M. Schwartz and Z. Steinbergert, *OBSERVATION OF HIGH-ENERGY NEUTRINO REACTIONS AND THE EXISTENCE OF TWO KINDS OF NEUTRINOS*, Phys. Rev. Lett. 9, 36 - Published 1 July 1962

[3] K. Kodama et al. (DONUT Collaboration), *Observation of tau neutrino interactions*, Phys. Lett. B 504 (3), 12 April 2001, Pages 218-224

[4] Raymond Davis Jr., Don S. Harmer and Kenneth C. Hoffman, *Search for Neutrinos from the Sun*, Phys. Rev. Lett. 20, 1205(1968)

[5] Y. Fukuda et al. (Super-Kamiokande Collaboration), *Evidence for Oscillation of Atmospheric Neutrinos*, Phys. Rev. Lett. 81. 1562(1998)

[6] Q. R. Ahmad et al. (SNO Collaboration), *Measurement of the Rate of* $\nu_e + d \rightarrow p + p + e^-$ *Interactions Produced by* ^8B *Solar Neutrinos at the Sudbury Neutrino Observatory*, Phys. Rev. Lett. 87, 071301(2001)

[7] S. Abe et al. (The KamLAND Collaboration), *Precision Measurement of Neutrino Oscillation Parameters with KamLAND*, Phys. Rev. Lett. 100, 221803(2008)

[8] W. C. Haxton and G. J. Stephenson Jr., *DOUBLE BETA DECAY*, Prog. Part. Nucl. Phys. 12, 409(1984)

[9] J. Mené ndez, *What do we know about neutrinoless double-beta decay nuclear matrix elements?*, arXiv:1605.05059v1

[10] J. Mené ndez, A. Poves, E. Caurier and F. Nowacki, *Disassembling the Nulear Matrix Elements of the Neutrinoless* $\beta\beta$ *Decay*, Nucl. Phys. A 818, 139(2009)

[11] Y. Iwata et al., *Large-Scale Shell-Model Analysis of the Neutrinoless $\beta\beta$ Decay of ^{48}Ca*, Phys. Rev. Lett. 116, 112502(2016)

[12] A. Neacsu and M. Horoi, *Shell model predictions for ^{124}Sn double-β decay*, Phys. Rev. C 93, 024308(2016)

[13] J. Barea, J. Kotila and F. Iachello, *$0\nu\beta\beta$ and $2\nu\beta\beta$ nuclear matrix elements in the interacting boson model with isospin restoration*, Phys. Rev. C 91, 034304(2015)

[14] F. Şimkovic, V. Rodin, A. Faessler and P. Vogel, *$0\nu\beta\beta$ and $2\nu\beta\beta$ nuclear matrix elements, quasiparticle random-phase approximation, and isospin symmetry restoration*, Rhys. Rev. C 87, 045501(2013)

[15] N. Ló pez Vaquero, T. R. Rodrí guez and J. L. Egido, *Shape and Pairing Fluctuation Effects on Neutrinoless Double Beta Decay Nuclear Matrix Elements*, Phys. Rev. Lett. 111, 142501(2013)

[16] J. Yao, L. Song, K. Hagino, P. Ring and J. Meng, *Systematic study of nuclear matrix elements in neutrinoless double-β decay with a beyond-mean-field covariant density functional theory*, Phys. Rev. C 91, 024316(2015)

[17] Klapdor-Kleingrothaus H V, Krivosheina I V, Dietz A and Chkvorets O, *Search for Neutrinoless Double Beta Decay with Enriched ^{76}Ge in Gran Sasso 1990-2003*, Phys.Lett. B 586 198 (2004)

[18] A. Gando et al., *Search for Majorana Neutrinos Near the Inverted Mass Hierarchy Region with KamLAND-Zen*, Phys. Rev. Lett. 117, 109903(2016)

[19] The GERDA Collaboration, *Background-free search for neutrinoless double-β decay of ^{76}Ge with GERDA*, Natue 544, 47-52 (06 April 2017)

[20] S. Umehara, *Study of Double Beta Decays of ^{48}Ca with CaF_2 Scintillators*, Doctral thesis, Osaka University (2004)

[21] S. Yoshida et al., *Ultra-violet wavelength shift for undoped CaF_2 scintillation detector by two phase of liquid scintillator system in CANDLES*, Nucl. Instr. and Meth. A601(2009)p282

[22] V. B. Mikhailk et al., *scintillation properties of pure CaF_2*, Nucl. Instr. and Meth. A566(2006)p522.

[23] M. Doihara, CaF_2(pure) シンチレータの冷却による発光特性の変化と波形弁別能, Master thesis, Osaka University (2014)

[24] K. Suzuki et al., *New DAQ System for the CANDLES Experiment*, IEEE Trans. Nucl. Sci., Vol. 62, Issue 3, pp. 1122-1127, Jun. 2015.

[25] M. Nomachi and S. Ajimura, *Serial data link on advanced TCA back plane*, IEEE Trans. Nucl. Sci., Vol. 53, no. 5, pp. 28492852, Oct. 2006.

[26] S. Umehara et al., *Data acquisition system of CANDLES detector for double beta decay experiment*, in Proc. IEEE Nuclear Science. Symp. Conf. Rec., 2011, pp. N464

[27] T. Maeda et al., *The CANDLES Trigger System for the Study of Double Beta Decay of* ^{48}*Ca*, IEEE Trans. Nucl. Sci., Vol. 62, Issue 3, pp. 1128-1134, Jun. 2015.

[28] S. Katagiri, CANDLES 実験における CaF_2 シンチレータと液体シンチレータの複合信号波形解析によるバックグラウンド調査, Master thesis, Osaka University (2017)

[29] M. Nomachi, Private Communication

[30] V. I. Tretyak, *Semi-empirical calculation of quenching factors for ions in scintillators*, Astripart. Phys. 33 (2010) 40-53.

[31] H.Kakubata, *Study of Background in CANDLES to Search for Double Beta Decay of* ^{48}*Ca*, Doctral thesis, Osaka University (2015)

[32] M. Moser, *Analysis of neutron induced background in CANDLES*, Master thesis, Osaka University (2017)

[33] S. Agostinelli et al., *GEANT4 - A simulation toolkit*, Nucl. Instruments Methods Phys. Res. Sect. A Accel. Spectrometers, Detect. Assoc. Equip. 506.3 (2003), pp. 250303.

[34] J. Allison et al., *Geant4 Developments and Applications*, IEEE Trans. Nucl. Sci. VOL. 53, NO. 1, Feb. 2006

[35] J. Allison et al., *Recent developments in GEANT4*, Nucl. Instruments Methods Phys. Res. A 835(2016)186225

[36] A. Balysh, A. De Silva, V. I. Lebedev, K. Lou, M. K. Moe, M. A. Nelson, A. Piepke, A. Pronskiy, M. A. Vient and P. Voge, *Double Beta Decay of* ^{48}*Ca*, Phys. Rev. Lett. 77, 5186(1996)

[37] V. B. Brudanin, N. I. Rukhadze, Ch. Briancon, V. G. Egorov, V. E. Kovalenko, A. Kovalik, A. V. Salamatin, I. Stekl, V. V. Tsoupko-Sitnikov, Ts.Vylov and P.Cermakc, *Search for double beta decay of ^{48}Ca in the TGV experiment*, Phys. Lett. B 495 (2000) 63

[38] R. Arnold et al. (NEMO-3 Collaboration), *Mesurement of the double-beta decay half-life and search for the neutrinoless double-beta decay of ^{48}Ca with NEMO-3 detector*, Phys. Rev. D 93, 112008(2016)

[39] J. Kotila and F. Iachello, *Phase-space factors for double-β decay*, Phys. Rev. C 85, 034316(2012)
http://nucleartheory.yale.edu/double-beta-decay-phase-space-factors

[40] G. Feldman and R. Cousins, *Unified approach to the classical statistical analysis of small signals*, Phys. Rev. D 57, 3873(1998)

[41] T. Kishimoto et al., *Calcium isotope enrichment by means of multi-channel counter-current electrophoresis for the study of particle and nuclear physics*, Prog. Theor. Exp. Phys. 2015, 033D03

[42] S. Umehara et al., *A basic study on the production of enriched isotope ^{48}Ca by using crown-ether resin*, Prog. Theor. Exp. Phys. 2015, 053C03

[43] A. Khumaeni et al., *Emission Characteristics of Ca and Mg Atoms in Gas Plasma Induced by the Bombardment of Transversely Excited Atmospheric CO_2 Laser at 1 atm*, Jpn. J. Appl. Phys. 51(2012) 082403

[44] Richard B. Firestone, Virginia S. Shirley et al., *The 8th edition of the Table of Isotopes*, John Wiley & Sons. Inc., 1996

[45] I. Narsky, *Optimization of Signal Significance by Bagging Decision Trees*, arXiv:physics/0507157v1

[46] Kai Zuber, *Neutrino Physics Second Edition*, CRC press.

[47] M. Fukugita and T. Yanagida, *Physics of Neutrinos: and Application to Astrophysics*, Springer; 2003

[48] T. Kishimoto et al., *CANDLES for the study of double beta decay of Ca-48*, in: Proc. of 4th workshop on Neutrino Oscillations and their Origin, 2003, p. 338.

[49] T. Iida et al., *The CANDLES experiment for the study of Ca-48 double beta decay*, Nucl. Part. Phys. Proc. 273-275 (2016) 2633-2635

[50] K. Nakajima et al., *Low Background Techniques in CANDLES*, AIP Conf. Proc. 1672, 110004 (2015)

[51] T. Iida et al., *Status and future prospect of 48Ca double beta decay search in CANDLES*, Journal of Physics: Conference Series 718 (2016) 062026

[52] T. Kishimoto, T. Ohata, K. Matsuoka, S. Umehara and K. Fukumoto, *Calcium isotope enrich by MCCCE for the study of* ^{48}*Ca* $\beta\beta$ *decay*, SPLG 2015 Conference Proceeding p63 66

[53] K. Nakajima et al., *Performance of updated shielding system in CANDLES*, AIP Conf. Proc. 1921, 060003 (2018)

[50] Y. Hirano, *CANDLES Detector for the study of Double Beta Decay of* ^{48}*Ca*, Doctral thesis, Osaka University (2008)

[51] S. Matsuda, *Search for Neutrinoless Double-Beta Decay in* ^{136}*Xe after Intensive Background Reduction with KamLAND-Zen*, Doctral thesis, Tohoku University (2016)

[52] T. Batpurev, *The study of multi-hit events for reductions of background in CANDLES*, Master thesis, Osaka University (2016)

[xx] K. Kamada et al., *Single Crystal Growth and Scintillation Properties of Ca(Cl, Br, I)*^{2} *Single Crystal*, 10.1016/j.ceramint.2017.05.249